

Implementation and Analysis of a Bayesian Approach to Topographic Reconstruction with Multiple Antenna Synthetic Aperture Radar Interferometry

Amit Ashok

A dissertation submitted to the Department of Electrical Engineering,
University of Cape Town in partial fulfilment of the requirements for the
Degree of Master of Science in Electrical Engineering.



University of Cape Town
Cape Town, 2001

Declaration

I declare that this dissertation is my own, unaided work. It is being submitted in partial fulfilment for the Degree of Master of Science in Engineering in the University of Cape Town. It has not been submitted before for any degree or examination in any other university.

Signature of Author.....

Cape Town, 16 February 2001.

Acknowledgements

I wish to express my sincere thanks to my supervisor Dr. A.J. Wilkinson for his support and guidance during the course of this dissertation.

I would also like to thank my co-supervisor Professor M. R. Inggs for his support.

I wish to thank all members of the radar remote sensing group (RRSG) at UCT for providing a enjoyable and stimulating work environment.

To my parents and brother for all their support and encouragement.

For financial support I am also grateful to University of Cape Town for “International Student Scholarship”.

Abstract

Multiple-antenna synthetic aperture radar (SAR) interferometry is a single-pass interferometry technique for topographic mapping. A Bayesian model-based approach to topographic reconstruction with multiple-antenna SAR interferometry, proposed by Dr. A. J. Wilkinson, is implemented and analysed in this dissertation. The phase ambiguity reduction and data-noise improvement achieved with multiple-antenna interferometry are explained from the basic principles of radar interferometry. The surface topography is modelled by a rectangular grid of discrete points on the ground, corresponding to the individual pixels in a SAR image. The position of each point is parameterised in terms of the angle of arrival of the received signal, represented by a pixel in the SAR image. Topographic reconstruction stated as an angle of arrival parameter estimation problem in a Bayesian inference framework.

To generate the necessary multiple-antenna data, an interferometric SAR simulator (based on a forward-model for the SAR imaging process) is implemented. Two Bayesian estimation methods are implemented for estimating the angle of arrival parameter from the simulated multiple-antenna data. One estimation method uses a single pixel data vector to estimate the angle of arrival for a point in a image. The other estimation method employs a multiple pixel data vector with data from neighbouring pixels to estimate the angle of arrival for a point in the image. The likelihood and posterior distributions of angle of arrival obtained with the Bayesian estimation methods are analysed in detail for a three-antenna airborne SAR system. The ambiguities measured in the likelihood distribution of the angle of arrival obtained using the three-antenna simulated dataset are verified from theoretical calculations. A measure of the accuracy of the angle of arrival estimate is formulated in terms of the standard deviation of posterior distribution obtained from the Bayesian analysis of the data. Finally, the Bayesian estimation methods are applied to a simulated three-antenna dataset to demonstrate the topographic reconstruction process.

Contents

Declaration	i
Acknowledgements	ii
Abstract	iii
Contents	iv
List of Figures	vi
List of Tables	ix
List of Symbols and Acronyms	x
1 Introduction	1
1.1 SAR Interferometry	2
1.2 Topographic Mapping with SAR Interferometry	3
1.3 Multiple-Antenna SAR Interferometry	4
1.4 Dissertation Objectives	4
1.5 Outline of Dissertation	5
2 Theory and Problem Formulation	7
2.1 Introduction	7
2.2 Multiple-Antenna Interferometry Theory	7
2.2.1 Principles of Radar Interferometry	8
2.2.2 Reduced Ambiguity with Multiple-Antennas	12
2.2.3 Data-Noise Improvement with Multiple Data Measurements	13
2.3 Bayesian Inference	14
2.3.1 Background	14
2.3.2 Bayes Theorem	14
2.3.3 Bayesian Parameter Estimation	15

2.4	Problem Formulation	16
2.5	Multiple-Antenna InSAR Data	17
3	Multiple-Antenna InSAR Simulator	18
3.1	Introduction	18
3.2	Principles of SAR Imaging	19
3.2.1	SAR Imaging Geometry	19
3.2.2	Ground to Slant Range Mapping	19
3.2.3	SAR Image Formation	20
3.3	Properties of SAR Images	21
3.3.1	SAR Image Statistics	21
3.3.2	Joint SAR Image Statistics: Forward Model	22
3.3.3	Complex Covariance Matrix	23
3.3.4	Coherence Model	24
3.3.4.1	Temporal coherence	24
3.3.4.2	Geometric coherence	25
3.3.4.3	Receiver noise coherence	26
3.3.5	Received Power	26
3.4	Simulator Architecture	27
3.5	Simulation Geometry	27
3.6	Simulation Program	28
3.6.1	Input Files	30
3.6.2	Simulation Processing Steps	31
3.6.2.1	Ground to slant range conversion	31
3.6.2.2	Radar cross section	31
3.6.2.3	Phase and Coherence	33
3.6.3	Data generation from joint distribution	35
3.6.4	Output Files	36
3.7	Simulator Performance	36
3.8	Simulation Example	37
4	Bayesian Topographic Reconstruction Methods	38
4.1	Introduction	38
4.2	Parameter Selection	38
4.3	Coherence Estimation	39
4.3.1	Simulation Coherence	40
4.3.2	Maximum Likelihood Coherence Estimator	40

4.4	Scene Topographic Reconstruction	40
4.5	Point Position Estimation with Single Pixel Data set	41
4.5.1	Method Description	41
4.5.2	Application	44
4.6	Point Position Estimation with Multiple Pixel Data set	47
4.6.1	Method Description	47
4.6.2	Application	50
5	Analysis of Results	53
5.1	Introduction	53
5.2	Simulated SAR Data	53
5.3	Ambiguity Analysis	55
5.4	Accuracy Analysis	58
5.5	Terrain Reconstruction	62
6	Conclusion and Future Work	66
6.1	Conclusion	66
6.2	Future Work	68
A	Simulation Example	69
B	Topographic Reconstruction Demonstration	77
	Bibliography	81

List of Figures

1.1	Across track InSAR geometry.	3
2.1	Geometry of a dual-antenna InSAR system.	9
2.2	Ambiguous direction of arrival of the echo signal from the point P.	11
2.3	Geometry of an asymmetrical three-antenna InSAR system.	12
3.1	Strip-map SAR geometry	19
3.2	Ground range to slant range mapping for side-looking geometry.	20
3.3	SAR image formation model.	21
3.4	Geometry depicting incidence angles.	25
3.5	Simulator architecture.	27
3.6	Imaging geometry of a typical simulation showing antenna flight-paths and the imaged DEM.	28
3.7	SAR image generation with forward model.	28
3.8	Flow chart of the simulation program.	29
3.9	Ground to slant range conversion.	32
3.10	Slant to ground projection geometry.	34
4.1	System geometry showing the relationship between the surface height and angle of arrival	39
4.2	Pixel data set used for estimating the location of a point.	42
4.3	Angle of arrival geometry	43
4.4	Antenna and slant range geometry.	45
4.5	System and ground point geometry.	45
4.6	Prior, Likelihood and Posterior probability distributions.	46
4.7	Multiple pixel data set ($L = 1$) for estimating the position of the point.	48
4.8	A straight line through predicted position of all points.	49
4.9	Intersection of a k^{th} slant range arc with the line.	50
4.10	Marginalised probability distributions for angle of arrival and local slope angle.	52

5.1	Simulation geometry of a inclined plane DEM with the three-antenna InSAR system.	54
5.2	Likelihood PDF of angle of arrival using various antenna pairs.	56
5.3	Likelihood PDF of angle of arrival using all three antenna pair data.	57
5.4	Posterior PDF of angle of arrival using all three antenna data.	59
5.5	Posterior PDF with one pixel data set. The vertical dotted lines mark one standard deviation from the peak	60
5.6	Posterior PDF with three pixel data set. The vertical dotted lines mark one standard deviation from the peak	61
5.7	Posterior PDF with five pixel data set. The vertical dotted lines mark one standard deviation from the peak	61
5.8	Slant range profile of estimated and real terrain height.	63
5.9	The height standard deviation of estimated height.	63
5.10	A slant range plot of the simulated and estimated (dotted line) coherence for data from antenna pair (1,3).	64
5.11	A slant range plot of the simulated and estimated (dotted line) coherence for data from antenna pair (1,2).	64
5.12	A slant range plot of the simulated and estimated (dotted line) coherence for data from antenna pair (2,3).	65
A.1	SAR magnitude image acquired from antenna 1.	71
A.2	Interferogram formed with antenna 1 and antenna 3 SAR images.	72
A.3	Interferogram (flat earth component removed) formed with antenna 1 and antenna 3 SAR images.	72
A.4	Interferogram formed with antenna 1 and antenna 2 SAR images.	73
A.5	Interferogram (flat earth component removed) formed with antenna 1 and antenna 2 SAR images.	73
A.6	Interferogram formed with antenna 2 and antenna 3 SAR images.	74
A.7	Interferogram (flat earth component removed) formed with antenna 2 and antenna 3 SAR images.	74
A.8	Coherence map for antenna 1 and antenna 3 SAR images.	75
A.9	Coherence map for antenna 1 and antenna 2 SAR images.	75
A.10	Coherence map for antenna 2 and antenna 3 SAR images.	76
B.1	Actual DEM, slant range projection.	77
B.2	Actual DEM Contour map, slant range projection.	78
B.3	Reconstructed DEM, slant range projection.	78
B.4	Reconstructed DEM Contour map, slant range projection.	79

B.5	Height standard deviation map, slant range projection.	79
B.6	Horizontal standard deviation map, slant range projection.	80
B.7	Displacement standard deviation map, slant range projection.	80

List of Tables

3.1	Simulation times for various image sizes.	37
3.2	SAR system and imaging geometry parameters.	37
3.3	Surface DEM parameters.	37
4.1	System and ground point parameters.	47
5.1	Three antenna InSAR system and scene parameters.	54
5.2	Ambiguities corresponding to the 3 vertical baselines in the three-antenna system.	55
5.3	Phase standard deviation and coherence theoretically calculated values.	58
5.4	Angle of arrival and height standard deviations for various number of datasets.	60
5.5	Mound DEM parameters.	62

List of Symbols and Acronyms

Symbols

a	Normalization constant.
A_{GR}	Ground range resolution cell area.
A_{SR}	Slant range resolution cell area.
A	Amplitude of a complex signal.
b	Baseline.
BW	Bandwidth of the transmitted pulse.
c	Speed of light.
D	Data used in estimation.
$E()$	Statistical expectation.
f_o	Radar transmission frequency.
G	Radar gain.
h	Vertical position of a point or point height.
I	Real part of a complex signal.
j	Complex number $\sqrt{-1}$.
k	Integer number of phase cycles.
\mathbf{K}	Complex covariance matrix.
l	Shortest distance between two adjacent ambiguities.
M	Number of pixels in a sampling window.
\hat{n}	Surface normal vector.
N	Number of antennas.
$N()$	Normal distribution.
p	Ambiguity enhancement factor.
$P()$	Probability distribution.
P_r	Power received.
P_{noise}	Received noise power.
Q	Imaginary part of a complex signal.

\hat{r}	Slant range vector.
R	Slant range.
SNR	Signal to Noise Ratio.
t_d	Time delay between transmitted and received pulse.
\hat{v}	Antenna velocity vector.
V	SAR image.
$W()$	Wrapping operator.
x	Azimuth.
y	Horizontal position of a point.
z	Height.
α	Surface slope angle.
β	Terrain slope factor .
γ	Complex coherence.
$\gamma_{geometry}$	Geometric coherence factor.
γ_{time}	Temporal coherence factor.
γ_{snr}	Signal to noise coherence factor.
γ_{reg}	Misregistration coherence factor.
Δf_{range}	Spectral frequency shift in range.
$\Delta \theta_{amb}$	Angle of arrival ambiguity.
Δl_{amb}	Shortest distance between two adjacent ambiguities.
Δh_{amb}	Vertical displacement between two adjacent ambiguities.
Δy_{amb}	Horizontal displacement between two adjacent ambiguities.
η	Surface reflectivity coefficient.
θ_{inc}	Incidence angle.
θ	Angle of arrival.
λ	Carrier wavelength
σ	Radar cross section.
σ°	Radar cross section coefficient.
σ_θ	Angle of arrival standard deviation.
σ_l	Displacement standard deviation.
σ_h	Height standard deviation.
σ_y	Horizontal standard deviation.
ψ	Wrapped phase.
φ	Absolute phase.

Acronyms

DEM	Digital Elevation Model.
InSAR	Interferometric Synthetic Aperture Radar.
MAP	Maximum Posterior Estimate.
MLE	Maximum Likelihood Estimate.
PDF	Probability Density Function.
RADAR	Radio Detection and Ranging.
RCS	Radar Cross Section.
SNR	Signal to Noise Ratio.
SAR	Synthetic Aperture Radar.
JPL	Jet Propulsion Laboratories.

Chapter 1

Introduction

Synthetic Aperture Radar Interferometry (InSAR) or SAR interferometry, is a radar based technique for producing high resolution topographic maps of planetary surfaces. It is a remote sensing technique that has found applications in topographic studies of remote regions, surface monitoring, and even planetary exploration. Applications such as topographic mapping and surface change detection using InSAR and related techniques have been demonstrated by Graham (1974), Zebker and Goldstein (1986), Goldstein and Zebker (1987), Gabriel and Goldstein (1988), Gabriel et al. (1989), Massonnet et al. (1995). Today SAR interferometry is greatly appreciated as an extremely power tool for mapping planetary surfaces, especially the Earth's land, ice, and sea surface topography. It can produce topographic data in the form of a *digital elevation map* (DEM) that is required in several geophysical, geological and surveying applications. However, most of the current SAR interferometry techniques for topographic mapping use repeat-pass SAR interferometry, which suffers from some inherent drawbacks such as degraded performance due to time-decorrelation and atmospheric effects (Massonnet and Rabaute 1993), (Goldstein 1995), (Tarayre and Massonnet 1994), (Hanssen and Feijt 1996). In view of this, several multiple-antenna, multiple-frequency, and multiple-baseline based SAR interferometry techniques (Ferretti et al. 1996, 1997), (Xu et. al 1994), (Ghiglia and Wahl 1994), (Jakowatz, Wahl and Thompson 1996), (Derauw and Moxhet 1996), (Lombardo and Lombardini 1997), (Lombardini 1996, 1998) (Homer et al. 1996, 1997) have been proposed recently to reduce some of the drawbacks of the conventional two-antenna and dual-pass SAR interferometry. In this dissertation, we investigate multiple-antenna SAR interferometry for topographic mapping and apply a Bayesian model-based approach for estimating surface topography.

This introductory chapter begins with an brief overview of SAR interferometry and the various configurations commonly used for topographic mapping. Then a brief and simplified discussion

of the basic InSAR processing techniques used for deriving topographic maps is presented to highlight some of the existing drawbacks of conventional InSAR. This is followed by a brief introduction to multi-antenna/multi-baseline SAR interferometry. With this perspective, the main objectives of this dissertation are motivated and identified. Finally, a brief description of organisation of chapters in the dissertation is given.

1.1 SAR Interferometry

The first reported use of InSAR was for a study of the topography of Venus (Roger and Ingalls 1969). However, the development of modern InSAR processing techniques was spawned by the landmark paper by (Zebker and Goldstein 1986), that introduced InSAR as a spaceborne tool for topographic mapping. Since then the interest in InSAR has dramatically increased and various InSAR techniques and systems have been developed and deployed (Bamler and Hartl 1998), (Wilkinson 1997). Several applications using different configurations of InSAR have been developed in the last decade. Some of the most common configurations used are as follows (Wilkinson 1997):

- *Across Track Interferometry*: The two SAR images are acquired from two different across track trajectories. When the two passes are obtained at different times it is known as *repeat pass across track interferometry*. The other mode involves two images which are acquired at the same instance in time from two across tracks, and is known as *single pass across track interferometry*.
- *Differential Interferometry*: Repeat pass interferometry used along the same track to measure minute changes in surface height between passes. (Gabriel, Goldstein and Zebker 1989)
- *Along Track Interferometry*: Two antennas separated in the along track direction are used to measure movements in surface and estimate radial components of the surface velocity. (Goldstein and Zebker 1987) and (Carande 1992)

Across track interferometry is the most widely used InSAR technique for topographic mapping. In this dissertation, reference to SAR interferometry or InSAR for topography mapping assumes a multiple-antenna (two or more)/repeat-pass across track SAR interferometric configuration.

1.2 Topographic Mapping with SAR Interferometry

SAR interferometry techniques (Bamler and Hartl 1998) use two complex SAR images to derive topographic maps of the surface. The SAR images are acquired from slightly different angles from across track flight trajectories (Zebker and Goldstein 1986) as shown in Figure 1.1. The focused images are first accurately aligned using image registration techniques such that both images cover exactly the same area on the ground. These two registered images V_1 and V_2 are then combined ($Z = V_1 \cdot V_2^*$) to form an interference image Z commonly referred to as an *interferogram*. The phase of the interferogram image represents the phase difference between the two complex SAR images. The phase difference due to the different ranges of the two receiving antennas from the ground as a result of slightly different viewing angles of the antennas and the surface topography can only be measured modulo 2π . Therefore, the 'wrapped' (modulo 2π) interferometric phase appears as fringes in the interferogram and the spacing between fringes varies according to surface topography.

However, the terrain height is related to the absolute interferometric phase and therefore the interferometric phase has to be unwrapped. *Phase unwrapping* (PU) techniques (Goldstein et al. 1988), (Hartl and Wu 1993), (Constantini 1996), (Nico et al. 2000) are used to unwrap the interferometric phase. PU techniques employ different methodologies for optimal phase unwrapping and are mostly based on *ad-hoc* algorithms (Wilkinson 1997) which produce point estimates on the absolute phase from the measured interferometric phase. These PU methods suffer from propagation error and unwrapping errors in steep areas due to phase aliasing (Hag-

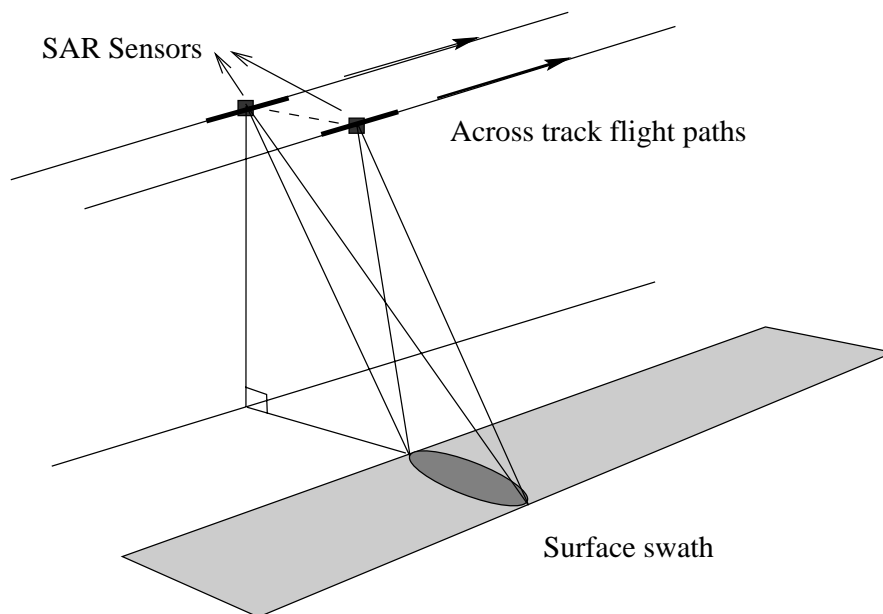


Figure 1.1: Across track InSAR geometry.

berg and Ulander 1993) that can cause significant height errors. These problems commonly associated with PU in conventional (dual-antenna/repeat-pass) InSAR can be reduced to an extent by multi-antenna/multi-baseline SAR interferometry techniques.

1.3 Multiple-Antenna SAR Interferometry

Multiple-antenna SAR interferometry is basically an extension of conventional across track interferometry using three or more antennas. Using multiple interferometric phases of different ambiguities can reduce the overall phase ambiguity and the phase-aliasing in steep areas and facilitate the phase unwrapping operation (Corsini et al. 1999). Moreover, depending on the observational geometry and SAR system parameters in some cases the phase unwrapping can be avoided and terrain height can directly be retrieved from the measured interferometric phase. Further, data-noise is also improved with multiple data measurements and as a result, accuracy of the terrain height estimates can also be improved. Also as multiple-antenna SAR interferometer is a single-pass system it does not suffer from problems of time-decorrelation and uneven atmospheric propagation delays that are encountered in repeat-pass InSAR systems.

1.4 Dissertation Objectives

In multiple-antenna InSAR the data needs to be processed such that the ambiguity diversity can be exploited to achieve reduced ambiguity and improved data-noise. Over the past few years, various researchers have proposed different techniques for processing the multiple-antenna InSAR data to obtain the topographic maps. Lombardini (1996,1998) and Corsini et al. (1999) proposed a *maximum likelihood estimator* (MLE) for estimating the absolute phase directly from the data derived from a three-antenna InSAR system. (Ferretti et al. 1996) presented a multi-baseline method for combining multiple SAR surveys for accurate DEM formation using classical ML and *maximum posteriori* (MAP) estimators. However, most point estimation techniques do not adequately address the issue of height uncertainty in the estimated values and also lack the framework for incorporating specific prior information into the estimation process.

The Bayesian inference theory provides an appropriate formal framework for combining multiple-antenna InSAR data and prior information optimally to estimate the terrain height (Wilkinson 2000). A Bayesian model-based approach to the topographic reconstruction with InSAR has been proposed by Wilkinson (1997), Wilkinson and Datcu (1998). In this dissertation, a

Bayesian model-based approach to topographic reconstruction with multiple-antenna InSAR as proposed by Dr. Wilkinson¹ is pursued. In this context, the main objectives of the dissertation are identified as follows:

- Review the theory of multiple-antenna interferometry for topographic mapping. Describe the parameterisation and formulation of topographic reconstruction as an angle of arrival estimation problem in the Bayesian inference framework as proposed by Dr. Wilkinson.
- Implement a multiple-antenna interferometric SAR simulator based on a forward-model, to generate the data required to test the angle of arrival parameter estimation methods implemented within the proposed Bayesian inference framework .
- Describe and implement the angle of arrival estimation methods in the Bayesian inference framework. Analyse the likelihood and posterior distribution of the angle of arrival parameter and summarise the posterior distribution with appropriate summary parameter(s) that quantify the uncertainty in the estimates.

1.5 Outline of Dissertation

The remainder of this dissertation are organised as follows:

- **Chapter 2** covers the basic principles of radar interferometry and discusses the main features of the multiple-antenna InSAR. Thereafter, a brief overview of Bayesian inference theory for application to estimation problems is given. Finally, the topographic mapping with multiple-antenna InSAR is described as an inverse problem and the parameterisation and formulation of the topographic reconstruction in a Bayesian inference framework as proposed by Dr. Wilkinson is described.
- **Chapter 3** presents the theory and implementation of the multiple-antenna InSAR simulator. First, various aspects of SAR imaging process are briefly reviewed. The forward model defining the geometric, radiometric and statistical characteristics of the SAR images as a function of SAR system parameters and surface properties is discussed. Then the architecture and the simulation geometry of the multiple-antenna InSAR simulator is explained. The implementation of the simulation program is described in terms of the operational details of the main processing blocks of the simulator. The input files and output files of the simulation program are also briefly described. Finally, the simulation performance is also briefly discussed.

¹Dr. A. J. Wilkinson, Department of Electrical Engineering, University of Cape Town, South Africa.

- **Chapter 4** discusses the Bayesian parameter estimation methods implemented for topographic reconstruction. The topographic reconstruction process is described in terms of position and height estimation of each point in the image. An estimation method of obtaining coherence values is discussed. Then two Bayesian methods for point position estimation using single and multiple pixel data sets are described. Point location and height estimation is illustrated by applying the Bayesian estimation methods to simulated three-antenna interferometric data and plotting the prior, likelihood and posterior probability distributions.
- **Chapter 5** presents an analysis of the likelihood and posterior probability distributions. The ambiguities in the angle of arrival and other related parameters (displacement, height and horizontal) are analysed using likelihood distributions for all antenna combinations (different baselines) in a three-antenna system. The reduced ambiguity of the three-antenna system is illustrated with the plots of appropriate likelihood and posterior distributions. A measure of accuracy of the angle of arrival estimate is calculated in terms of the standard deviation of the posterior distribution. The standard deviation of the angle of arrival estimates is analysed as a function of coherence and number of data points used in the estimation process.
- **Chapter 6** presents the conclusions and gives recommendations for further work.
- **Appendix A** contains the listing of input files and images of the simulation example described in chapter 3.
- **Appendix B** contains three-dimensional plots and images demonstrating topographic reconstruction with Bayesian estimation method.

Chapter 2

Theory and Problem Formulation

2.1 Introduction

The theory of multiple-antenna SAR interferometry is based on the basic principles of radar interferometry. In radar interferometry the relationship between the SAR system parameters, observational geometry, surface topography and the interferometric data is used to determine terrain height. Thus, first the basic principles of radar interferometry are considered and the implications of inherent ambiguity in the measured interferometric phase on height calculations are explained. The reduced-ambiguity and improved data-noise characteristics of multiple-antenna SAR interferometry are briefly described and compared to conventional dual-antenna InSAR. This is followed by a review of the Bayesian inference theory and its application to inference problems. Finally, a Bayesian model-based approach proposed by Dr. Wilkinson is described which formulates the topographic reconstruction with multiple-antenna interferometry as a parameter estimation problem.

2.2 Multiple-Antenna Interferometry Theory

This section presents a simplified discussion of the basic principles of radar interferometry as applied to multiple-antenna interferometry. The implications of ambiguities in angle of arrival and related parameters on height retrieval are explained. Reduction of ambiguities and the improved data-noise in multiple-antenna InSAR are also described.

2.2.1 Principles of Radar Interferometry

Consider a dual-antenna InSAR system and a point target as depicted in Figure 2.1. The two antennas are separated by a distance (*baseline*, b) in the across track direction (Zebker and Goldstein 1986). A pulse with a carrier frequency f_o is transmitted from antenna 1 in the direction of the surface. The point target reflects the transmitted pulse in the direction of antennas and the echo pulse is received at antenna 1 with time delay t_{d1} and at antenna 2 with time delay t_{d2} given by,

$$t_{d1} = \frac{2 \cdot r_1}{c} \quad (2.1)$$

$$t_{d2} = \frac{r_1 + r_2}{c} \quad (2.2)$$

where r_1 and r_2 are the slant ranges from antenna 1 and 2 to the point target and c is the speed of light.

The phase of the received signals at antenna 1 and 2 is related to the time delays and is expressed as,

$$\psi_1 = \arg \left\{ \exp(-2\pi \cdot f_o \cdot t_{d1}) \right\} = \arg \left\{ \exp \left(-\frac{4\pi r_1}{\lambda} \right) \right\} \quad (2.3)$$

$$\psi_2 = \arg \left\{ \exp(-2\pi \cdot f_o \cdot t_{d2}) \right\} = \arg \left\{ \exp \left(-\frac{2\pi \cdot (r_1 + r_2)}{\lambda} \right) \right\} \quad (2.4)$$

The phase difference between the two signals is of main importance in interferometry. It is referred to as the interferometric phase ψ_{12} and is defined as,

$$\psi_{12} = \arg \left\{ \exp((\psi_1 - \psi_2)) \right\} = \arg \left\{ \exp \left(-\frac{2\pi \cdot (r_2 - r_1)}{\lambda} \right) \right\} \quad (2.5)$$

By this definition the interferometric phase is limited to the principal range $(-\pi, \pi]$. In a typical InSAR geometry the baseline is several wavelengths long and therefore the measured interferometric phase is a modulo 2π measurement of the *absolute* phase φ_{12} ,

$$\varphi_{12} = \frac{2\pi \cdot (r_2 - r_1)}{\lambda} \quad (2.6)$$

This relationship between the '*wrapped*' interferometric phase and absolute phase difference is mathematically expressed as,

$$\varphi_{12} = \psi_{12} + k \cdot 2\pi \quad (2.7)$$

$$\psi_{12} = W(\varphi_{12}) \quad (2.8)$$

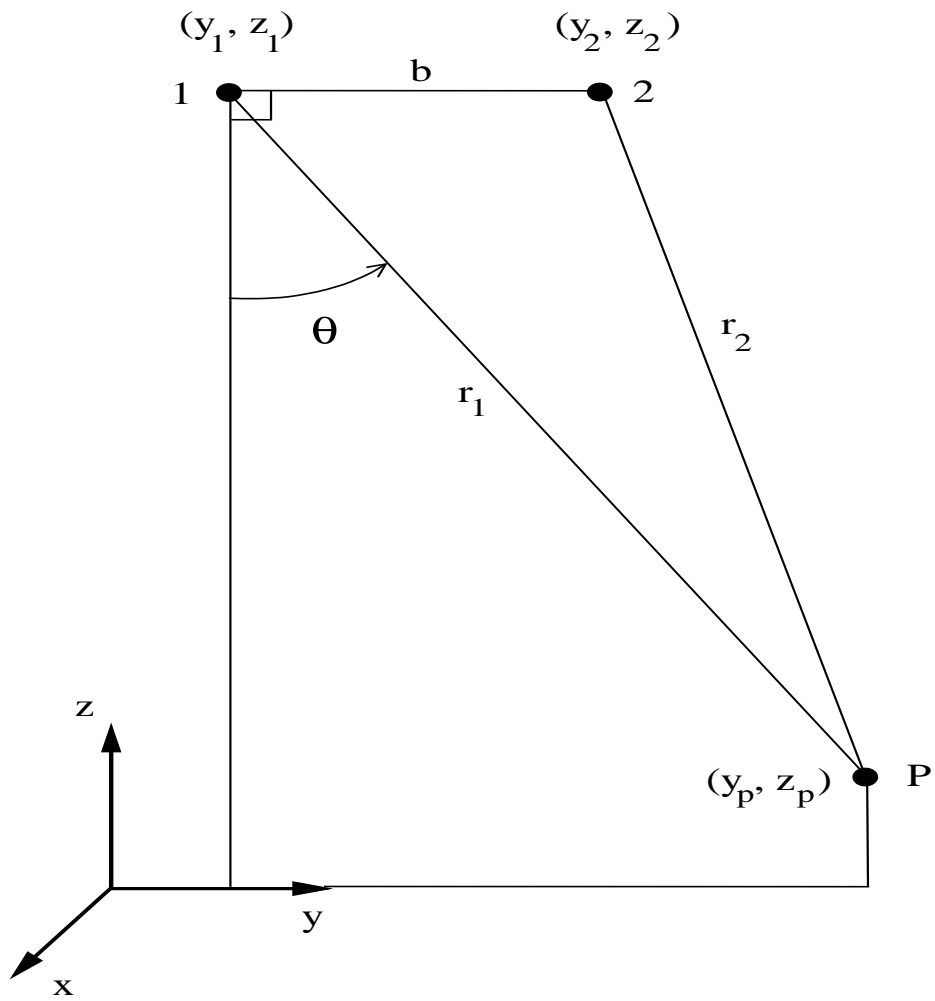


Figure 2.1: Geometry of a dual-antenna InSAR system.

where k is an integer and $W(\cdot)$ is the wrapping operator that converts the absolute phase to interferometric phase. In interferometry the terrain height is derived from the interferometric phase difference using simple geometric relationships (Rodriguez and Martin 1992). However, as the height is related to the absolute phase, hence the measured modulo 2π interferometric phase has to be unwrapped in order to recover the absolute phase (Goldstein et al.1988).

The absolute phase is related to the angle between the baseline normal and r_1 by (Wilkinson 1997),

$$\varphi_{12} = \frac{2\pi}{\lambda} \left([b^2 + r_1^2 - 2r_1b \sin(\theta)]^{\frac{1}{2}} - r_1 \right) \quad (2.9)$$

The terrain height is directly related to the angle of arrival θ , which can be expressed in terms of the absolute phase by rearranging Equation 2.9 as,

$$\theta = \arcsin \left(\frac{-\lambda\varphi_{12}}{2\pi b} + \frac{b}{2r_1} - \frac{\lambda^2\varphi_{12}^2}{8\pi^2 b r_1} \right) \quad (2.10)$$

The position of the point is determined from the angle of arrival and the antenna co-ordinates by following set of equations,

$$y_p = y_1 + r_1 \sin(\theta) \quad (2.11)$$

$$z_p = z_1 - r_1 \cos(\theta) \quad (2.12)$$

Ambiguity Analysis

The interferometric phase is an ambiguous modulo 2π measurement since the baseline is several times longer than the wavelength. This implies that the angle of arrival derived from the interferometric phase measurement is also ambiguous. The ambiguity in angle of arrival can be interpreted as an ambiguous direction of arrival of the echo signal from the point target P, as shown in Figure 2.2. The ambiguity of the angle of arrival is determined by various system parameters. The expression of ambiguity in angle of arrival is derived now.

The angular ambiguity $\Delta\theta_{amb}$ is defined as follows ($\Delta\psi_{12} = 2\pi$) (Wilkinson 1997),

$$\Delta\theta_{amb} = \left| \frac{d\theta}{d\psi_{12}} \right| \Delta\psi_{12} = \left| \frac{d\theta}{d\psi_{12}} \right| 2\pi \quad (2.13)$$

Substituting Equation 2.9 into 2.16 we get,

$$\Delta\theta_{amb} = \left| \frac{\lambda [b^2 + r_1^2 - 2r_1b \sin(\theta)]^{\frac{1}{2}}}{r_1 b \cos(\theta)} \right| \quad (2.14)$$

Using far field approximation, $r_1 \gg b$, Equation 2.14 is simplified to,

$$\Delta\theta_{amb} \approx \left| \frac{\lambda}{b \cos(\theta)} \right| \quad (2.15)$$

The ambiguities in the angle of arrival can have significant effect on errors in the terrain height. Unwrapping errors in excess of 2π (equivalent to one ambiguity) due to phase aliasing and poor phase quality (high data-noise) can culminate into a wrong choice of ambiguity for the angle of arrival and this can cause height errors. The height error Δh_{amb} , caused by wrong choice of angle of arrival by one ambiguity is directly related to the angular ambiguity as follows (Wilkinson 1997),

$$\Delta h_{amb} = \left| \frac{dh}{d\theta} \right| \Delta\theta \quad (2.16)$$

Using Equation 2.12 in Equation 2.16 we get,

$$\Delta h_{amb} = \Delta\theta \cdot r_1 \sin(\theta) \quad (2.17)$$

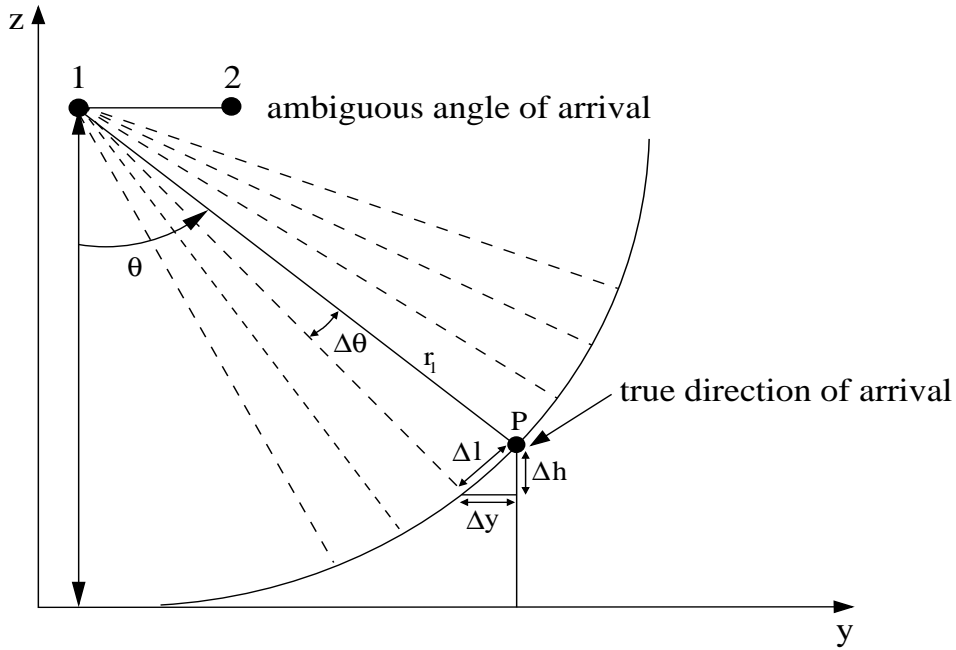


Figure 2.2: Ambiguous direction of arrival of the echo signal from the point P.

The related displacement and horizontal ambiguities as shown in Figure 2.2 are defined as,

$$\Delta l_{amb} = \Delta\theta \cdot r_1 \quad (2.18)$$

$$\Delta y_{amb} = \Delta\theta \cdot r_1 \cos(\theta) \quad (2.19)$$

2.2.2 Reduced Ambiguity with Multiple-Antennas

In multiple-antenna InSAR the addition of more antennas to the conventional dual-antenna setup gives rise to multiple baselines as opposed to a single baseline in dual-antenna InSAR. The multiple-baselines produce multiple interferometric phase measurements, each with a different ambiguity. If the antennas are arranged in an asymmetrical configuration a combination of the resulting diversity of ambiguities can be utilized to reduce the overall ambiguity of the system. In order to understand the reduction in ambiguity, let us consider a three-antenna InSAR system depicted in Figure 2.3. The asymmetrical antenna arrangement results in two long baselines between first and the second antenna, first and third antenna and a short baseline

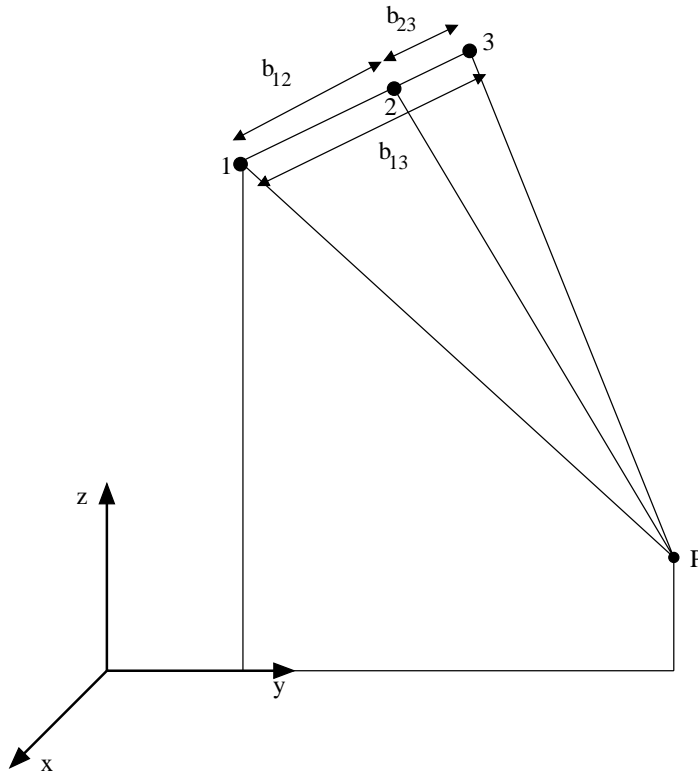


Figure 2.3: Geometry of an asymmetrical three-antenna InSAR system.

between the last two antennas. These baselines are referred to as b_{13} , b_{12} and b_{23} , with subscripts referring to the antenna pair used. Using this baseline diversity the overall ambiguity of the three-antenna system can be reduced (Lombardini 1996, 1998), (Jakowatz et al. 1996). Infact, it has been shown (Lombardini and Lombardo 1998) that for an asymmetrical factor p ,

$$p = \frac{b_{23}}{b_{13}} \quad (2.20)$$

the overall ambiguity of the three-antenna system is reduced by the factor of p (for integer p values) compared to the ambiguity of equivalent dual-antenna system with the first and third antenna. This factor is usually referred to as the ambiguity enhancement factor p . Thus the ambiguity of the three-antenna system $\Delta\theta_{123}$ is given by,

$$\Delta\theta_{123} = p \cdot \Delta\theta_{13} \quad (2.21)$$

where $\Delta\theta_{13}$ is the ambiguity of the equivalent two-antenna system with first and the third antennas. The reduced ambiguity in the three-antenna system also reduces the amount of phase aliasing in interferometric phase for steep terrain (Corsini et al. 1997,1999). As a result, the height can be estimated with improved accuracy with reduction of phase-aliasing in steep areas. Depending upon the SAR system parameters and the system geometry the reduction in ambiguity can even be enough to obtain the absolute phase directly and thus derive the height directly from the measured data without any phase unwrapping.

2.2.3 Data-Noise Improvement with Multiple Data Measurements

Multiple-antenna InSAR yields multiple data measurements which when combined properly lead to a reduction in the data-noise. The reduction in data-noise can be understood as a result of effective averaging of the multiple data measurements. The reduced data-noise increases the accuracy of height estimates in comparison to conventional InSAR.

2.3 Bayesian Inference

2.3.1 Background

Estimating information from noisy data measurements is a problem that occurs quite frequently in signal processing. The same is true for the problem of topographic reconstruction with SAR interferometry. The presence of uncertainty in the form of noise in the measured data suggests application of estimation techniques to obtain the terrain height information. There are several estimation techniques available for such purposes, most of which belong to the classical statistical paradigm. However, such classical estimation techniques lack a formal framework for incorporating valuable prior knowledge into the estimation process and rely on point estimators that are defined as some 'ad hoc' function of the measured data. Bayesian statistical inference (refer to Lee (1997), Gelman (1995) for detailed texts on Bayesian statistics and inference) on the other hand, offers a formal framework to incorporate the prior knowledge and a data-model in the estimation process.

2.3.2 Bayes Theorem

Bayesian inference is based on a well known *Bayes* theorem in probability theory that was introduced by *Rev. Thomas Bayes* (1763). The probability theorem states:

$$P(A|B) = \frac{P(A) \cdot P(B|A)}{P(B)} \quad (2.22)$$

where,

- $P(A|B) \equiv$ Conditional probability of event A taking place given that event B has already happened.
- $P(B|A) \equiv$ Conditional probability of event B taking place given that event A has already happened.
- $P(A) \equiv$ Probability of event A taking place.
- $P(B) \equiv$ Probability of event B taking place.

Given the conditional probability $P(B|A)$, the Bayes theorem allows the calculation of the conditional probability $P(A|B)$ through Equation 2.22, which is a very useful property for inference purposes. Further, it also formally allows for the inclusion of prior information via probability distribution, $P(A)/P(B)$.

2.3.3 Bayesian Parameter Estimation

Bayesian inference offers a formal approach to estimation problems. In this framework, Bayes theorem is expressed as follows,

$$P(\theta|D) = \frac{P(\theta) \cdot P(D|\theta)}{P(D)} \quad (2.23)$$

where, θ represents the parameters to be estimated from the measured data D . $P(D|\theta)$ is the conditional probability distribution of data, given a value of parameter and is referred to as the *likelihood distribution/function*. $P(\theta|D)$ is the conditional probability distribution of parameters, given data and is known as the *posterior distribution*. $P(\theta)$ represents the probability distribution of parameters, prior to data acquisition and is therefore called the *prior distribution*. The probability distribution of measured data $P(D)$, and known as the *evidence* in the context of model comparison.

These aforementioned probability distributions are key elements in the Bayesian inference theory. It is through the prior and likelihood distributions that specific user knowledge can be injected in the process of inference. The prior distribution allows for the inclusion of prior information about the parameters before data is acquired. The likelihood distribution is constructed on the basis of a statistical model of data. The combination of the prior and likelihood distributions through Bayes formula generates the posterior distribution which represents the current state of knowledge of parameters given the prior knowledge and the measured data. The posterior distribution is the final product of the Bayesian inference and conveys complete information about the parameter. Point estimates can be derived from the posterior, however they often fail to summarize the shape of the posterior. Especially, when the posterior distributions is multi-modal, point estimates are meaningless and its only with parameters that describe the shape of the posterior, that meaningful inference can be conducted. However, the classical estimation techniques still produce a point estimate in such cases, which can be misleading and can lead to totally invalid results. This further highlights the importance of the posterior distribution and the strengths of the Bayesian inference approach as opposed to

classical estimation (refer to O’Hagan (1994) for a detailed discussion of Bayesian vs classical estimation).

The likelihood distribution, as mentioned before, is based on a statistical model of the data, usually referred to as the *forward model*. The forward model predicts the probability of obtaining a data measurement given a value of a parameter. It defines the measured data by a probability distribution that is a function of the parameters of the system/process which generates data. The forward model is also particularly useful in simulating data measurements for comparisons with real data measurements. Such comparisons are useful in assessing the effectiveness of the forward model to approximate the real data generation process.

2.4 Problem Formulation

The multiple SAR images, generated by a multiple-antenna InSAR system represent a collection of noisy complex measurements of received backscatter from the imaged scene. The complex data is function of various surface scattering properties and the surface topography. Topographic reconstruction with SAR interferometry is essentially an inverse problem (Wilkinson 1997) as the process of reconstruction involves inverting the complex data in order to extract the surface topography. The presence of noise and ambiguity in the complex data suggest a statistical approach to estimate the topographic information from multiple SAR images. The Bayesian inference approach offers a suitable framework for optimal fusion of the available measured data and prior knowledge to estimate the terrain height. Hence, with a parametric representation of the surface topography, the topographic reconstruction can be formulated as a parameter estimation problem in the Bayesian inference framework, (e.g. Wilkinson and Datcu (1998)).

In the approach proposed by Dr. Wilkinson, the surface topography can be parameterised in terms of the angle of arrival of each point in the SAR image and hence the topographic reconstruction problem can be formulated as an estimation problem in the Bayesian inference framework, stated as follows,

$$\mathbf{P}(\theta|\mathbf{V}) = \mathbf{a} \cdot \mathbf{P}(\theta) \times \mathbf{P}(\mathbf{V}|\theta) \tag{2.24}$$

where, θ represents the angle of arrival of the received backscatter from each point in the SAR image and a is a constant. The angle of arrival parameter determines the position of a point on ground from which its height is determined (explained in detail in Chapter 4). $\mathbf{V} = [\mathbf{V}_1, \dots, \mathbf{V}_N]$

is the vector representing the SAR data set of N SAR images from N antennas. The prior distribution $P(\theta)$ specifies the range of angles over which the angle of arrival can be estimated unambiguously. The likelihood distribution $P(V|\theta)$, based on the forward model, predicts the likeliness of a data measurement given value of the parameter. It should be noted that this above-mentioned problem formulation in terms of angle of arrival parameter is limited to non-layover regions where each SAR image pixel represents received backscatter from only one point on ground. Nonetheless, this formulation can be easily extended to include layover regions, by representing each SAR pixel in terms of multiple angle of arrival parameter corresponding to each scatter on the ground in the layover region (Wilkinson 1997, 1998, 1999). The statistical layover-model proposed by Wilkinson (1999) can be used in the likelihood function to model the laid-over data.

2.5 Multiple-Antenna InSAR Data

SAR data from multiple-antenna InSAR systems is required for testing and analysing the Bayesian model-based approach described above. At the time of this write up the author is not aware of any operational multiple-antenna InSAR systems which could provide real data for this purpose. Therefore, the required multiple SAR data will be generated with specified antenna configuration and scene geometry using a multiple-antenna interferometric simulator based on the forward-model. The forward-model provides the necessary statistical theoretical framework for the simulator. Furthermore, the development the model-based simulator will also allow the study of effect of various antenna configurations on performance and limitations of reconstruction process. In the next chapter, the theory and implementation of multiple-antenna interferometric SAR simulator implemented is covered.

Chapter 3

Multiple-Antenna InSAR Simulator

3.1 Introduction

A two-antenna InSAR simulator was developed by Wray (2000). However, multiple-antenna interferometry requires more than two antennas and thus the existing simulator cannot be used for this purpose. To overcome the two-antenna limitation a new interferometric simulator that can simulate any number of antennas is required. This chapter covers the development of a multiple-antenna interferometric SAR simulator. It should be noted that the simulator has been designed only to be sufficiently accurate for purpose of generating data for testing the Bayesian reconstruction algorithms and has certain limitations regarding the flight path and backscatter models. The chapter is organised as follows.

First, the fundamentals of the SAR imaging operation as applicable to interferometry are briefly presented in order to gain a general understanding of the SAR imaging process. Thereafter, the SAR image simulation theory is described, based on the statistical forward model of multiple SAR images. Aspects of the forward model related to various SAR image characteristic are discussed. The basic design of the simulator based on the forward model is considered and a brief outline of the simulation program structure is given. The implementation details of the simulator are then discussed and the important aspects of the simulation program operation are explained in detail. Simulator performance in terms of the simulation times is also briefly analysed. Finally, an example simulation is described.

3.2 Principles of SAR Imaging

Some important aspects of SAR imaging such as flight geometry, ground to slant range mapping and the process of image formation are briefly introduced in order to develop a basic understanding of the imaging process. These concepts are implemented in the simulator.

3.2.1 SAR Imaging Geometry

A SAR sensor mounted on a platform like an aircraft/spacecraft scans the across the surface (range direction) moving in the along-track (azimuth) direction. The ground is viewed in a side-looking geometry with the antenna beam pointing down from one side of the platform and illuminating a swath on the ground in the antenna footprint, as shown in Figure 3.1. This SAR imaging geometry is known as *strip-map mode*, and is generally used in interferometry.

3.2.2 Ground to Slant Range Mapping

The side-looking geometry of the radar implies that a point in the ground range coordinate system is translated to the radar-centered slant range coordinate system. This ground to slant range mapping is not always one-to-one. *Shadow* and *layover* regions in SAR images are non one-to-one mappings.

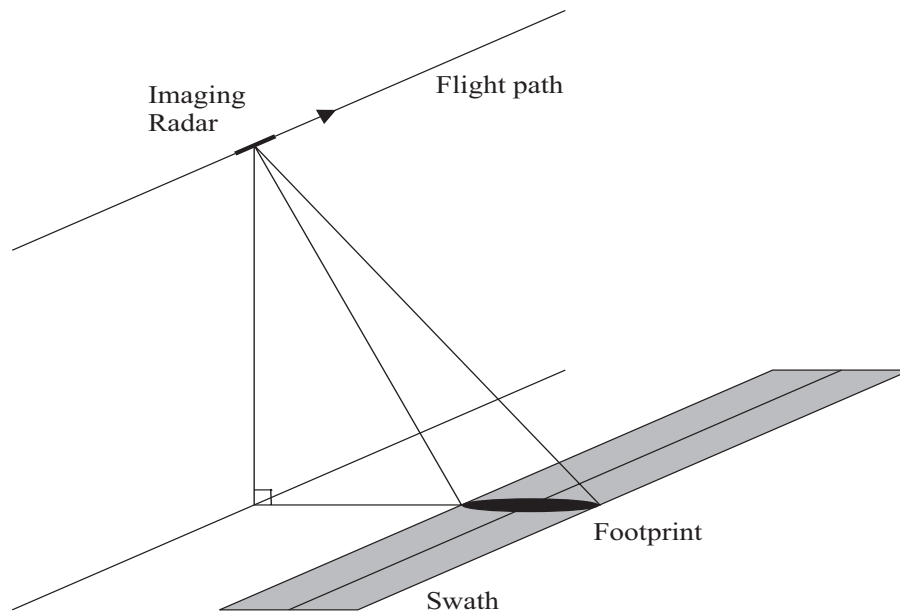


Figure 3.1: Strip-map SAR geometry

- **Layover region:** The ground to slant range conversion sometimes causes multiple points on the ground to be mapped to the same slant range. These points cannot be resolved in slant range and are said to be *laid-over*. Such regions are referred to as *layover* and the received signal is a weighted sum of the signal returns from each point on ground. Section B in Figure 3.2 shows a layover region.
- **Shadow region:** These areas are hidden from the radar's direct line of sight because of the radar viewing angle in these regions. Slant range section C in Figure 3.2 shows a typical shadow region.

3.2.3 SAR Image Formation

A SAR image is composed of signal returns scattered from the illuminated surface. Each pixel in a focused SAR image represents the signal return from a patch on the ground, referred to as a 'resolution cell'. A resolution cell contains several point scatterers and the received complex signal V is expressed as the weighted sum of all the returns,

$$V(x, R) = \sum_i a_i \cdot e^{j\psi_i} \quad (3.1)$$

where a_i is the amplitude and $\psi_i = -\frac{4\pi r_i}{\lambda}$ is the phase of the complex signal return from the i^{th} point scatterer at range r_i . x and R represent the azimuth and the slant range image coordinates respectively. The combined return from multiple scatterers in a resolution cell can be represented by an equivalent signal return as,

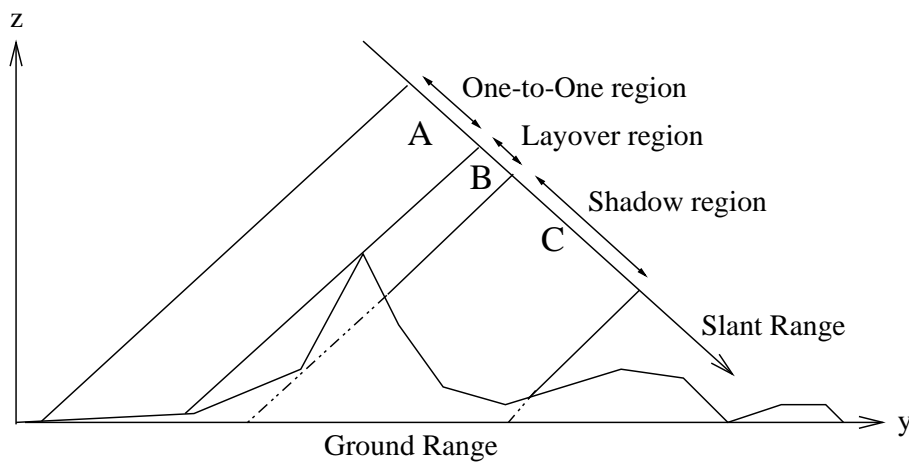


Figure 3.2: Ground range to slant range mapping for side-looking geometry.

$$V(x, R) = A(x, R).e^{j\psi(x, R)} \quad (3.2)$$

where the signal amplitude A fluctuates in accordance with the distribution of scatterers on the surface characterised locally by its equivalent radar cross section coefficient σ° (Ulaby et al. 1982). The scene can be modeled as a *distributed target*. The SAR image formation process can therefore be represented by the returns from a scene, a distributed target, transformed by the radar system's point response with addition of receiver noise and black body radiation from the scene. This process is illustrated in Figure 3.3.

3.3 Properties of SAR Images

A SAR image is a complex representation of various physical and geometrical properties of the imaged scene. The noisy nature of a SAR image can be understood by modeling it as a random process with parameters that are functions of various surface properties. Furthermore, the correlation between several SAR images can be described by using a joint statistical model, which is adopted as the forward model for multiple-antenna SAR image generation. These statistical aspects of SAR images and the forward model components are discussed in detail in the following section.

3.3.1 SAR Image Statistics

In a resolution cell, the scatterers are oriented randomly. For a high number of random scatterers the signal return can be modeled as a complex circular Gaussian random process, on the assumption that there is no one dominant scatterer (Oliver and Quegan 1998). This assumption is valid for most regions in a scene, such as, forests, farmlands, mountains etc. In urban areas this assumption is not always valid due to the presence of artificial objects that can produce

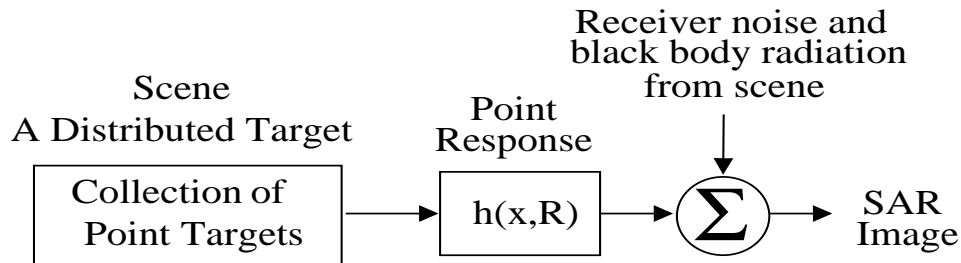


Figure 3.3: SAR image formation model.

strong signal returns. However, for a typical scene the assumption holds in most regions and therefore the Gaussian model is applicable. Each pixel in a SAR image can be represented by a zero-mean complex circular Gaussian random variable $V(x, R)$,

$$V(x, R) = I(x, R) + jQ(x, R) \quad (3.3)$$

The real and imaginary components of the complex signal are independent, identically distributed, zero-mean Gaussian random variables,

$$\begin{aligned} I(x, R) &\sim N(0, \sigma_I) \\ Q(x, R) &\sim N(0, \sigma_q) \end{aligned} \quad (3.4)$$

where standard deviation $\sigma_I = \sigma_Q$ for both real and imaginary components.

The intensity/power of the signal return for the pixel at (x, R) is proportional to the variance of the random variable,

$$Intensity(x, R) \propto E \left\{ |V(x, R)|^2 \right\} \propto \sigma \quad (3.5)$$

where the variance is directly proportional to the radar cross section, σ .

3.3.2 Joint SAR Image Statistics: Forward Model

SAR interferometry uses two or more SAR images of the same scene to generate interferograms. These SAR images are correlated as they are formed over the same scene from slightly different viewing angles. The statistical model for a single SAR image can be extended to a set of N images, which can be represented by (Wilkinson 1997) a joint complex circular Gaussian PDF $P(\mathbf{V})$,

$$P(\mathbf{V}) = \frac{\mathbf{1}}{\pi^N |\mathbf{K}|} \exp \left(-\mathbf{V}^\dagger \mathbf{K}^{-1} \mathbf{V} \right) \quad (3.6)$$

where the column vector $\mathbf{V} = (\mathbf{V}_1, \mathbf{V}_2, \dots, \mathbf{V}_{N_{\text{images}}})$ represents the set of N images. \mathbf{V}^\dagger is the conjugate transpose, $\mathbf{K} = \mathbf{E} \left\{ \mathbf{V} \cdot \mathbf{V}^\dagger \right\}$ is the complex covariance matrix. The complex covariance matrix \mathbf{K} is composed of variance terms related to the magnitude of the surface reflectivity and pairwise complex covariance terms representing the correlation between images.

Assuming that all the images are accurately focused, registered, and sampled at the Nyquist rate, each pixel in an image becomes statistically independent of every other pixel in the same image and the joint distribution can be written as a product (Wilkinson 1997),

$$P(\mathbf{V}) = \prod_{i=1}^{N_{samples}} P(V_1(i), \dots, V_{N_{images}}(i)) \quad (3.7)$$

$$= \prod_{i=1}^{N_{samples}} \frac{1}{\pi^N |\mathbf{K}_i|} \exp\left(-\mathbf{V}_i^\dagger \mathbf{K}_i^{-1} \mathbf{V}_i\right) \quad (3.8)$$

where $\mathbf{K}_i = cov(V_1(i), \dots, V_N(i))$, is the covariance matrix for i^{th} pixel location. This implies that the set of all i^{th} pixels in N images are jointly complex circular Gaussian random variables.

This joint distribution represents the forward model that is used to obtain signal returns given scene and system parameters for simulating SAR images with the right correlation structure. The complex covariance matrix \mathbf{K} is the parameter that defines the joint distribution and carries information about the various scene and system properties. In the next section, the complex covariance matrix is described as a function of various system and scene parameters.

3.3.3 Complex Covariance Matrix

The complex covariance matrix completely defines the relationship between the N images. The matrix is defined as,

$$\mathbf{K} = \begin{bmatrix} E\{|V_1|^2\} & E\{V_1 V_2^*\} & \dots & E\{V_1 V_N^*\} \\ \vdots & & \ddots & \\ E\{V_i V_1^*\} & & & \vdots \\ \vdots & & & \ddots \\ E\{V_N V_1^*\} & \dots & E\{V_N V_j^*\} & E\{|V_N|^2\} \end{bmatrix} \quad (3.9)$$

Each covariance element in the matrix is equal to the covariance between a pair of images and is related to the correlation coefficient via,

$$\gamma_{ij} = \frac{E \{V_i V_j^*\}}{\sqrt{E \{|V_i|^2\} \cdot E \{|V_j|^2\}}} \quad (3.10)$$

$$\gamma_{ij} = |\gamma_{ij}| e^{j\psi}$$

The complex correlation coefficient γ_{ij} ($0 \leq |\gamma_{ij}| \leq 1$), usually referred to as coherence, expresses the correlation between images i and j . A value of 1 means complete correlation, i.e. the two images are statistically identical, whereas a value of 0 implies full decorrelation indicating that the two images are totally unrelated or statistically independent. Phase, ψ , of the correlation coefficient is equal to the interferometric phase formed by the two images. The two terms in the denominator of the correlation equation 3.10 represent the variances, that are equal to the received power of the signals.

3.3.4 Coherence Model

The coherence is an important parameter in interferometry and it determines the quality of the interferometric phase. It is expressed as a product of three coherence components (Rodriguez and Martin 1992), (Wilkinson 1997), (Bamler and Hartl 1998),

$$|\gamma| = \gamma_{time} \cdot \gamma_{geometry} \cdot \gamma_{snr} \quad (3.11)$$

where γ_{time} , is the time coherence used to measure the time-decorrelation effect in repeat-pass interferometry. The geometric coherence, $\gamma_{geometry}$, is due to the spectral shift from different viewing angles of the radar. The γ_{snr} coherence represents the signal to noise contribution to the overall coherence value. Note that γ_{reg} , the decorrelation factor caused by misregistration can be made small and has been ignored in the coherence equation.

3.3.4.1 Temporal coherence

The factor γ_{time} in the range $0 \leq |\gamma_{time}| \leq 1$, is introduced to model the extent of temporal decorrelation. In repeat-pass interferometry the changes in scene over time between passes introduce decorrelation in the acquired SAR images. These changes can be due to several factors such as surface deformation, vegetation growth, landslides to name a few. Usually, longer times between passes increases the decorrelation.

3.3.4.2 Geometric coherence

Geometric coherence is a measure of decorrelation due to baseline. The two different viewing angles introduce a spectral shift (Prati and Rocca 1992,1993) such that the spectrum of the return signals in one image is shifted with respect to the one in the other image by an amount which is directly proportional to the baseline. Assuming zero squint radar geometry, the geometric coherence can be written as a function of range spectral shift (valid in the range $-BW \leq \Delta f_{range} \leq BW$),

$$\gamma_{geometry} = \frac{BW - |\Delta f_{range}|}{BW} \quad (3.12)$$

where BW is the radar pulse bandwidth and Δf_{range} is a slope-induced spectral shift in the range direction. This spectral shift is derived here as a function of various incidence angles and the radar operating frequency f_o and is written as,

$$\Delta f_{range} = f_o \left[1 - \left(\frac{\sin(\theta_{t1}) + \sin(\theta_{r1})}{\sin(\theta_{t2}) + \sin(\theta_{r2})} \right) \right] \quad (3.13)$$

This is a generalized formula, which takes into account that the received signal may be transmitted from an antenna other than the receiving one, and hence the four incidence angles (one each for two transmitting/receiving antenna pairs) as shown in Figure 3.4. It is evident from Equation 3.13 that the longer the baseline the greater the difference between incidence angles of two receiving antennas and therefore the larger the spectral shift.

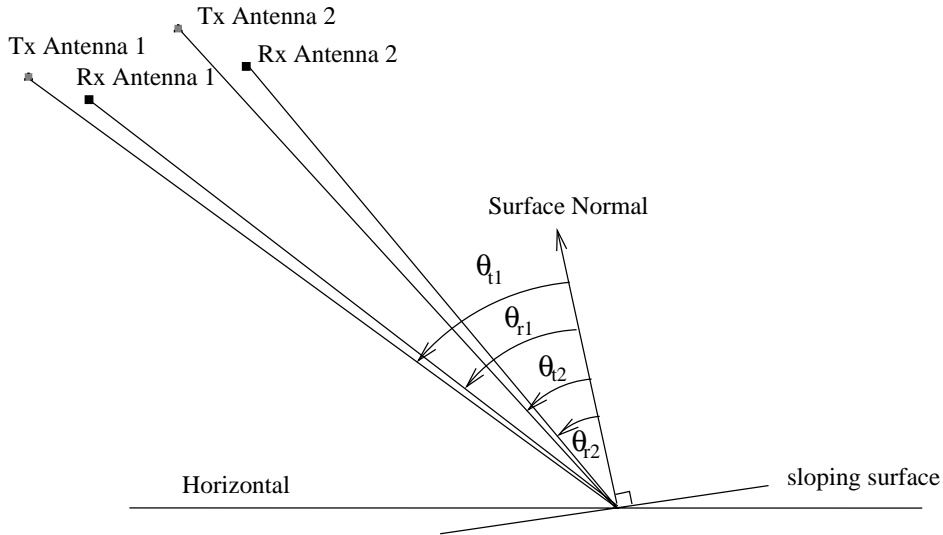


Figure 3.4: Geometry depicting incidence angles.

3.3.4.3 Receiver noise coherence

The finite signal to noise ratio also contributes to the coherence value and is defined as (Zebker and Villasenor 1992),

$$\gamma_{snr} = \frac{1}{\sqrt{1 + \frac{1}{SNR_1}}} \cdot \frac{1}{\sqrt{1 + \frac{1}{SNR_2}}} \quad (3.14)$$

where SNR_1 and SNR_2 are the signal to noise ratios of the two SAR images.

3.3.5 Received Power

The variance term in the coherence Equation 3.10 is proportional to the total received power, equal to the sum of the received signal power P_r , and the noise power P_{noise} ,

$$E \{ |V|^2 \} \propto P_r + P_{noise} \quad (3.15)$$

The received signal power is dependent on several factors such as surface reflectivity, local slope of terrain and distance from radar, and is given by the radar equation (Skolnik 1981) as,

$$P_r = \left(\frac{P_t G^2 \lambda^2}{(4\pi)^3} \right) \frac{\sigma}{R^4} \quad (3.16)$$

where P_t is the transmitted power, G is antenna gain, R is slant range to target, σ is the radar cross section and λ is the wavelength. This expression assumes a homogeneous region where all parameters are constant across the resolution cell. The radar Equation 3.16 can be rewritten in terms of slant range dependent parameters as,

$$P_r \propto \frac{\sigma(\theta_{inc})}{R^4} \quad (3.17)$$

After range correction, the $\frac{1}{R^4}$ slant range term is removed from Equation 3.17, making the received power directly proportional to the radar cross section, which is a function of the surface radar cross section coefficient σ° , and incidence angle θ_{inc} . The received noise power, P_{noise} , in Equation 3.15, is slant range dependent (in the range compensated image) and is determined by the SNR and received signal power for a particular slant range.

3.4 Simulator Architecture

The simulator uses several input parameters to specify radar system parameters, scene geometry and scene model. These include antenna position information, antenna transmission/receiving arrangement, radar system parameters, input DEM file and, variables describing system geometry. The simulator produces a complex SAR image for every antenna, and if requested, the coherence map for all image pairs, a slant range height map, layover and shadow maps and, an angle of arrival map. It also produces a log file containing all the information pertaining to the simulation run. A block diagram representation of the simulator is shown in Figure 3.5

3.5 Simulation Geometry

The scene is represented by a *digital elevation model* (DEM) which is a collection of height points on an evenly spaced rectangular grid. The antenna trajectory model used for the reference antenna assumes a straight flight path parallel to the DEM. Further, for every other antenna the flight path is assumed to be parallel to the reference antenna trajectory. This antenna trajectory model used implies that the DEM is parallel to antenna flight path and each DEM line is mapped into the corresponding slant range line. The imaging geometry for a typical simulation is depicted in Figure 3.6.

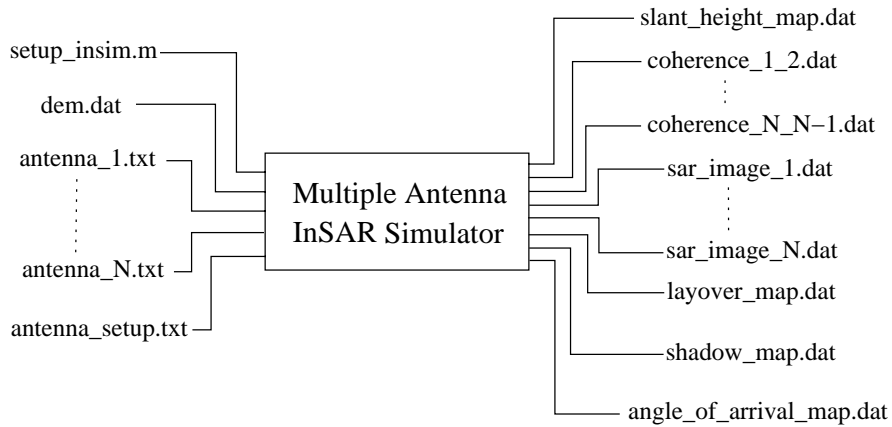


Figure 3.5: Simulator architecture.

3.6 Simulation Program

The simulation program directly simulates the scene statistics using the the DEM and SAR system parameters. These scene statistics are used to define the joint distribution which forms the forward model. Then the SAR images are obtained by generating samples from the joint distribution. This simulation process is depicted in Figure 3.7. The simulator program consists of several processing steps involving various system and surface parameters. The simulation is setup by the system and scene parameters in the input files specified by the user.

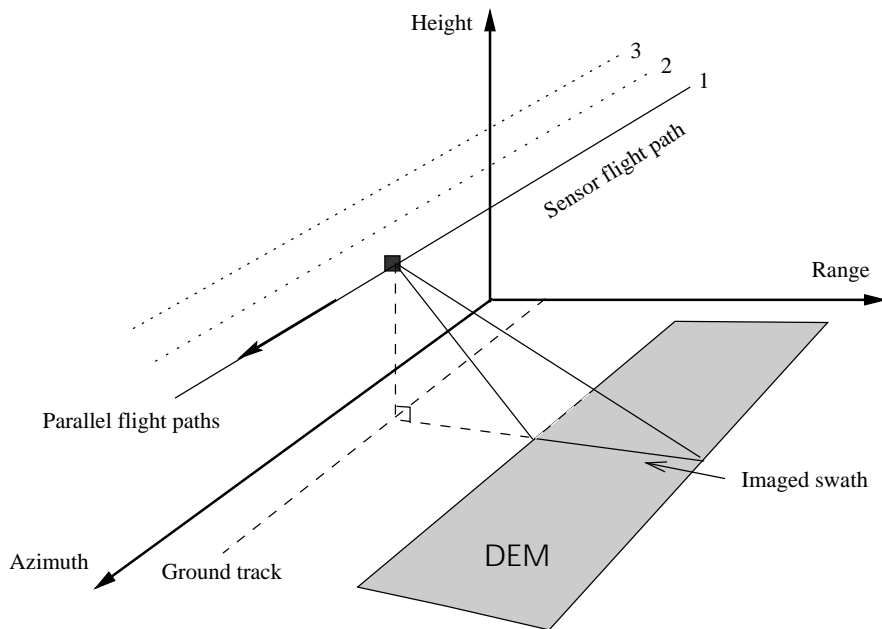


Figure 3.6: Imaging geometry of a typical simulation showing antenna flight-paths and the imaged DEM.

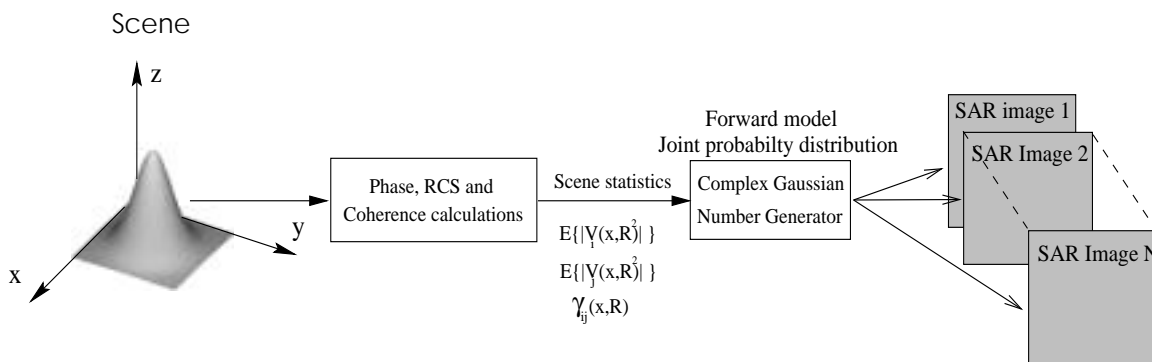


Figure 3.7: SAR image generation with forward model.

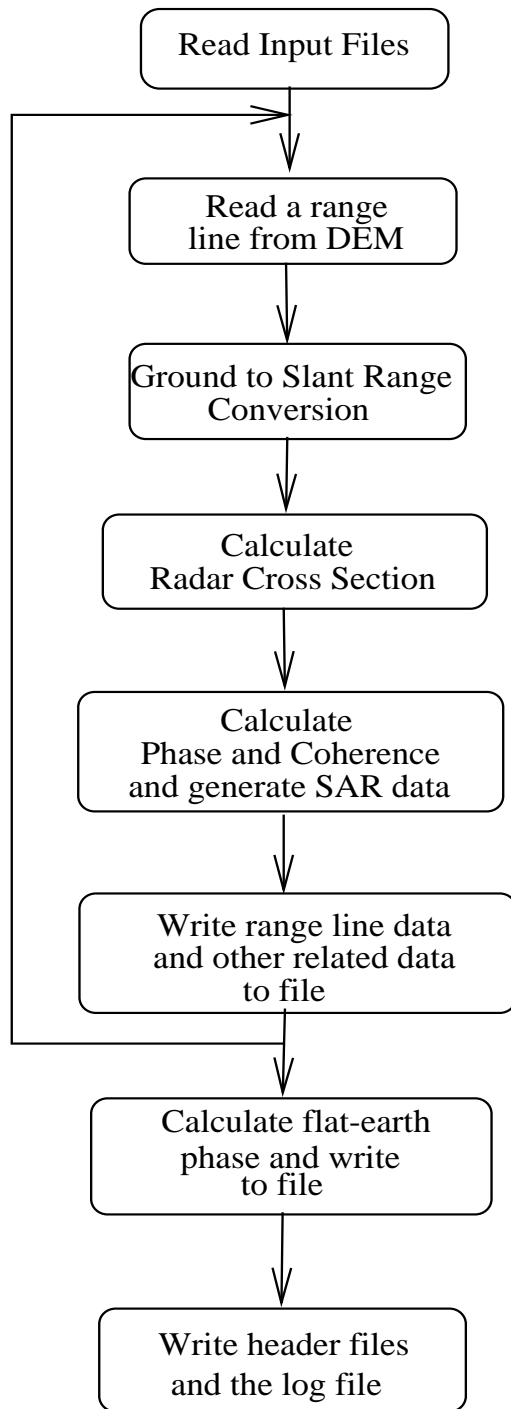


Figure 3.8: Flow chart of the simulation program.

3.6.1 Input Files

The input to the simulation program consists of several ASCII files and a binary file containing the actual DEM. The main input file is an ASCII file called *setup_insim.m* and specifies the following parameters:

- Directory path where antenna specification files are located;
- The number of antennas;
- Filename specifying the antenna transmission/receiver configuration file;
- Filename specifying the DEM file;
- DEM dimensions and actual grid spacing;
- The start and end azimuth line number for simulation;
- The number of slant range bins to be simulated;
- The desired slant range spacing for the SAR image to be produced;
- The near slant range where simulation must start;
- The desired signal to noise ratio of the image, specified for mid-swath (assuming flat surface);
- The speed of propagation for transmitted signal;
- Directory where simulation outputs are stored;
- Flags requesting optional simulation outputs: flat earth, coherence map, slant range height map, layover and shadow maps, angle of arrival map and the absolute phase map.

The other ASCII files include the antenna files, which contain the antenna coordinates, radar frequency and bandwidth. Each antenna is described in a separate file, e.g. two antennas will be specified by two files, *antenna_1.txt* and *antenna_2.txt* respectively. The antenna transmission and receiving configuration is described in an ASCII file, *antenna_setup.txt*, specifying the transmitting antenna number for every antenna used in the simulation.

3.6.2 Simulation Processing Steps

A flow chart of the simulation program is shown in Figure 3.8. The various simulation processing steps in the flow chart are discussed in the following sections which explain the complete simulation process starting from a DEM and resulting in the simulated SAR images. During the simulation each range line in the DEM is read and simulated one at a time, and the resulting simulated range line data is written to the output file before proceeding to the next range line. The range line read from the DEM consists of evenly spaced height samples of terrain in ground range coordinates. These ground range points need to be mapped to radar centered slant range coordinates due to the side-looking imaging geometry. The mapping is performed by the ground to slant range conversion module described in the following section.

3.6.2.1 Ground to slant range conversion

This module accepts a range line as an array of height values in ground coordinates, together with the reference antenna coordinates. Starting with the near slant range, arcs of equal distance from the reference antenna are defined, separated by the slant range spacing. The intersections of the slant range arcs with line segments joining discrete height points in the range line are then calculated. Figure 3.9 shows constant slant range arcs intersecting with the line segments connecting the discrete height points along the range line. In layover regions a slant range arc intersects with two or more points, as seen for the first slant range arc in Figure 3.9. In shadow regions, the intersections found are not recorded. The output produced consists of range bins from near to far slant range. Every slant range bin contains information about the intersection point: such as the y, z co-ordinates, local terrain slope and local surface normal for each intersection point. All the calculations are performed in the y, z zero-doppler plane. The code for this module was adapted from the '*solver*' procedure of the two antenna simulator written by (Wray 2000) with an addition of surface normal calculations and other minor changes.

3.6.2.2 Radar cross section

The magnitude of the average return from a resolution cell at a particular range bin is given by radar cross section figure, RCS. This module calculates the RCS for each slant range bin from near to far slant range for each antenna separately.

The calculations are based on the following definition of RCS (σ),

$$\sigma = \sigma^o A_{GR} \tag{3.18}$$

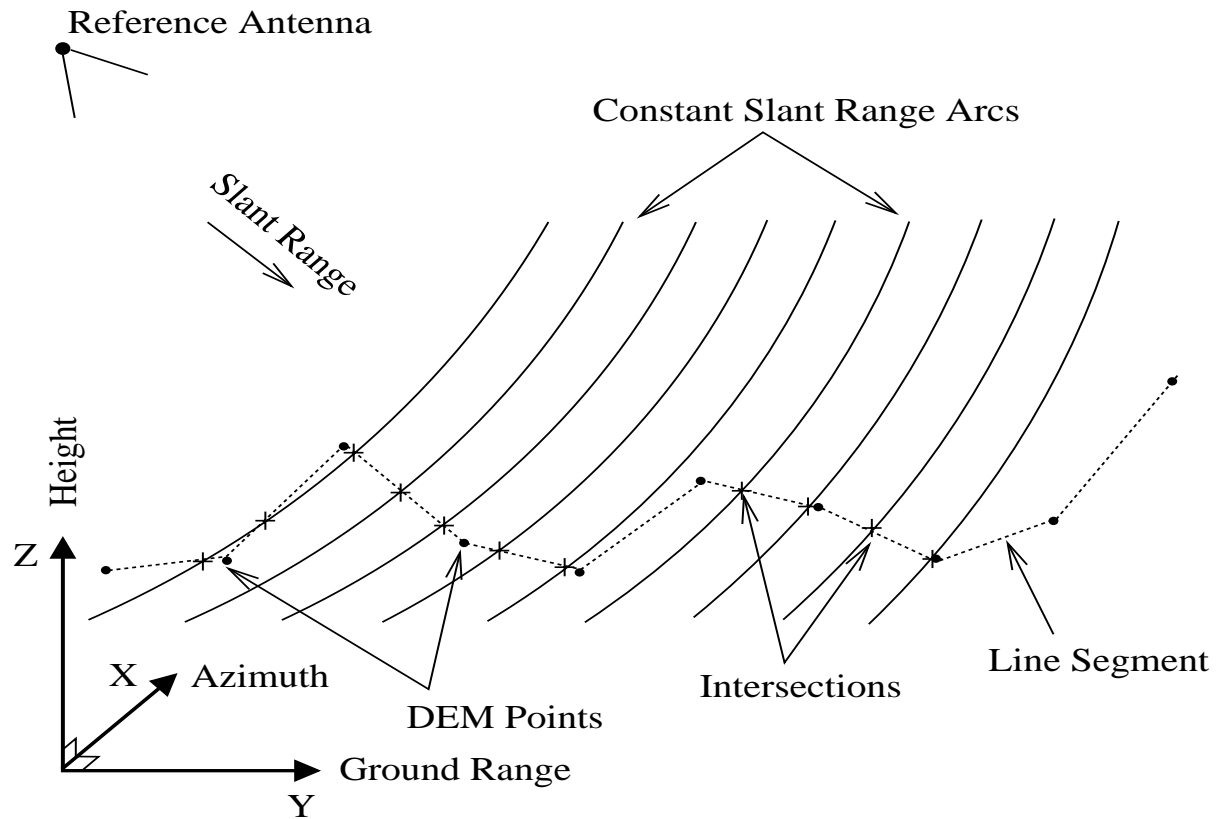


Figure 3.9: Ground to slant range conversion.

where radar cross section coefficient σ^o , is the unit-less backscatter coefficient and A_{GR} , is the ground resolution cell area in units of m^2 . The radar cross section coefficient varies with incidence angle, surface roughness, moisture level and terrain cover type. The model used for calculating the sigma nought is only incidence angle dependent, as other surface parameters are not readily available. The sigma nought is calculated using a simple geometric model,

$$\sigma^o = \frac{\eta}{\sin(\theta_{inc})} \quad (3.19)$$

where θ_{inc} is the incidence angle: angle between the incident ray (slant range vector) \hat{r} , and the local surface normal \hat{n} , as shown in Figure 3.10. η is the surface reflectivity coefficient and has a value of unity under the assumption of homogeneous terrain¹. The incidence angle is found using,

$$\theta_{inc} = \cos^{-1} \left(\frac{\hat{r} \cdot \hat{n}}{|\hat{r}| |\hat{n}|} \right) \quad (3.20)$$

The ground resolution cell area is the actual area illuminated by the radar on the ground and is calculated as the projection of the fixed slant range resolution cell area onto the ground. Using the slant range vector \hat{r} , surface normal vector \hat{n} , and the antenna velocity vector \hat{v} , shown in Figure 3.10, the projected ground area A_{GR} is given as (Wilkinson 2000),

$$A_{GR} = \frac{|(\hat{v} \times \hat{n}) \times (\hat{r} \times \hat{n})|}{(\hat{v} \times \hat{n} \cdot \hat{r})^2} A_{SR} \quad (3.21)$$

where A_{SR} is the slant range resolution cell area and is equal to the product of slant range spacing and the azimuth spacing.

3.6.2.3 Phase and Coherence

The phase of the signal return from near to far slant range is calculated for all the simulated antenna positions. The phase is due to the delay in distance transversed by the wave from the transmitting antenna to the target and from target to the receiving antenna. For each slant range these distances are calculated using antenna and target positions. The received phase ψ is given by the following equation,

¹the simulator can be extended to model different terrain types with different values of η for each typical terrain type.

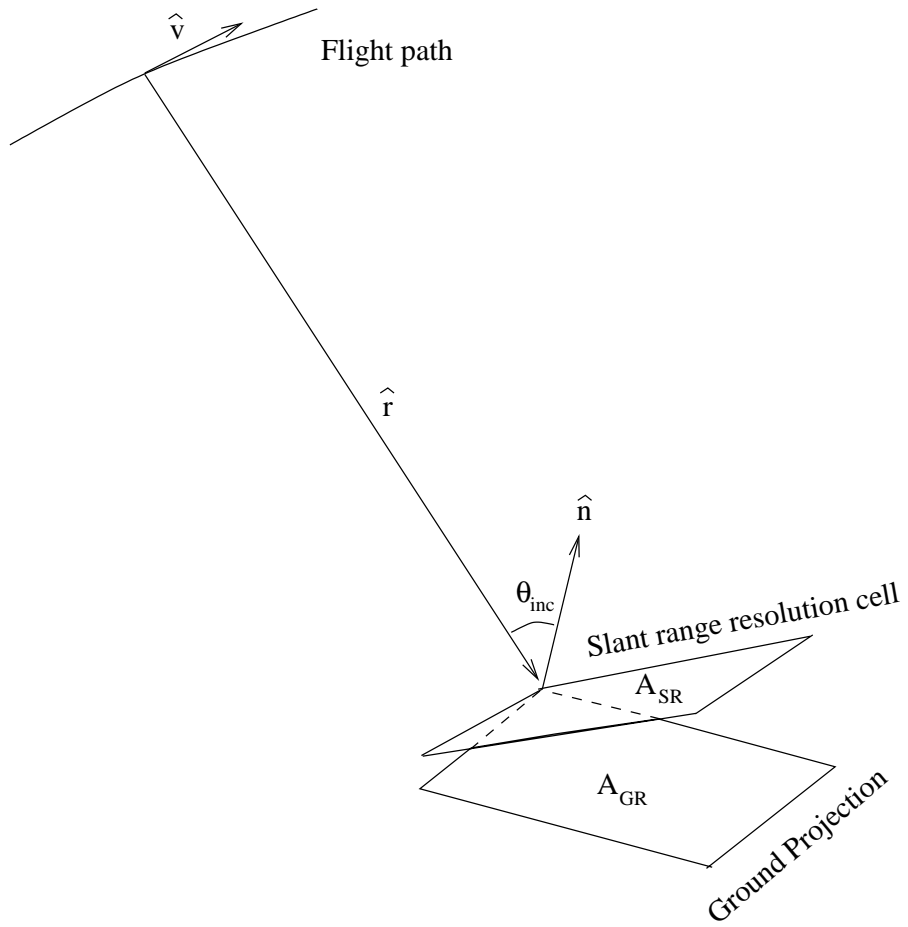


Figure 3.10: Slant to ground projection geometry.

$$\psi = W \left(-\frac{2\pi(R_{tx} + R_{rx})}{\lambda} \right) \quad (3.22)$$

where R_{tx} is the distance from transmitting antenna to the target, R_{rx} is the distance from target to the receiving antenna and λ is the radar wavelength.

The magnitude of the coherence for each antenna pair is obtained using Equation 3.10. It is calculated from near to far slant range as a product of the three factors. The temporal coherence factor is assumed uniform (equal 1 for single-pass multiple antenna system) over the swath width. The geometric coherence is calculated using the formula in Equation 3.13. The four incident angles are obtained using the geometry specified by the antenna and target positions and the local terrain slope. The coherence part due to the receiver noise is found by calculating the signal to noise ratios for each antenna as a function of slant range. The signal to noise ratio is obtained using (Wilkinson 2000),

$$SNR = b \cdot \frac{\sigma}{R^3} \quad (3.23)$$

b is the system constant, R is the slant range and σ is the RCS. In layover regions the coherence is calculated using a coherence model for layover regions proposed by Wilkinson (1997). It predicts the coherence in a layover region is a weighted sum of coherence γ_l , of individual layover regions. The coherence for L laid-over regions is given as,

$$\gamma_s = \frac{\sum_{l=1}^L \gamma_l \sqrt{E \{ |V_{i,l}|^2 \}} \cdot E \{ |V_{j,l}|^2 \}}{\sqrt{\sum_{l=1}^L E \{ |V_{i,l}|^2 \}} \sum_{l=1}^L E \{ |V_{j,l}|^2 \}} \quad (3.24)$$

3.6.3 Data generation from joint distribution

With calculated values of RCS, coherence and phase the covariance values for each antenna pairing are obtained from Equation 3.10. These covariance values are used to form the covariance matrix which defines the joint distribution as given by Equation 3.6. The joint distribution is used to generate SAR data with the correct statistical, radiometric and geometric properties. The data is generated for each range bin separately. Samples from the joint complex circular Gaussian distribution are generated using the Cholesky decomposition method (MATLAB's Cholesky decomposition function). This involves generating the N independent complex random numbers from a standard normal distribution with a random number generator, where N is the number of antennas being simulated. Cholesky decomposition is applied to the covari-

ance matrix of the joint distribution to obtain a transform matrix that transforms the set of independent random numbers into correlated random numbers. This transform matrix is then applied to the set of N standard normal complex random numbers producing a set of correlated random numbers as described by the joint distribution.

3.6.4 Output Files

The outputs produced by the simulator are stored in files in the directory specified by the user. The simulator writes the following data into files:

- The simulated complex SAR image for each antenna.
- The simulation log file containing various simulation parameters.

and according to the specific user request the following simulation products are also written to files:

- The coherence map for each antenna pair.
- The flat earth complex SAR image for each antenna.
- The layover and shadow maps.
- The angle of arrival map for the reference antenna.
- The slant range height map of simulated DEM.

3.7 Simulator Performance

The simulation program has been implemented in MATLAB. The current implementation has tolerable simulation times for small (64 x 64 pixels) to medium (1024 x 1024 pixels) simulations. However, as MATLAB is basically an interpreted language its computational efficiency is somewhat limited and this quickly becomes a bottleneck for very large simulations in terms of the simulation times. Table 3.1 shows some timing results of simulation image size vs simulation times (on an Intel 266 MHz system running Windows NT). The current simulation program implementation can be made more time efficient, particularly so for large simulations (20,000 x 20,000 pixels), using a compiled language (such as C or FORTRAN) which offers much greater computational speeds.

3.8 Simulation Example

To illustrate a typical multiple-antenna InSAR simulation, a three-antenna airborne SAR system and a mound DEM are simulated. The SAR system and imaging geometry parameters used in the simulation are tabulated in Table 3.2. The input files corresponding to this simulation are listed in Appendix A. The mound DEM parameters are specified in Table 3.3. The simulation produces several output images including three complex SAR images for each antenna, the flat earth phase images, coherence image for each antenna pair, angle of arrival and layover and shadow maps. These simulated images are shown in Appendix A.

Simulation Image Size [pixels]	Simulation Time [mins]
64 x 64	1.4
128 x 128	5.2
512 x 512	93
1024 x 1024	380

Table 3.1: Simulation times for various image sizes.

Parameter	Value
Antenna 1 and 3 separation	3.0m
Antenna 1 and 2 separation	2.5m
Antenna 2 and 3 separation	0.5m
Airborne Platform Altitude	9000m
Incident angle (mid-swath)	48.5°
Swath width (slant range)	6400m
Slant range (mid-swath)	13580m
Frequency	5.3GHz
Bandwidth	20MHz
Range pixel spacing	12.5m
Azimuth line spacing	12.5m

Table 3.2: SAR system and imaging geometry parameters.

Surface DEM Parameter	Value
DEM Maximum height	1000m
DEM Minimum height	0m
DEM range spacing	12.5m
DEM azimuth spacing	12.5m

Table 3.3: Surface DEM parameters.

Chapter 4

Bayesian Topographic Reconstruction Methods

4.1 Introduction

Topographic reconstruction with multiple-antenna SAR interferometry has been outlined as an parameter estimation problem in Chapter 2. This chapter describes the model-based Bayesian inference method proposed by Dr. Wilkinson for estimating topography of the surface from the multiple-antenna SAR data. In the context of the estimation problem the selection of the parameter to be estimated is first considered. Then the topographic reconstruction of the surface is explained in terms estimating the position of individual ground point with the angle of arrival parameter. Methods of obtaining coherence values required in the estimation methods are considered. Then a method for estimating the location of a point using a single pixel data set is described. An extension of this method which uses multiple pixel data in the point position estimation process is also discussed for obtaining more reliable estimates. These methods are then applied to simulated SAR data for a three-antenna InSAR system to illustrate the relevant probability distributions for obtaining point location (and height) estimates.

4.2 Parameter Selection

Topographic reconstruction is the process of reconstructing the surface height information from SAR images. The topography of a surface can be described by the position of points on the ground (Section 2.4). The location of a point on the ground is fixed by the *angle of arrival* of the received echo and the slant range distance from the antenna. This angle of arrival is defined

as the angle between the vertical and the path of signal return from the point on the ground to the reference antenna as shown in Figure 4.1. Thus for a given slant range, the angle of arrival parameter can be used to calculate the location of a point. Therefore, angle of arrival is a suitable parameter for inferring the location of a point from the SAR data. From the geometry shown in Figure 4.1 the position of the point P is defined with following set of equation,

$$z_p = z_a - r \cdot \cos(\theta) \tag{4.1}$$

$$y_p = y_a + r \cdot \sin(\theta) \tag{4.2}$$

where z_a is the height of the reference antenna above the ground and r is the slant range. The height h_p of the point P at a slant range r is defined as equivalent to the z_p coordinate of the point position.

4.3 Coherence Estimation

The Bayesian estimation method requires coherence values for calculating the likelihood probability distribution. The optimal method of obtaining coherence would be to estimate it through the Bayesian estimation process as another parameter. However, with each additional parameter the complexity of Bayesian estimation method increases in terms of computation time and dimensionality of the posterior distribution making this approach inefficient. Therefore,

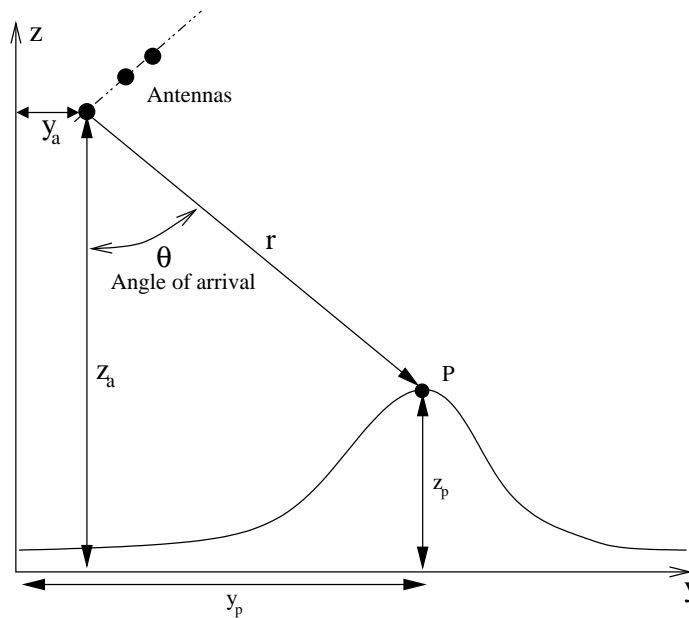


Figure 4.1: System geometry showing the relationship between the surface height and angle of arrival

the coherence values are pre-estimated. Two methods for obtaining the coherence values are identified.

4.3.1 Simulation Coherence

The simulator produces coherence values for each antenna pair. These coherence values are calculated from the theoretical model which defines the coherence for given system and scene parameters.

4.3.2 Maximum Likelihood Coherence Estimator

The *maximum likelihood estimator* MLE, (a classical estimator) is coherence estimator usually used for obtaining estimates of coherence values from SAR images. It is derived under the assumption that all M independent samples used in the estimation have identical statistics. An improved version of the MLE coherence estimator (Touzi et al.1999) is defined as,

$$|\gamma_{ij}| = \frac{\left| \sum_{n=1}^M V_i(n) \cdot V_j^*(n) \cdot e^{-j\psi_{ij}(n)} \right|}{\sqrt{\sum_{n=1}^M |V_i(n)|^2 \cdot \sum_{n=1}^M |V_j(n)|^2}} \quad (4.3)$$

where $e^{-j\psi_{ij}(n)}$ is phase correction factor used to compensate for the local interferogram phase slope due to non-flat surface. To phase correction factor is calculated using the terrain slope factor β obtained from the fringe rate (it is found by transforming the sample interferogram phase data into frequency domain). The numerator in Equation 4.3 represents the estimated covariance using the M samples, while the denominator term consists of estimates of the two variance terms. The M samples used in the estimate are drawn from a rectangular window centered about the point in the image for which the coherence value is to be estimated. The MLE coherence estimator has been found to be equivalent to a MAP Bayesian estimator for coherence assuming uniform prior distribution (Wilkinson 1997).

4.4 Scene Topographic Reconstruction

In the Bayesian estimation framework the topographic reconstruction problem is parameterized as (Wilkinson 2000),

$$P(\theta|V_1, \dots, V_N) = a \cdot P(\theta) \cdot P(V_1, \dots, V_N|\theta) \quad (4.4)$$

where the parameter vector θ is the angle of arrival of all pixels in the SAR image, a is a constant and, V_1, \dots, V_N are the vectors representing the N complex SAR images. Assuming

that all images are accurately focused and correctly registered, each pixel data point in a given SAR image can be regarded as independent of each other. Under this assumption Equation 4.4 can be written as a product (Wilkinson 2000),

$$P(\theta|V_1, \dots, V_N) = \prod_{i=1}^M P(\theta_i|V_1(i), \dots, V_N(i)) \quad (4.5)$$

$$= \prod_{i=1}^M a_i \cdot P(\theta_i) \cdot P(V_1(i), \dots, V_N(i)|\theta_i) \quad (4.6)$$

$$= a \cdot \prod_{i=1}^M P(\theta_i) \cdot P(V_1(i), \dots, V_N(i)|\theta_i) \quad (4.7)$$

where M , is the number of pixels in each SAR image and a is a constant. The statistical independence implies that the angle of arrival parameter can be estimated on a pixel by pixel basis. Therefore, the topography of a scene can be reconstructed by calculating the position of each point in the image.

4.5 Point Position Estimation with Single Pixel Data set

4.5.1 Method Description

In the Bayesian inference approach (proposed by Dr. Wilkinson, Section 2.4) to estimate the position of a point (corresponding to a pixel in SAR image) with the angle of arrival parameter θ can be stated as ,

$$P(\theta|V) = a \cdot P(\theta) \cdot P(V|\theta) \quad (4.8)$$

where single pixel data set $V = [v_1(i), \dots, v_N(i)]$, consists of i^{th} pixel from each SAR image. The pixels comprising a single pixel data set are depicted in Figure 4.2.

The likelihood probability distribution $P(V|\theta)$ is a joint complex circular Gaussian distribution. It represents the probability of obtaining a particular set of data measurements V given a value of parameter θ . It is defined as,

$$P(V|\theta) = \frac{1}{\pi^N |K(\theta)|} \exp\left(-V^\dagger K^{-1}(\theta)V\right) \quad (4.9)$$

The position (and height) estimate of a point is based on the posterior distribution $P(\theta|V)$ and it is obtained through the following steps:

1. Define the prior distribution.
2. Calculate the likelihood distribution.
3. Combine the likelihood and prior distribution using Equation 4.8 to obtain posterior distribution and normalize it.

This process of obtaining the posterior distribution for a particular ground point is now described with an example of a three-antenna InSAR system.

The position and thus height of a point at a slant range R is to be inferred from the available single pixel dataset of three measurements from the three antennas. The true angle of arrival is to be estimated from a range of ambiguous angles of arrival as shown by dotted lines in Figure 4.3. The prior distribution $P(\theta)$ is defined over a limited range of angles as determined by imaging geometry and angular ambiguities. It is assumed to be a uniform distribution over a finite interval in absence of specific prior terrain information. The probability (i.e. likelihood probability) of obtaining the measured data given an angle of arrival, is calculated using Equation 4.9 with $N = 3$, where V is the column vector containing the three complex

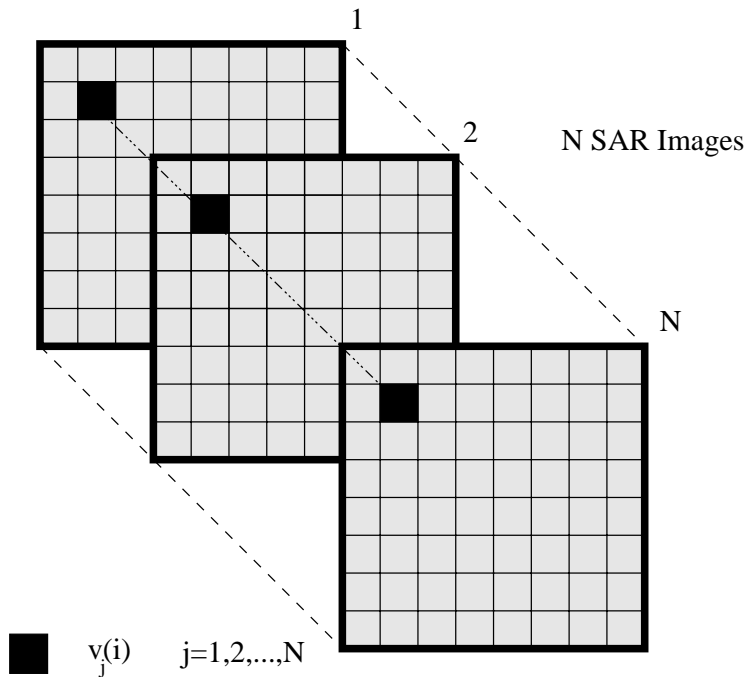


Figure 4.2: Pixel data set used for estimating the location of a point.

pixel data measurements,

$$V = \begin{bmatrix} v_1 \\ v_2 \\ v_3 \end{bmatrix}$$

v_1, v_2 and v_3 are the data measured from antenna one, two and three respectively. The complex covariance matrix K of the likelihood distribution takes the following form,

$$K = \begin{bmatrix} E \{ |V_1|^2 \} & E \{ V_1 V_2^* \} & E \{ V_1 V_3^* \} \\ E \{ V_2 V_1^* \} & E \{ |V_2|^2 \} & E \{ V_2 V_3^* \} \\ E \{ V_3 V_1^* \} & E \{ V_3 V_2^* \} & E \{ |V_3|^2 \} \end{bmatrix}$$

The variance terms in the matrix are proportional to the received signal power and are estimated using a simple averaging estimator with M pixels (similar to one used to estimate variance in the coherence estimator, Equation 4.3). These M pixel samples used in the estimates are drawn from a window size of 5×5 pixels ($M = 25$) centered about the point in the image for which the coherence value is to be estimated.

$$\begin{aligned} \sigma_{V_1}^2 &= E \{ |V_1|^2 \} = \frac{1}{M} \sum_{n=1}^M |v_1(n)|^2 \\ \sigma_{V_2}^2 &= E \{ |V_2|^2 \} = \frac{1}{M} \sum_{n=1}^M |v_2(n)|^2 \\ \sigma_{V_3}^2 &= E \{ |V_3|^2 \} = \frac{1}{M} \sum_{n=1}^M |v_3(n)|^2 \end{aligned} \tag{4.10}$$

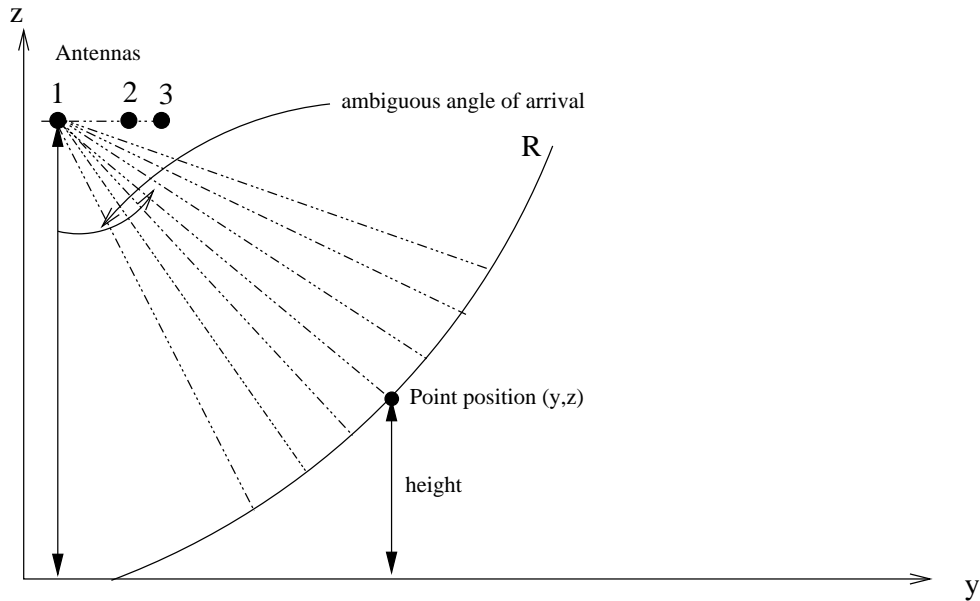


Figure 4.3: Angle of arrival geometry

The covariance elements in the matrix are expanded as per Equation 3.10. With these expansions and substitutions the covariance matrix is expressed as follows,

$$K = \begin{bmatrix} \sigma_{V_1}^2 & |\gamma_{12}| \left(\sqrt{\sigma_{V_1}^2 \cdot \sigma_{V_2}^2} \right) e^{-j\psi_{12}} & |\gamma_{13}| \left(\sqrt{\sigma_{V_1}^2 \cdot \sigma_{V_3}^2} \right) e^{-j\psi_{13}} \\ |\gamma_{12}| \left(\sqrt{\sigma_{V_1}^2 \cdot \sigma_{V_2}^2} \right) e^{+j\psi_{12}} & \sigma_{V_2}^2 & |\gamma_{23}| \left(\sqrt{\sigma_{V_2}^2 \cdot \sigma_{V_3}^2} \right) e^{-j\psi_{23}} \\ |\gamma_{13}| \left(\sqrt{\sigma_{V_1}^2 \cdot \sigma_{V_3}^2} \right) e^{+j\psi_{13}} & |\gamma_{23}| \left(\sqrt{\sigma_{V_2}^2 \cdot \sigma_{V_3}^2} \right) e^{+j\psi_{23}} & \sigma_{V_3}^2 \end{bmatrix}$$

The coherence magnitude values are obtained with the MLE coherence estimator (using a 5x5 window). The phase component of the covariance elements depends on the angle of arrival (Wilkinson 2000) and is defined as,

$$\psi_{ij} = \psi_i - \psi_j \quad (4.11)$$

where ψ_i and ψ_j is the phase of the received signals at the respective antennas. This phase is given by,

$$\psi = W \left(-\frac{2\pi(R_{tx} + R_{rx})}{\lambda} \right) \quad (4.12)$$

where R_{tx} is the distance from transmitting antenna to the target, R_{rx} is the distance from target to the receiving antenna and λ is the radar wavelength. These phases are calculated for each antenna from the geometry shown in Figure 4.4 as defined by antenna positions, angle of arrival θ , and the slant range R . The covariance matrix is calculated as a function of angle of arrival to obtain the likelihood probability using Equation 4.9. In this manner, the likelihood probability distribution is formed by calculating these probabilities over a range of angle of arrivals. The posterior distribution is obtained by multiplying the prior distribution with the likelihood distribution and normalizing it with the constant a given by,

$$a = \int P(\theta) \cdot P(V|\theta) \cdot d\theta \quad (4.13)$$

4.5.2 Application

Consider a three-antenna airborne InSAR system with imaging geometry and SAR parameters similar to the JPL's AIRSAR (Zebker et al. 1992) airborne system. The three antennas are arranged in a straight vertical line with the second antenna placed close to the third antenna to achieve a short vertical baseline. This is a single-pass system with one transmitting antenna (antenna 1 is the reference antenna). An inclined surface with an elevation angle of 10 degrees represented by a DEM is chosen as the earth surface model for simulation. The simulation geometry is depicted in Figure 4.5. A ground point position and height is estimated using the

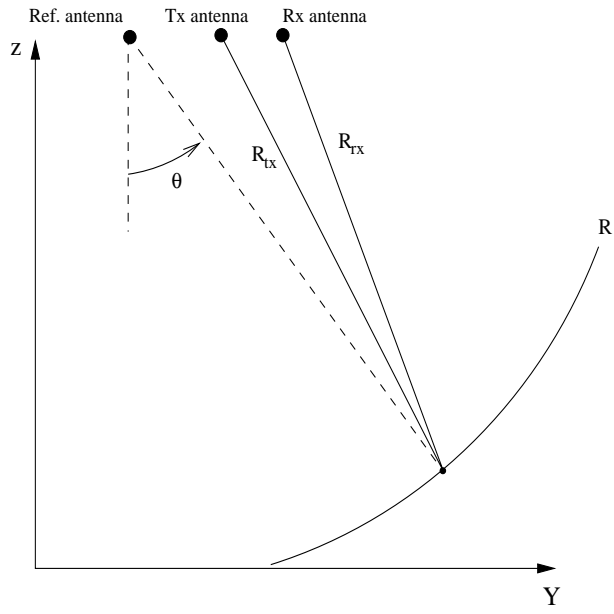


Figure 4.4: Antenna and slant range geometry.

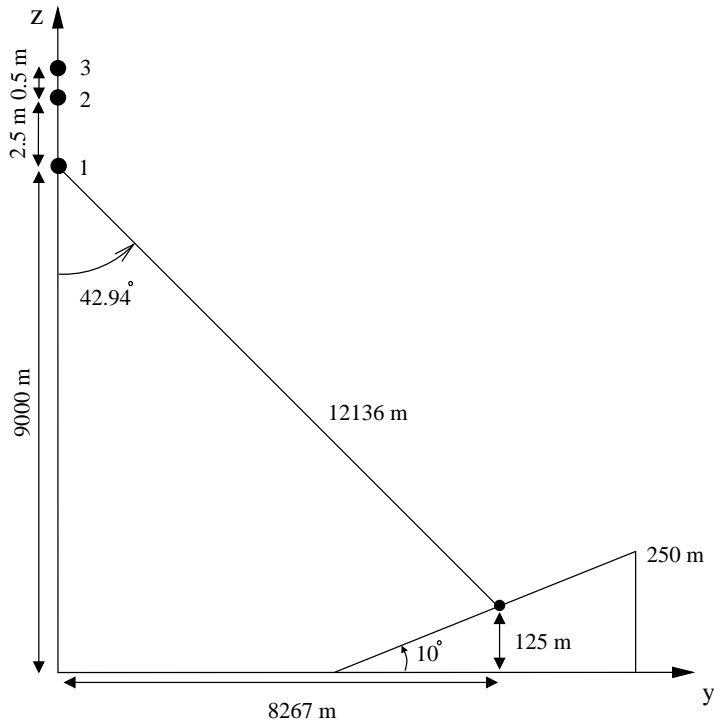


Figure 4.5: System and ground point geometry.

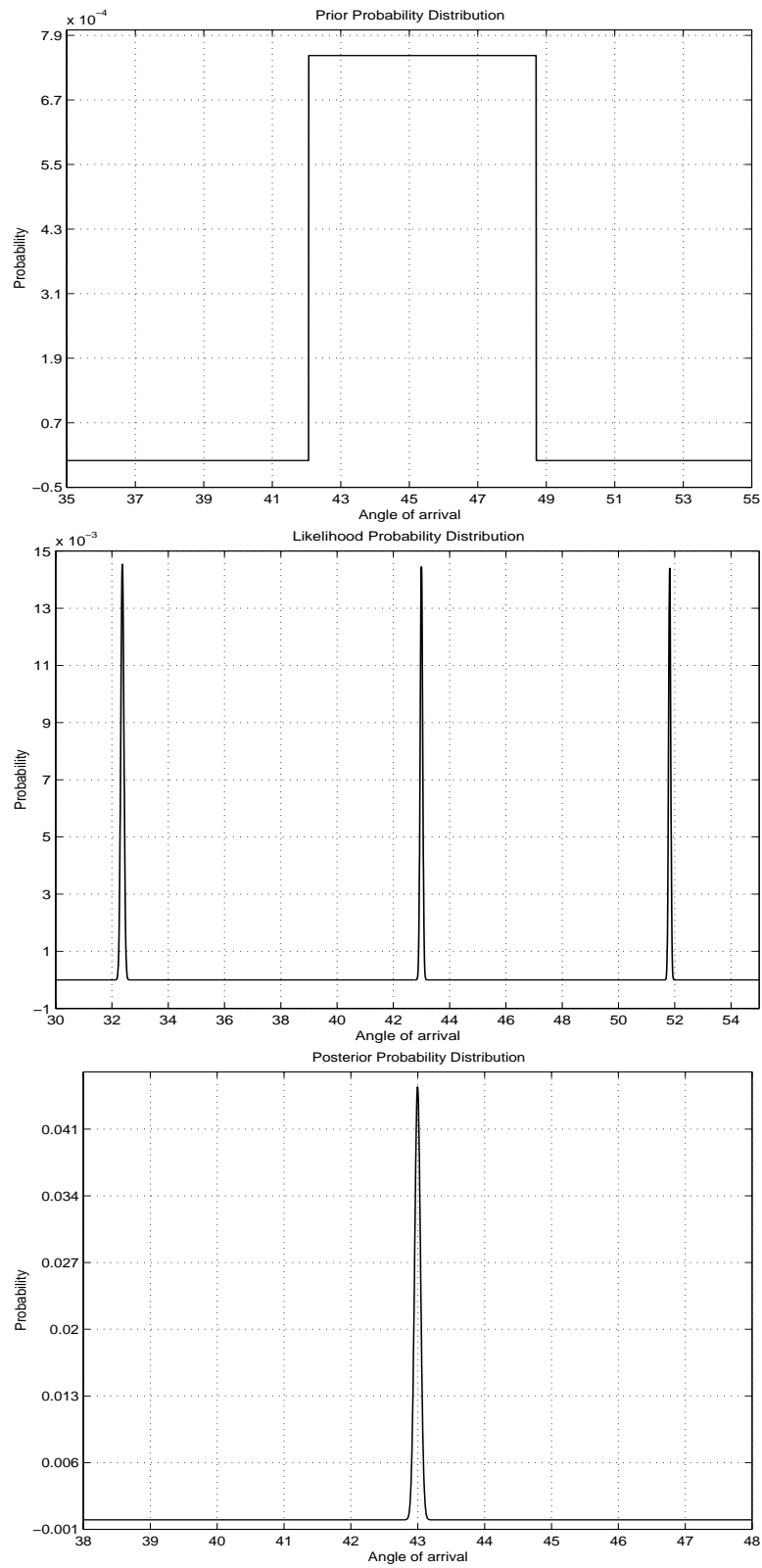


Figure 4.6: Prior, Likelihood and Posterior probability distributions.

single pixel data set method described. Table 4.1 lists the relevant SAR system and ground point parameters. A uniform prior distribution for angle of arrival corresponding to the height interval of $[0, 1000]$ m is used. The respective prior, likelihood and posterior distributions obtained are shown in Figure 4.6. As expected the MAP of the posterior distribution obtained is centered close to the true angle of arrival of 42.94 degrees corresponding to ground point height of 125m. A detailed analysis of the likelihood and posterior distributions in terms of ambiguities and estimate accuracy is presented in next chapter.

4.6 Point Position Estimation with Multiple Pixel Data set

4.6.1 Method Description

Incorporating more data into the estimation process increases the accuracy of the point position estimate obtained from the resulting posterior distribution. In this section, a method using multiple pixel data set in point position estimation using an approach proposed by Dr. Wilkinson is described. The multiple pixel data set consists of pixels in the neighbourhood of the pixel for which the position is being estimated.

Figure 4.7 shows pixels used in the multiple pixel data set obtained from N SAR images. The data set V consists of $2L + 1$ sets (L^2 , if data points in azimuth direction are also included) of pixel data points in the slant range direction centered around the pixel of interest i ,

InSAR System Parameters	
Baseline 1 & 3 [m]	3.0
Baseline 1 & 2 [m]	2.5
Baseline 2 & 3 [m]	0.5
Radar Frequency [GHz]	5.3
Radar Bandwidth [MHz]	20.0
Reference Antenna Altitude [m]	9000
Ground Point Parameters	
Ground Point Height [m]	125
Slant Range Distance [m]	12136
Angle of arrival [deg]	42.94

Table 4.1: System and ground point parameters.

$$V = \begin{bmatrix} v_1(i-L) & \cdots & v_1(i) & \cdots & v_1(i+L) \\ \vdots & & \vdots & & \vdots \\ v_N(i-L) & \cdots & v_N(i) & \cdots & v_N(i+L) \end{bmatrix} \quad (4.14)$$

where L is the number of data points used on either side of the i^{th} point. Pixel data points in azimuth direction are not used as that would require additional parameters to be estimated, thereby increasing the dimensionality of the posterior and resulting in unrealistic computational times (e.g. in MATLAB prototyping environment). Hence the method implemented only includes data pixels in the slant range direction.

These data sets are assumed to be statistically independent of each other and therefore the likelihood distribution is expressed as a product (Wilkinson 2000),

$$P(V|\theta_i) = \prod_{k=i-L}^{i+L} P(V(k)|\theta_k(\theta_i)) \quad (4.15)$$

where θ_k is the angle of arrival for the k^{th} point, θ_i is the angle of arrival of the point of interest i and $V(k)$ represents the dataset of the k^{th} point. It is assumed that all points lie on a straight line of a slope angle α , with i^{th} point at the center as shown in Figure 4.8. Therefore, angle

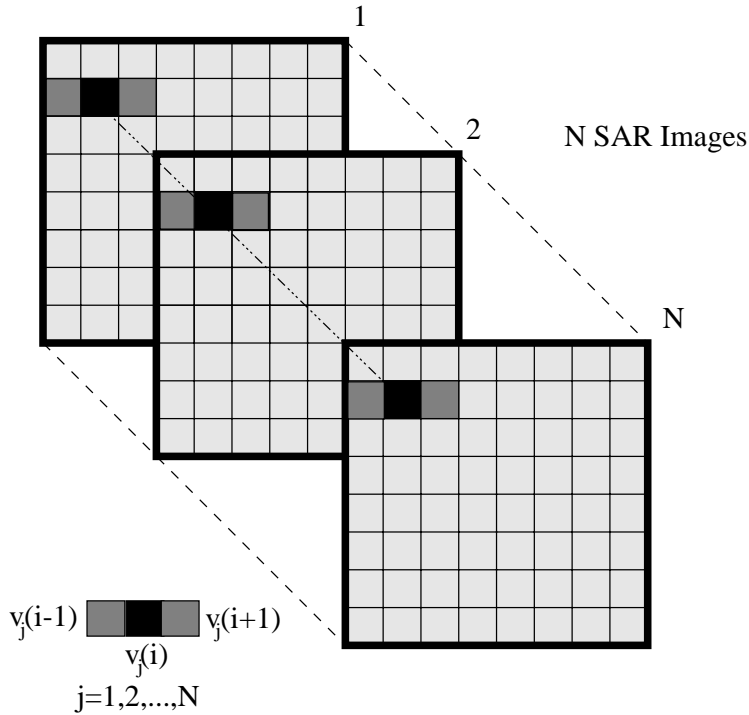


Figure 4.7: Multiple pixel data set ($L = 1$) for estimating the position of the point.

of arrival θ_k for the k^{th} point is constrained by the local slope of the line and the value of θ_i . The straight line modeling of the local surface is an approximation to the real surface, with the local slope parameter offering some adaptability. Therefore, the local slope angle is also included as a parameter that has to be estimated. With the local slope as another parameter, the estimation problem can be re-parametrized and stated as (Wilkinson 2000),

$$P(\theta_i, \alpha | V) = a \cdot P(\theta_i, \alpha) \cdot P(V | \theta_i, \alpha)$$

where V is the multiple pixel data set as specified in Equation 4.14, a is the normalization constant, and $P(V | \theta_i, \alpha)$ is the joint likelihood distribution given by,

$$P(V | \theta_i, \alpha) = \prod_{k=i-L}^{i+L} P(V(k) | \theta_k, \alpha)$$

Obtaining the likelihood distribution involves calculating the likelihood distribution $P(V(k) | \theta_k, \alpha)$ for each point individually. The θ_k for each point is calculated by finding the intersection between the line and the slant range arc R_k as shown in Figure 4.9. Then the covariance matrix is computed in a similar way as described in the previous section over a range of θ and α values. The resulting $2L + 1$, two dimensional distributions are multiplied to obtain the joint likelihood

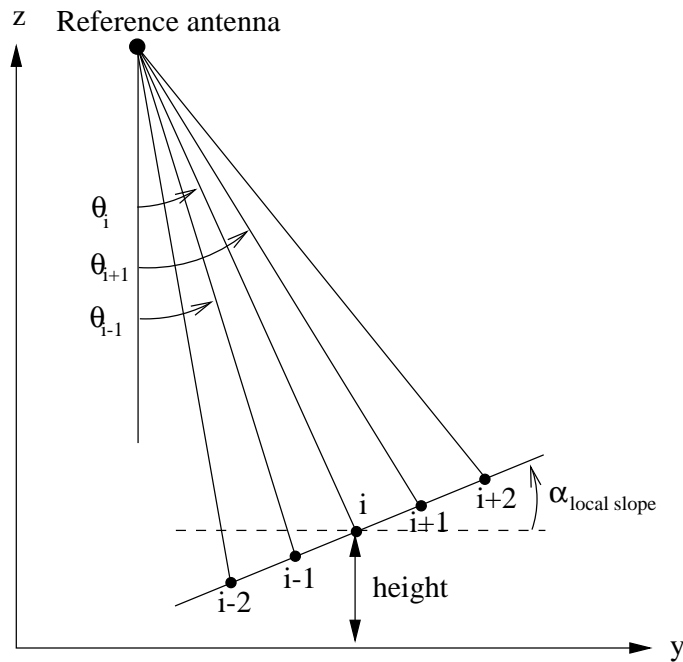


Figure 4.8: A straight line through predicted position of all points.

distribution for the complete data set. Thereafter, the joint posterior distribution for the two parameters is calculated as a product of a suitable prior distribution with the joint likelihood distribution. Estimates of the angle of arrival and local slope are obtained from the MAP points of the respective marginalised posterior distributions. In next chapter, a comparison of the accuracy of the estimated obtained with the multiple and single pixel estimation methods is presented.

4.6.2 Application

We use the same three-antenna airborne InSAR system as described in Table 4.1 for estimation of position of the point using multiple pixel data set method. Three adjacent pixels points ($L = 1$) in the slant range direction are used in multiple pixel data set. The signal returns from these points are simulated and the resulting multiple pixel data set is used in the estimation process to obtain the likelihood and posterior probability distributions for the middle point. As the local slope and angle of arrival are estimated jointly the resulting probability distributions are two dimensional. Figure 4.10 shows the marginalised probability distributions obtained from the joint probability distributions of the two parameters. The marginalised posterior distribution are calculated through the following equations,

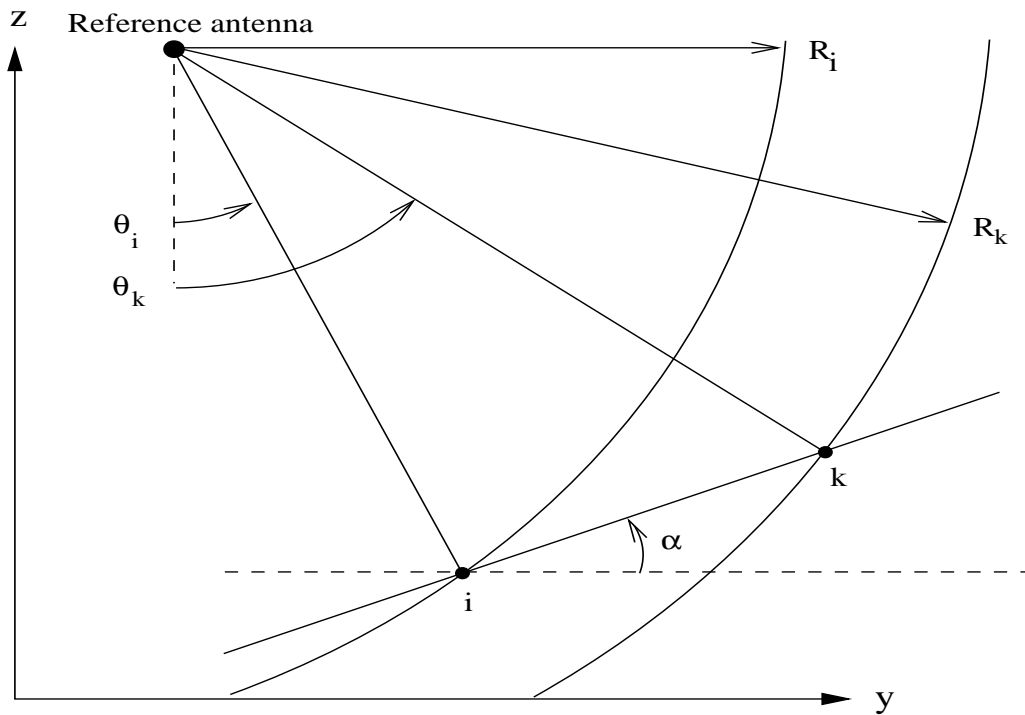


Figure 4.9: Intersection of a k^{th} slant range arc with the line.

$$P(\theta|V) = \int P(\theta, \alpha|V) \cdot d\alpha \quad (4.16)$$

$$P(\alpha|V) = \int P(\theta, \alpha|V) \cdot d\theta \quad (4.17)$$

From the plot of the posterior distribution of the local slope angle, it is observed that MAP point is at 8.5 degrees close to the true value of 0 degrees. The MAP angle of arrival posterior distribution gives the height estimate as 128.67m close to the true height 125m.

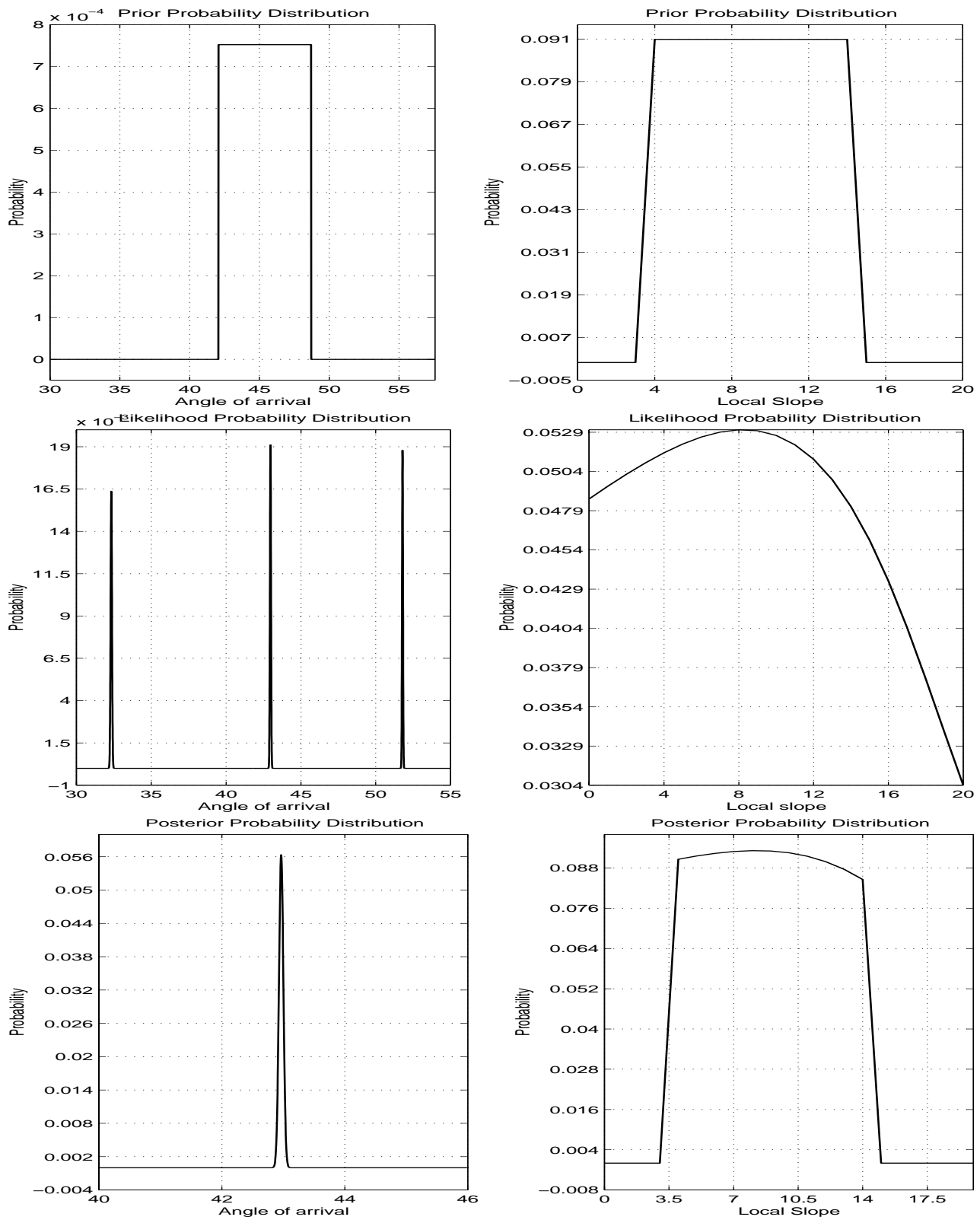


Figure 4.10: Marginalised probability distributions for angle of arrival and local slope angle.

Chapter 5

Analysis of Results

5.1 Introduction

The likelihood and posterior probability distributions represent the surface topographic information obtained with the Bayesian estimation methods implemented. Thus an analysis of the likelihood and posterior distributions is crucial to understand the information conveyed by these distributions. In this context, the ambiguities in the likelihood distribution for all antenna combinations is analysed in detail. In addition, the accuracy of the estimates obtained from the posterior distribution is analysed and compared for the two Bayesian estimation methods implemented, highlighting the higher accuracy of the method utilising multiple pixel data set. Finally, topographic reconstruction with the Bayesian estimation method is demonstrated by reconstructing the terrain height of a single range line.

5.2 Simulated SAR Data

A single-pass three-antenna airborne InSAR system similar to JPL's AIRSAR system together with an inclined plane surface represented a DEM is simulated in the model-based simulator developed in chapter 3. Figure 5.1 depicts the simulation geometry showing the asymmetrical antenna configuration with the three antennas arranged in a vertical plane. Table 5.1 lists the parameters of the InSAR system and surface topography used in the simulation. The simulated SAR data is used in the analysis of likelihood and posterior distributions in the following sections.

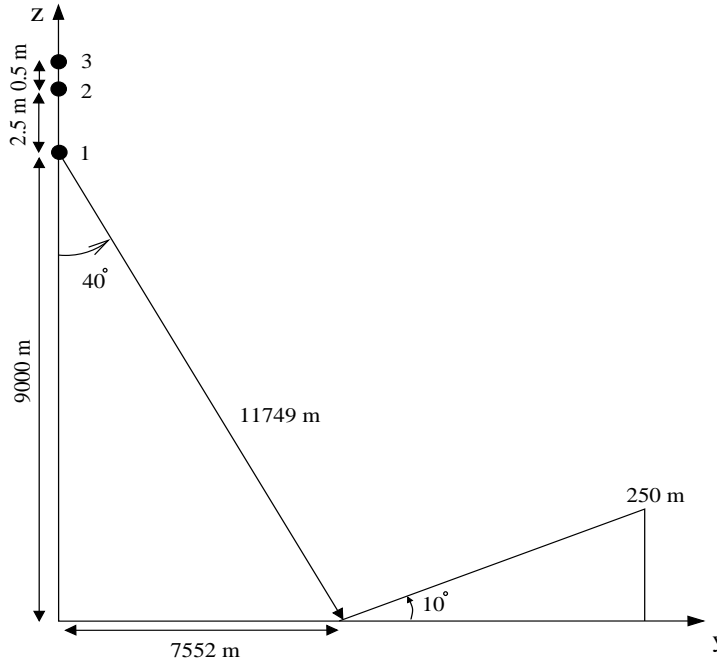


Figure 5.1: Simulation geometry of a inclined plane DEM with the three-antenna InSAR system.

System Parameter	Value
Antenna 1 and 3 separation [m]	3.0
Antenna 1 and 2 separation [m]	2.5
Antenna 2 and 3 separation [m]	0.5
Reference Antenna Height [m]	9000
Imaging Radar Frequency [GHz]	5.3
Imaging Radar Bandwidth [MHz]	20.0
Scene Parameter	Value
Maximum height [m]	250
Minimum height [m]	0
Slant range swath width [m]	800
Slant range spacing [m]	12.5
Azimuth spacing [m]	12.5

Table 5.1: Three antenna InSAR system and scene parameters.

5.3 Ambiguity Analysis

The asymmetrical arrangement of the antennas gives rise to three different ambiguities in the measured data. These ambiguities appear in form of repeating peaks in the likelihood and posterior distributions of angle of arrival parameter. The likelihood distribution of the angle of arrival formed with each of the three antenna pairs has a different ambiguity. To show these ambiguities, the likelihood distributions for all three antenna pair combinations are calculated using a single pixel data set from the simulated data. Figure 5.2 (a) shows the ambiguity in the likelihood distribution of angle of arrival, for data from antenna pair (1,3). Similarly, Figure 5.2 (b) and (c) depict the likelihood distributions of angle of arrival for data from antenna pairs (1,2) and (2,3) respectively.

As expected it was found that the ambiguities are most closely spaced in the likelihood distribution for the longest baseline of antenna pair (1,3) and the likelihood distribution for antenna pair (2,3) with the shortest baseline has the least ambiguity of the three antenna pairs. The angular ambiguities and related displacement, height, and horizontal ambiguities corresponding to the three baselines (calculated using Equations 2.15, and 2.18-2.19) are listed in Table 5.2.

In the Bayesian framework, the likelihood distribution with all three antenna data represents the optimal fusion of the three likelihood distributions with different ambiguities. This combined likelihood distribution with reduced ambiguity is shown in Figure 5.3. The angular ambiguity $\Delta\theta_{amb}$ of the combined likelihood distribution for the three-antenna system is given by Equation 2.21 as,

$$\Delta\theta_{amb} = p \cdot \Delta\theta_{amb}^{13} \quad (5.1)$$

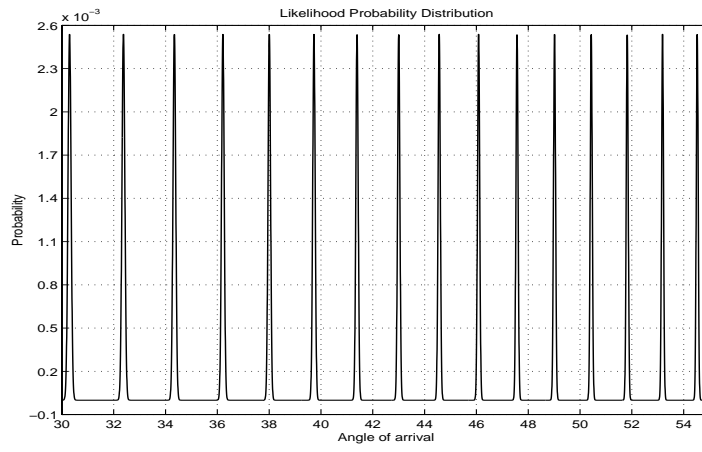
where $\Delta\theta_{amb}^{13}$ is the angular ambiguity of the two-antenna system (with antenna 1 and 3) and p is the ambiguity enhancement factor of the system, defined by Equation 2.20 as,

$$p = \frac{b_{13}}{b_{23}} \quad (5.2)$$

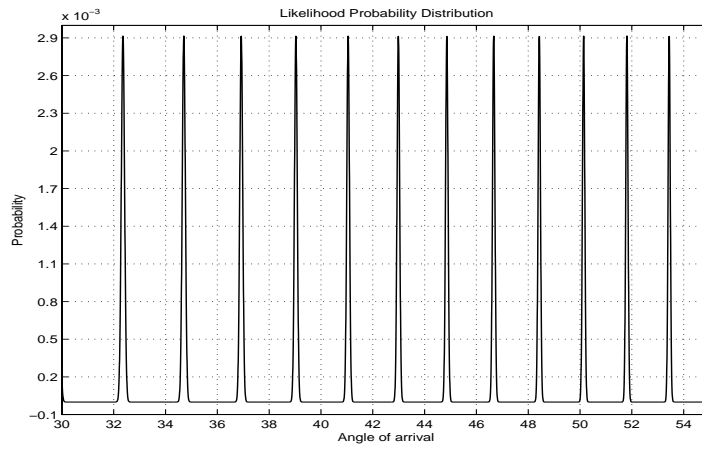
Using Equations 5.1, 5.2 and baseline parameters from Table 5.1 the system angular ambiguity

Vertical baseline [m]	$b_{13} = 3.0$	$b_{12} = 2.5$	$b_{23} = 0.5$
Angular ambiguity [deg]	$\Delta\theta_{amb}^{13} = 1.458$	$\Delta\theta_{amb}^{12} = 1.750$	$\Delta\theta_{amb}^{23} = 8.750$
Displacement ambiguity [m]	$\Delta l_{amb}^{13} = 308.2$	$\Delta l_{amb}^{12} = 370.1$	$\Delta l_{amb}^{23} = 1851.9$
Height ambiguity [m]	$\Delta h_{amb}^{13} = 206.8$	$\Delta h_{amb}^{12} = 248.3$	$\Delta h_{amb}^{23} = 1242.2$
Horizontal ambiguity [m]	$\Delta y_{amb}^{13} = 228.6$	$\Delta y_{amb}^{12} = 274.5$	$\Delta y_{amb}^{23} = 1373.4$

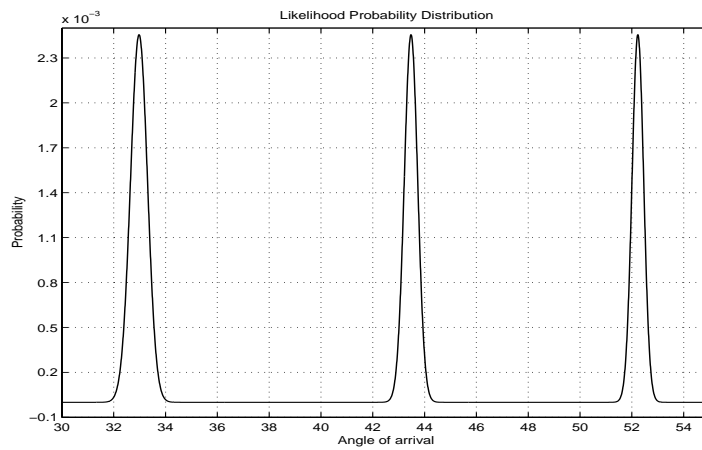
Table 5.2: Ambiguities corresponding to the 3 vertical baselines in the three-antenna system.



(a) Antenna pair (1,3)



(b) Antenna pair (1,2)



(c) Antenna pair (2,3)

Figure 5.2: Likelihood PDF of angle of arrival using various antenna pairs.

$\Delta\theta_{amb}$ is calculated as,

$$\Delta\theta_{amb} = 8.748 \text{ degrees}$$

The corresponding displacement ambiguity Δl_{amb} , height (vertical) ambiguity Δh_{amb} , and horizontal ambiguity Δy_{amb} for the three-antenna system as given by Equations 2.18, 2.17, and 2.19 respectively are as follows:

$$\Delta l_{amb} = 1852 \text{ metres}$$

$$\Delta h_{amb} = 1242 \text{ metres}$$

$$\Delta y_{amb} = 1373 \text{ metres}$$

It should be noted that the height ambiguity Δh_{amb} determines the range of surface heights (in this case 1242 m) that can be estimated unambiguously from the measured data.

The angle of arrival prior, a uniform distribution corresponding to the height interval of length Δh_{amb} , is applied to the likelihood distribution shown in Figure 5.3 to obtain the posterior distribution Figure 5.4. The posterior in Figure 5.4(a) plotted on a linear scale exhibits only one peak. The maximum of this peak i.e.MAP point is the angle of arrival estimate and is used for calculating the height of the point. Plotting the posterior on a log scale as shown in Figure 5.4(b) reveals several suppressed ambiguities around the main peak. It is found

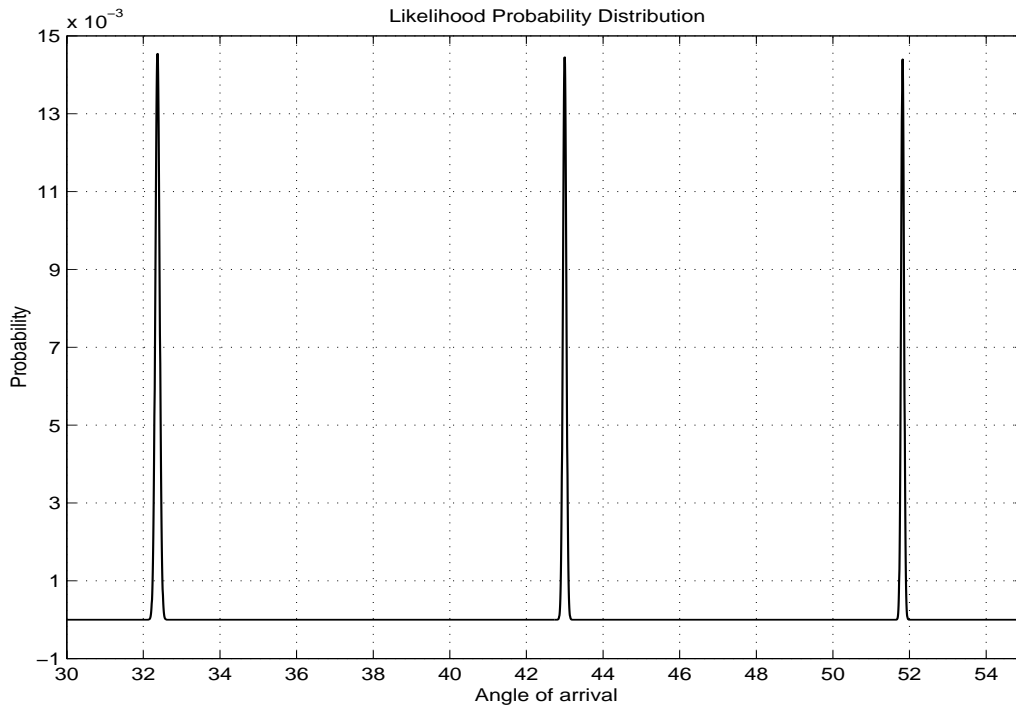


Figure 5.3: Likelihood PDF of angle of arrival using all three antenna pair data.

that these suppressed ambiguities are insignificant for high coherence values between antenna measurements. However, these ambiguities become significant for low correlation values and cannot be ignored.

5.4 Accuracy Analysis

The uncertainty in the estimated value of angle of arrival is a measure of the accuracy of estimates obtained with the Bayesian estimation methods. This uncertainty in the angular estimate is a function of correlation between the measured data. This is shown by the phase standard deviation values (obtained from graph in Rodriguez and Martin 1992) in Table 5.3 corresponding to the three (theoretical) coherence values for data from the three antenna pairs.

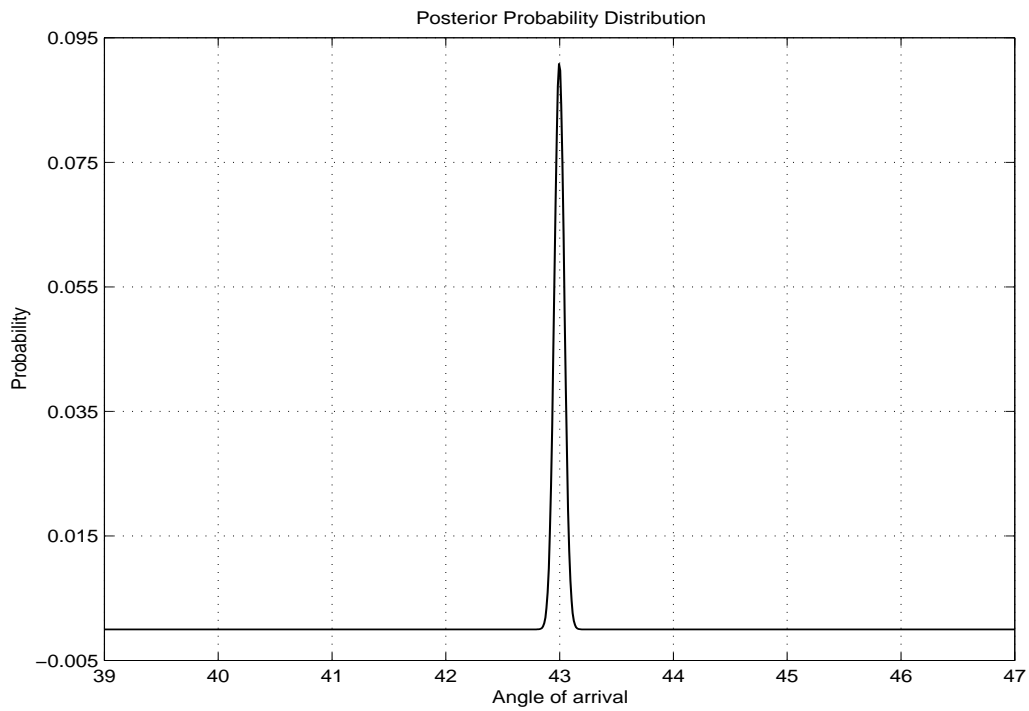
In addition to coherence, the uncertainty in estimates also depends on the number of data points used in the estimation process. In the Bayesian approach, the uncertainty in the angle of arrival estimate is directly proportional to the spread of the posterior distribution. Thus the standard deviation of the posterior probability distribution is formulated as a quantitative measure of the estimate accuracy. The standard deviation of the angle of arrival is calculated from the posterior probability distribution.

In order to analyse the uncertainty of estimates obtained with the Bayesian method as a function of number of data points used in the estimation, we consider three separate cases of point position estimation. In the first case, the Bayesian estimation method uses a single pixel data set. The angle of arrival posterior obtained after applying the estimation method is plotted in Figure 5.5. In next case, three pixel data sets are used in the Bayesian estimation process to obtain the posterior shown in Figure 5.6. In the third case, five pixel datasets are used in the estimation process. The posterior distribution obtained is shown in Figure 5.7. The vertical dotted lines in each of the posterior plots mark one standard deviation from the peak.

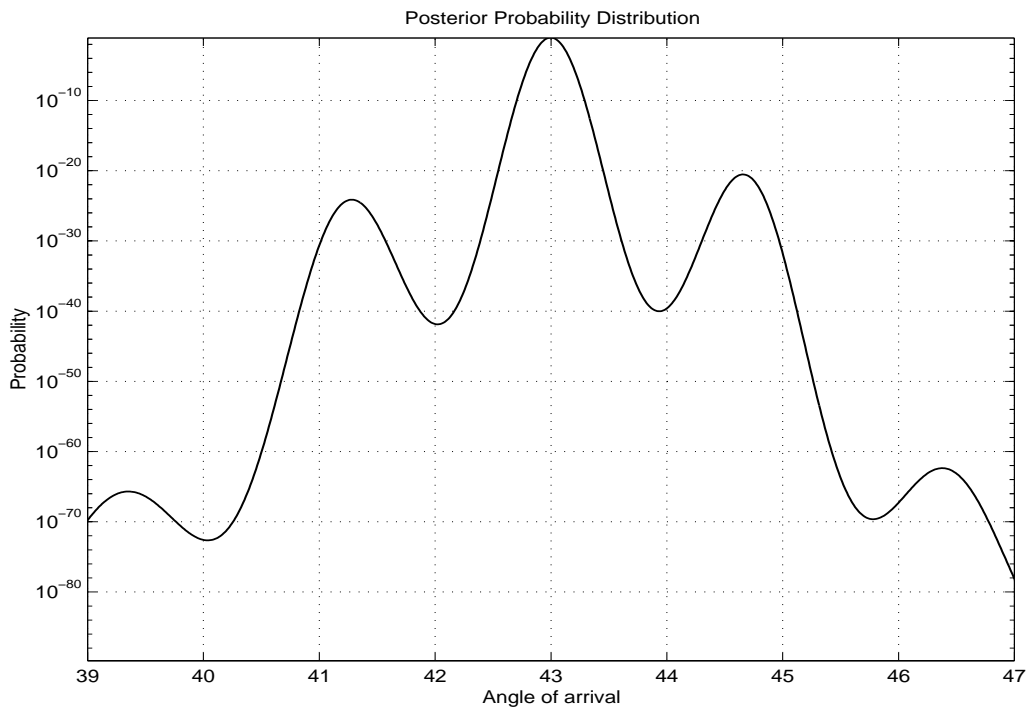
The angle of arrival standard deviations for each case as measured from the posterior plots are listed in Table 5.4. In addition, the displacement standard deviation σ_l , height standard deviation σ_h , and horizontal standard deviation σ_y are also calculated from the measured angle

Antenna pair	Baseline [m]	Coherence	Phase standard deviation [cycles]
2 and 3	0.5	0.9806	0.05512
1 and 2	2.5	0.9647	0.07126
1 and 3	3.0	0.9607	0.07445

Table 5.3: Phase standard deviation and coherence theoretically calculated values.



(a) Linear scale



(b) Log scale

Figure 5.4: Posterior PDF of angle of arrival using all three antenna data.

Number of pixels in data set	1	3	5
Angle Standard Deviation [deg]	$\sigma_\theta = 0.044$	$\sigma_\theta = 0.036$	$\sigma_\theta = 0.031$
Displacement Standard Deviation [m]	$\sigma_l = 9.31$	$\sigma_l = 7.62$	$\sigma_l = 6.63$
Height Standard Deviation [m]	$\sigma_h = 6.35$	$\sigma_h = 5.19$	$\sigma_h = 4.52$
Horizontal Standard Deviation [m]	$\sigma_y = 6.81$	$\sigma_y = 5.57$	$\sigma_y = 4.85$

Table 5.4: Angle of arrival and height standard deviations for various number of datasets.

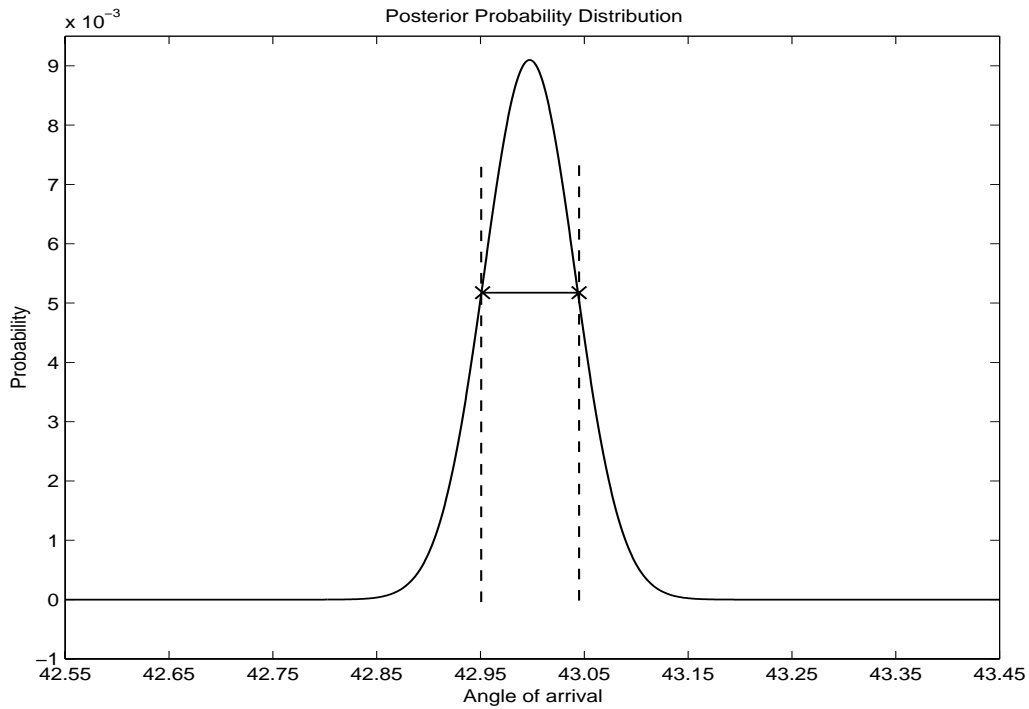


Figure 5.5: Posterior PDF with one pixel data set. The vertical dotted lines mark one standard deviation from the peak

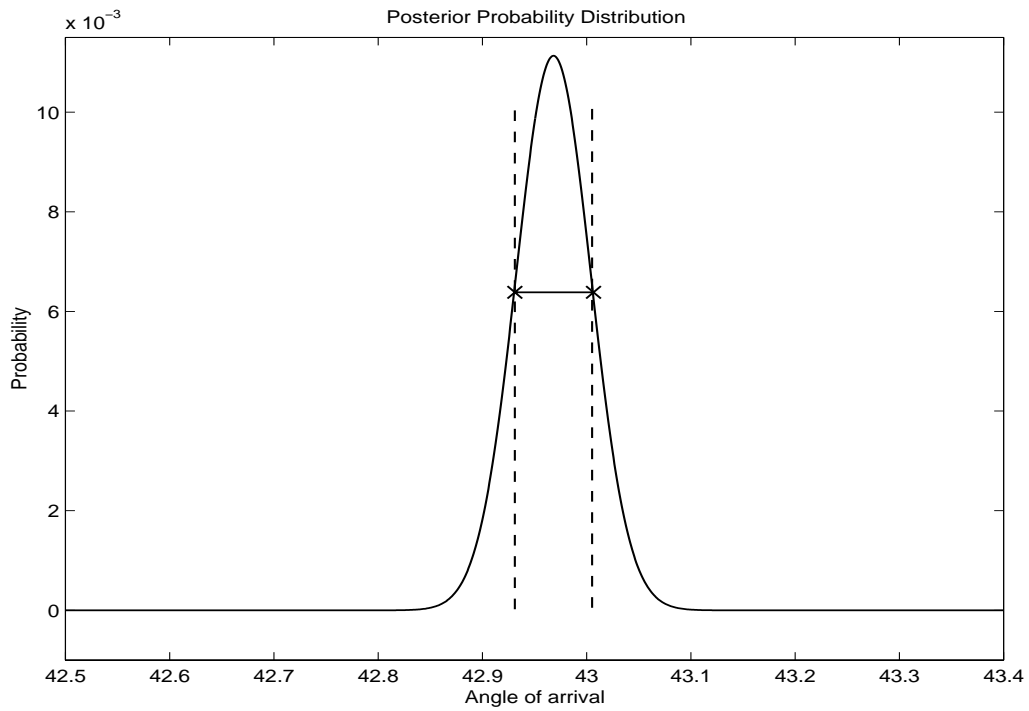


Figure 5.6: Posterior PDF with three pixel data set. The vertical dotted lines mark one standard deviation from the peak

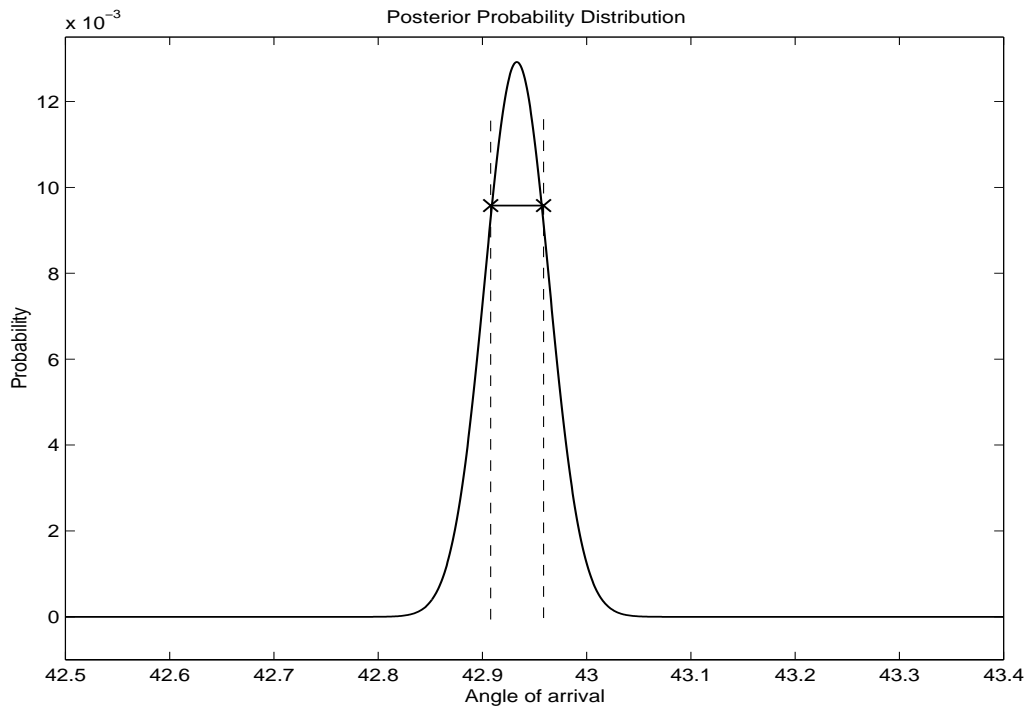


Figure 5.7: Posterior PDF with five pixel data set. The vertical dotted lines mark one standard deviation from the peak

of arrival standard deviation σ_θ using the following set of equations (are also included in the table),

$$\sigma_l = r_1 \cdot \sigma_\theta \quad (5.3)$$

$$\sigma_h = r_1 \cdot \sin(\theta) \cdot \sigma_\theta \quad (5.4)$$

$$\sigma_y = r_1 \cdot \cos(\theta) \cdot \sigma_\theta \quad (5.5)$$

From these tabulated standard deviation values and the posterior plots it is clear that the accuracy of the point position estimates increases with the number of pixel data point used in the estimation process. Thus we conclude that accuracy of the estimates obtained from the posterior distribution is a function of data coherence and number of data points used.

5.5 Terrain Reconstruction

A circular mound DEM together with the three-antenna system specified in Table 5.1 is simulated with the multiple-antenna simulator. The parameters of the circular mound DEM are listed in Table 5.5. The Bayesian estimation method using three pixel data set is applied to the simulated data to reconstruct the DEM.

A uniform prior distribution defined over the unambiguous range of angle of arrivals (corresponding to one height ambiguity Δh_{amb}) is used for each point. The coherence is estimated with the MLE using a 5x5 window, for each of the three antenna data pairs. Plots of the reconstructed height and standard deviation covering for the whole DEM are shown in Appendix B. We analyse the terrain reconstruction for a single range line from the centre of the DEM. Figure 5.8 shows a plot of the height of the centre range line from the reconstructed DEM, superimposed on the real height profile. The standard deviation of estimated height is plotted in Figure 5.9 as a function of slant range. Figures 5.10, 5.11 and 5.12 show the simulated and estimated coherence values for each of the three antenna pairs. These plots clearly show how the height standard deviation varies with the estimated coherence. It can be seen how the accuracy of the height estimate deteriorates for low coherence values in the steep region.

Mound DEM Parameter	Value
Maximum height [m]	400
Minimum height [m]	0
Slant range swath width [m]	1950
Slant range spacing [m]	12.5
Azimuth spacing [m]	12.5

Table 5.5: Mound DEM parameters.

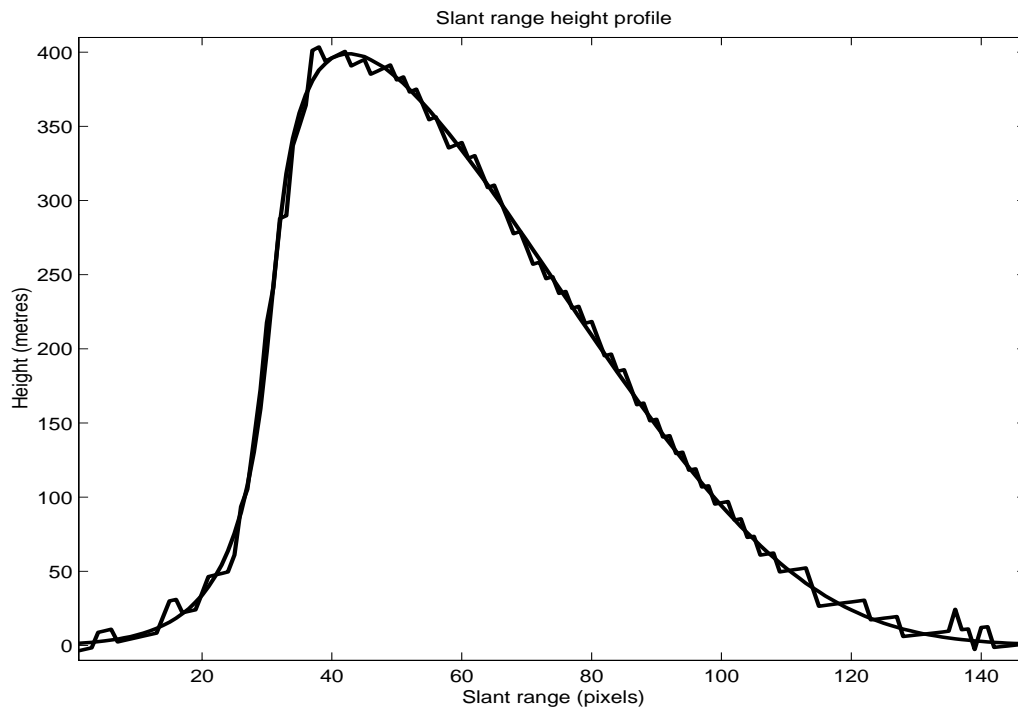


Figure 5.8: Slant range profile of estimated and real terrain height.

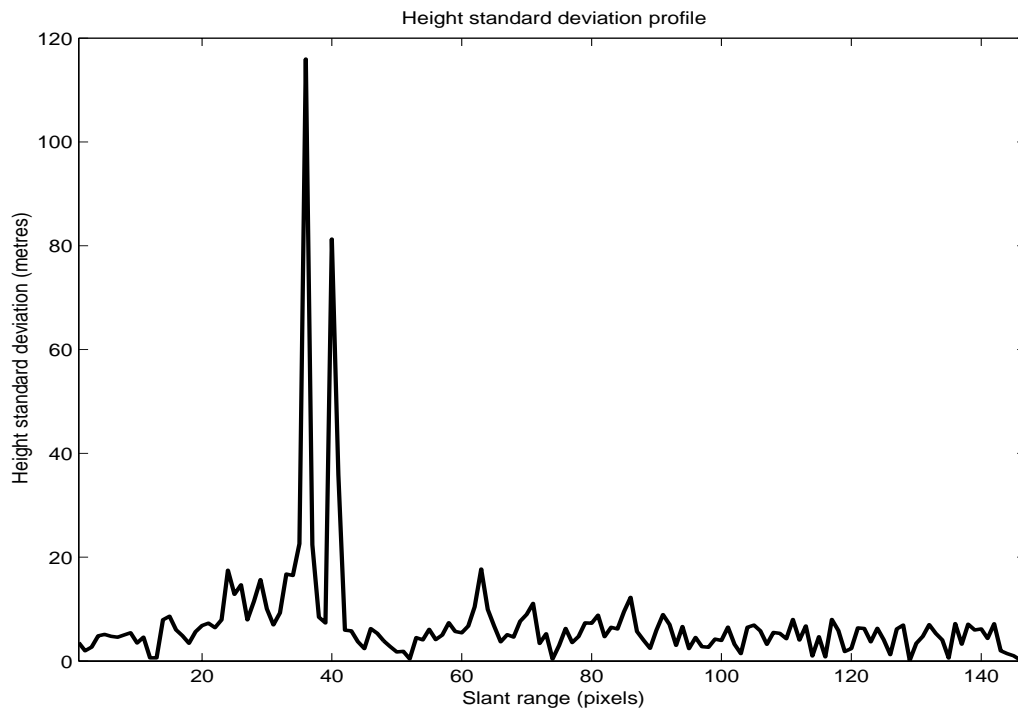


Figure 5.9: The height standard deviation of estimated height.

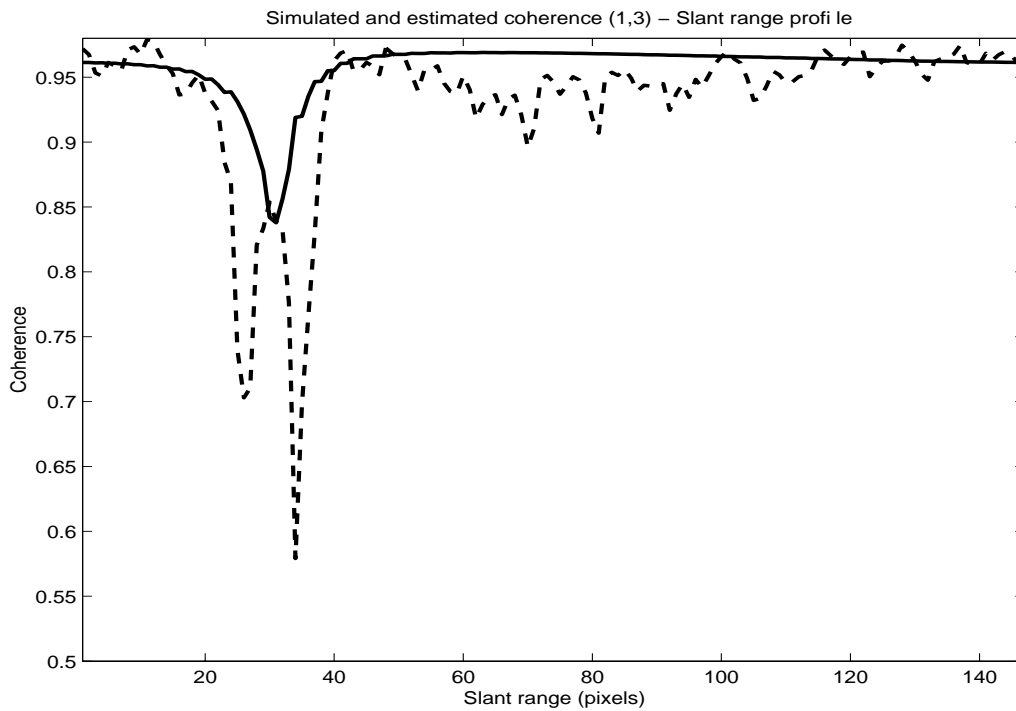


Figure 5.10: A slant range plot of the simulated and estimated (dotted line) coherence for data from antenna pair (1,3).

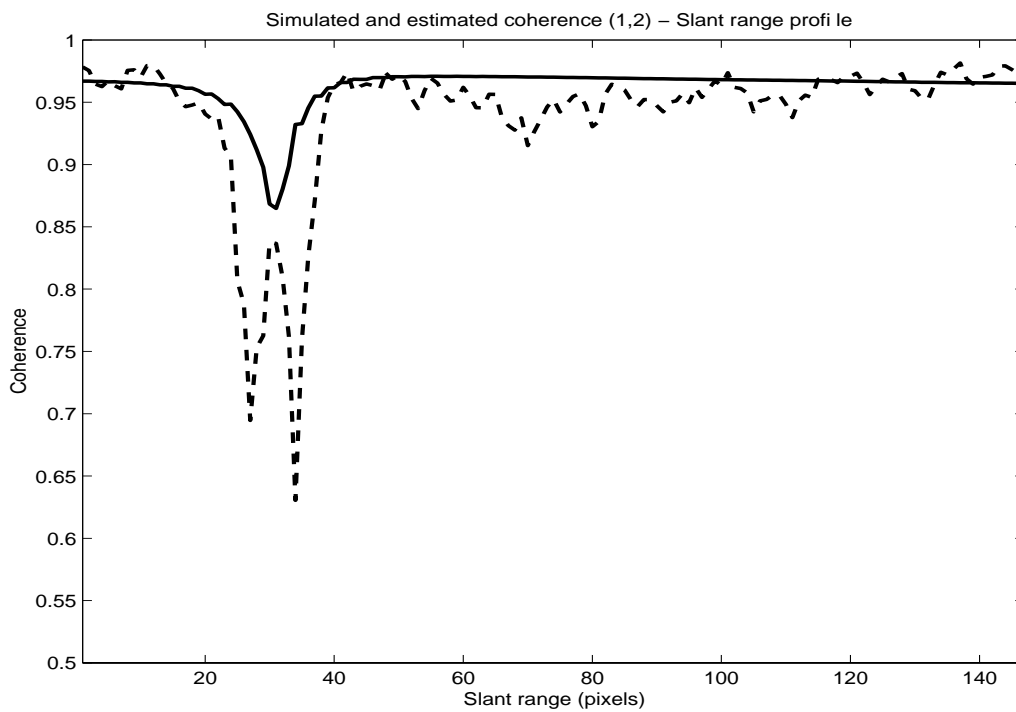


Figure 5.11: A slant range plot of the simulated and estimated (dotted line) coherence for data from antenna pair (1,2).

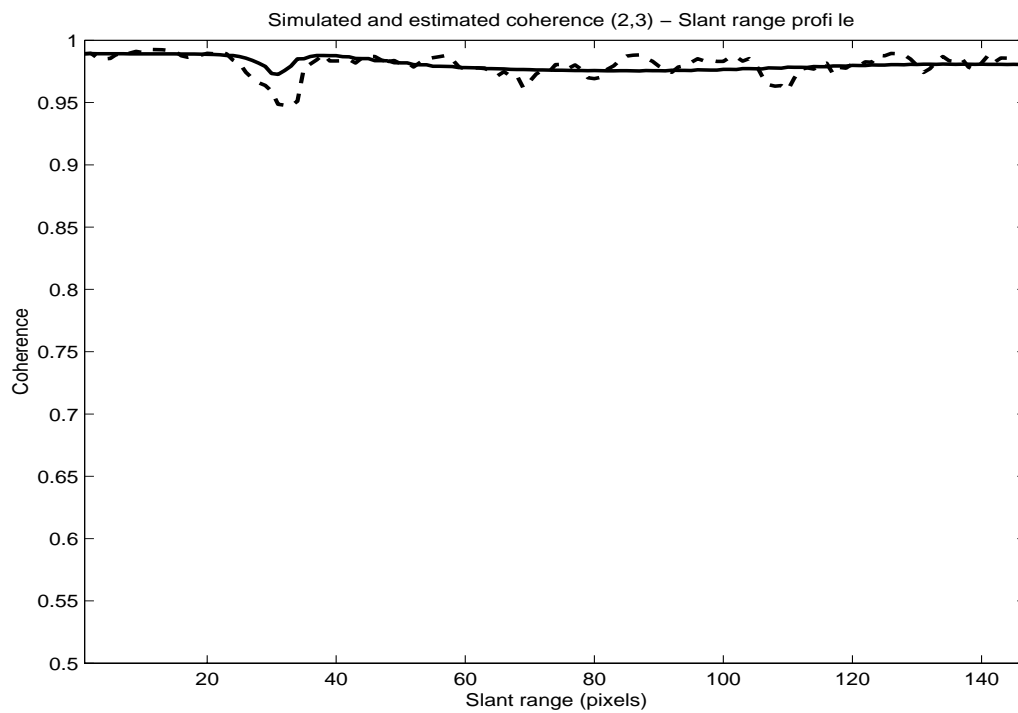


Figure 5.12: A slant range plot of the simulated and estimated (dotted line) coherence for data from antenna pair (2,3).

Chapter 6

Conclusion and Future Work

6.1 Conclusion

The following main objectives in this dissertation have been investigated:

- Description of the theory of multiple-antenna interferometry and analysis of the model-based Bayesian approach to topographic mapping with multiple-antenna interferometry proposed by Dr. Wilkinson.
- Implementation of a multiple-antenna interferometric SAR simulator to evaluate the proposed Bayesian topographic reconstruction techniques.
- Implementation and analysis of angle of arrival estimation reconstruction algorithms developed according to the Bayesian model-based approach proposed by Dr. Wilkinson.

The application of multiple-antenna interferometry to topographic mapping was explained from the basic principles of SAR interferometry. It was found that the reduction in ambiguities in multiple-antenna interferometry, compare to conventional two-antenna interferometry, was as a result of baseline diversity in a multiple-antenna configuration. Main features of improved data-noise characteristics and reduced ambiguities offered by multiple-antenna interferometry were shown to facilitate the topographic mapping process.

A model-based Bayesian approach to topographic reconstruction from multiple-antenna interferometry proposed by Dr. Wilkinson was presented. In this approach, the topographic reconstruction has been formulated as a parameter estimation problem in the Bayesian inference framework. A statistical forward model was considered, relating the surface topography, surface reflectivity, radar parameters and the system geometry to the measured SAR data. The

forward model described the SAR imaging process as a random process and defines the SAR images as collection of correlated random variables defined by a joint probability distribution.

An interferometric SAR simulator for simulating multiple-antenna SAR data based on the forward model was developed. In the theoretical simulation framework the SAR image formation process was reviewed and the definition of the forward model in terms of the joint probability distribution was presented. The joint probability distribution with its main parameter the complex covariance matrix was defined in terms of the SAR image characteristics such as coherence, interferometric phase and the received power. Implementation of the simulator involved the calculation of these statistics of the joint probability distribution from the system geometry, terrain DEM, radar parameters and the flight path. In the simulation, the Cholesky decomposition technique was implemented to sample from the joint distribution for generating the multiple-antenna SAR data.

In the approach implemented, the parameter estimation problem was stated as estimation of the surface topography, given the measured multiple-antenna SAR data. The estimation of surface topography of a scene was simplified to estimating the position (and height) of each point separately. A Bayesian estimation method was implemented to estimate the angle of arrival parameter using a single pixel data set. This method was implemented assuming a uniform prior and involved the calculation of the likelihood distribution based on the measured complex dataset and the system geometry. The resulting posterior distribution of the angle of arrival was used as the basis for estimating the position of a point. Another Bayesian estimation method as proposed by Dr. Wilkinson was also implemented that used multiple pixel data sets to achieve improved the accuracy of the point position estimates. This improved Bayesian estimation method with the second parameter of the local slope, jointly estimated with the angle of arrival parameter was also implemented. The two Bayesian methods were applied to simulated dataset from a three-antenna InSAR to estimate the position and height of a point. The methods performed within expectations, the position estimates derived from the posterior distribution were close to the true position of the point demonstrating the effectiveness of the proposed estimation methods. A improved version of the MLE estimator for estimating coherence was also reviewed and successfully implemented.

The likelihood and posterior distributions were analysed for a three-antenna airborne SAR system. Ambiguities in the likelihood distribution of angle of arrival were considered. The ambiguity in the angle of arrival likelihood distribution was used to calculate height, displacement, and horizontal ambiguities for each antenna pair. The reduced ambiguity in the likelihood distribution of the three-antenna data was described as optimal fusion of the likelihood functions

for each antenna pair. An analysis of the accuracy of the position estimates obtained from the posterior distribution was also pursued. The angle of arrival posterior distribution's standard deviation was used as a quantitative measure of the accuracy of point position estimate. The accuracy measurements included angle of arrival standard deviation and standard deviations for displacement, height and horizontal positional parameters. These standard deviation measurements proved that the method using multiple pixel data set achieves better accuracy with optimal data fusion. Finally, the multiple pixel data set Bayesian estimation method was applied to a simulated data set obtained using the three-antenna airborne system to reconstruct the DEM of a circular mound. Plots of the height standard deviation and coherence from this reconstruction process were used to demonstrate the variation of the estimate accuracy with coherence across a single range line.

6.2 Future Work

The following areas are identified for future work:

- Investigate non-parallel antenna flight path models and terrain specific backscatter models for the InSAR simulator to increase the accuracy (and realism) of the spaceborne/airborne SAR simulations.
- Investigate a practical implementation of the Bayesian approach proposed by Dr. Wilkinson for topographic reconstruction in layover regions. A Bayesian estimation approach using the layover coherence model (Wilkinson 1997, 1998, 1999) together with a model-selection scheme should be investigated for reconstruction in layover regions.
- Develop methods for infusing more specific prior information about the the surface topography in the Bayesian reconstruction method. Statistical models of earth surface that have been proposed in the literature should be investigated for this purpose.
- Investigate techniques for analysing higher multi-dimensional posterior distributions in a computationally efficient manner so that all unknown parameters in the topographic reconstruction problem can be included in the Bayesian estimation process with realistic computation times.
- Conduct a more indepth analysis of the likelihood function (e.g. analysis of standard deviation) and develop design rules.

Appendix A

Simulation Example

This appendix contains simulated images and listing of simulation input files from the simulation example described in Chapter 3.

Input Files

antenna_1.txt

```
=====
y position: 0
z_position: 9000
centre frequency: 5300000000
bandwidth: 20000000
```

antenna_2.txt

```
=====
y position: 0
z_position: 9002.5
centre frequency: 5300000000
bandwidth: 20000000
```

antenna_3.txt

```
=====
y position: 0
z_position: 9003
centre frequency: 5300000000
bandwidth: 20000000
```

antenna_setup.txt

```
=====
      1           1
      1           2
      1           3
transmit antenna - receive antenna
```

setup_insim.m

```
=====
% Directory path of antenna setup files
antenna_file_tag = 'c:\MAInSAR\input\airsar\antenna';
% Location of antenna tx/rx arrangement file
antenna_tx_rx = 'c:\MAInSAR\input\airsar\antenna_setup.txt';
% Directory path for simulator output files
output_directory = 'c:\MAInSAR\output\airsar\';
% Location of DEM file
dem_file = 'c:\MAInSAR\input\ers\dem_mound.dat';
% Number of antennas
N = 3;
% Master antenna number
master_antenna_no = 1;
% Number of rows in DEM
dem_rows = 512;
% Number of columns in DEM
dem_columns = 256;
% Range spacing of DEM samples in metres
dem_range_spacing = 50.0;
% Azimuth spacing of DEM samples in metres
dem_azimuth_spacing = 12.5;
% Desired slant range pixel spacing in SAR image in metres
slant_range_spacing = 12.5;
% Desired azimuth pixel spacing in SAR image in metres
azimuth_spacing = 12.5;
% Number of rows to be simulated
row_subset = [1,512];
% Speed of light in m/s
WAVE_SPEED = 3e8
% Radar pulse frequency in Hz
radar_frequency = 5300000000.00;
% Pulse Bandwidth in Hz
radar_bandwidth = 20000000.00;
% Near slant range to the swath
near_slant_range = 10392.3;
% Near ground range to the swath
near_ground_range = 5196.2;
% Number of slant range bins to be simulated
no_slant_range_bins = 512;
% SNR for mid swath as ratio (assuming flat ground)
SNR_SR=64;
% Flags for simulation output products
flat_earth_flag = 1;
coherence_map_flag = 1;
layover_map_flag = 1;
shadow_map_flag = 1;
height_map_flag = 1;
angle_arrival_map_flag = 1;
```

Simulated Images

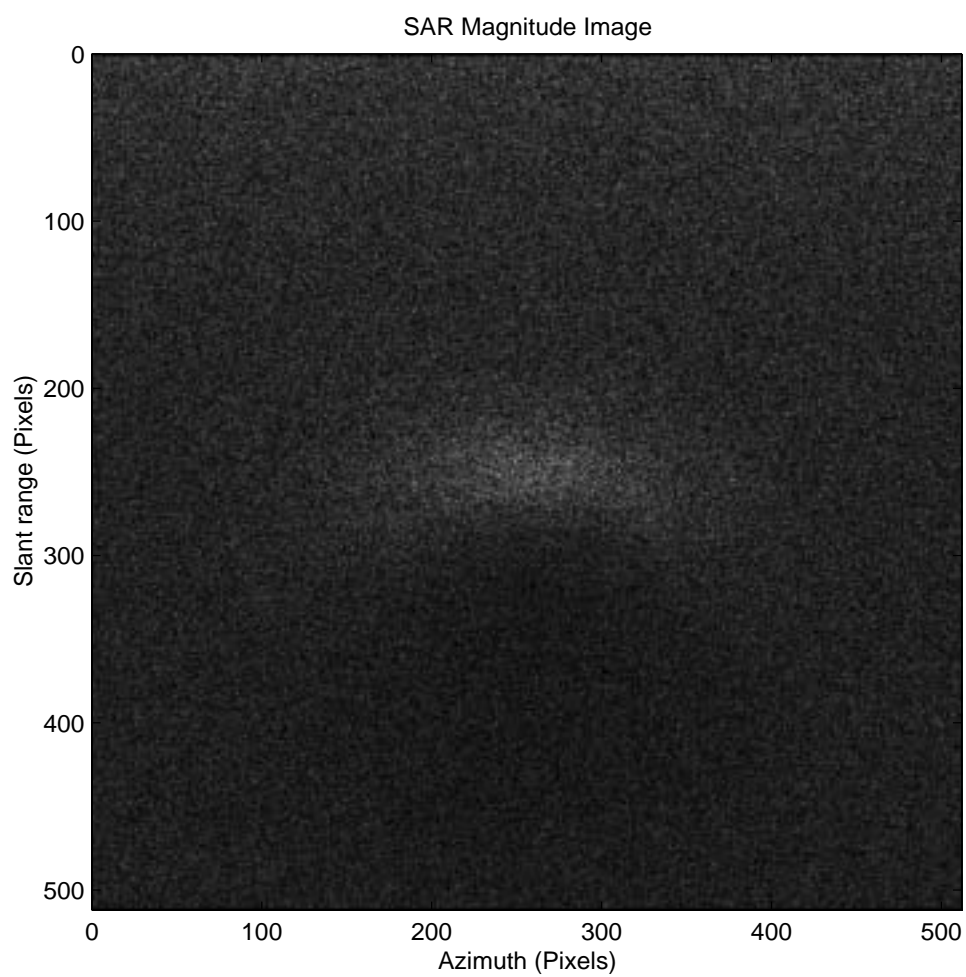


Figure A.1: SAR magnitude image acquired from antenna 1.

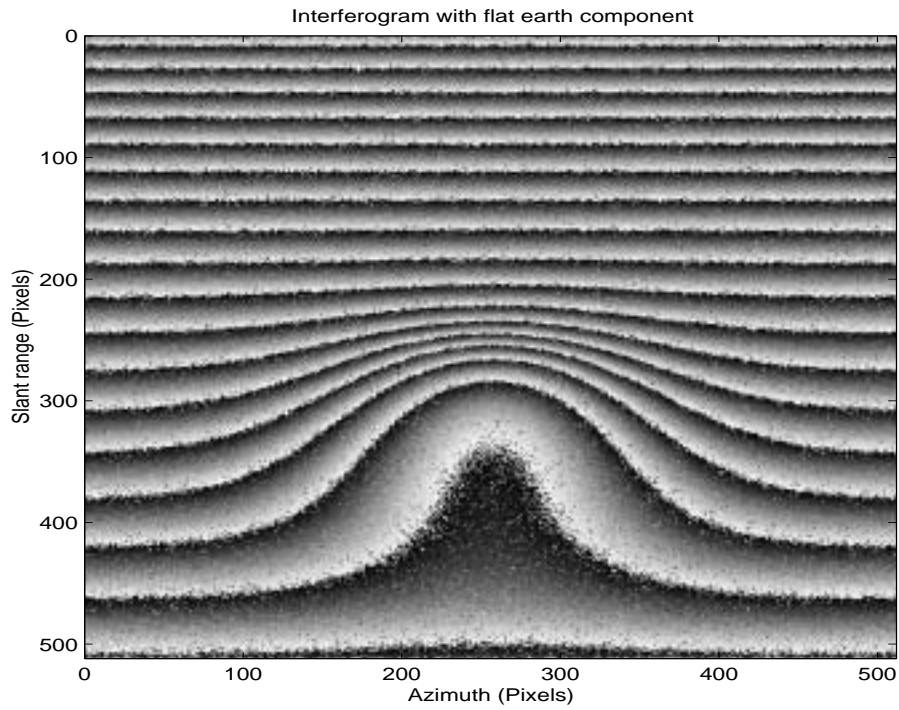


Figure A.2: Interferogram formed with antenna 1 and antenna 3 SAR images.

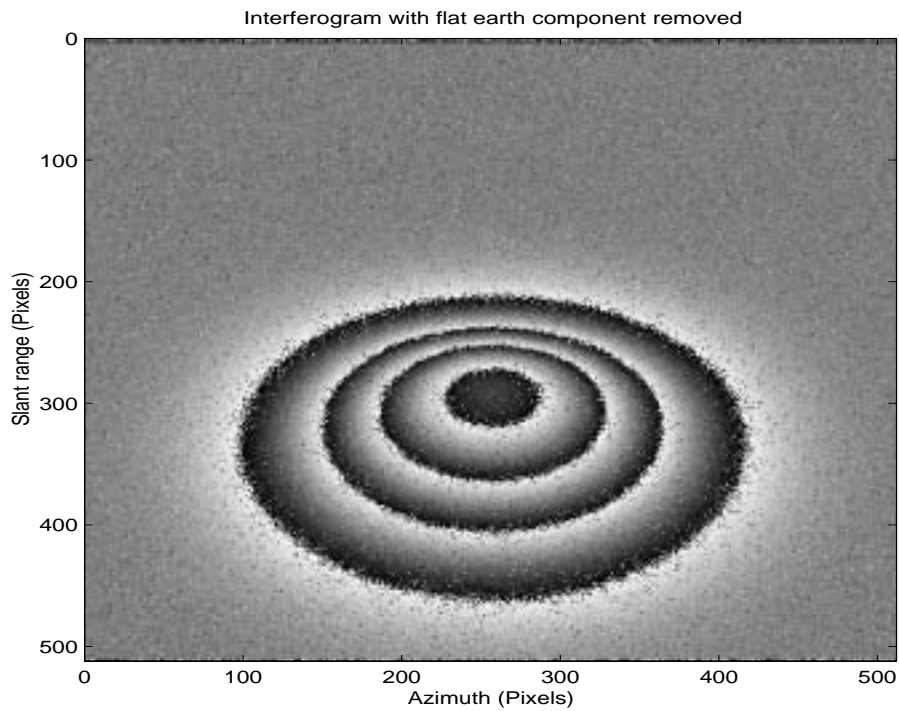


Figure A.3: Interferogram (flat earth component removed) formed with antenna 1 and antenna 3 SAR images.

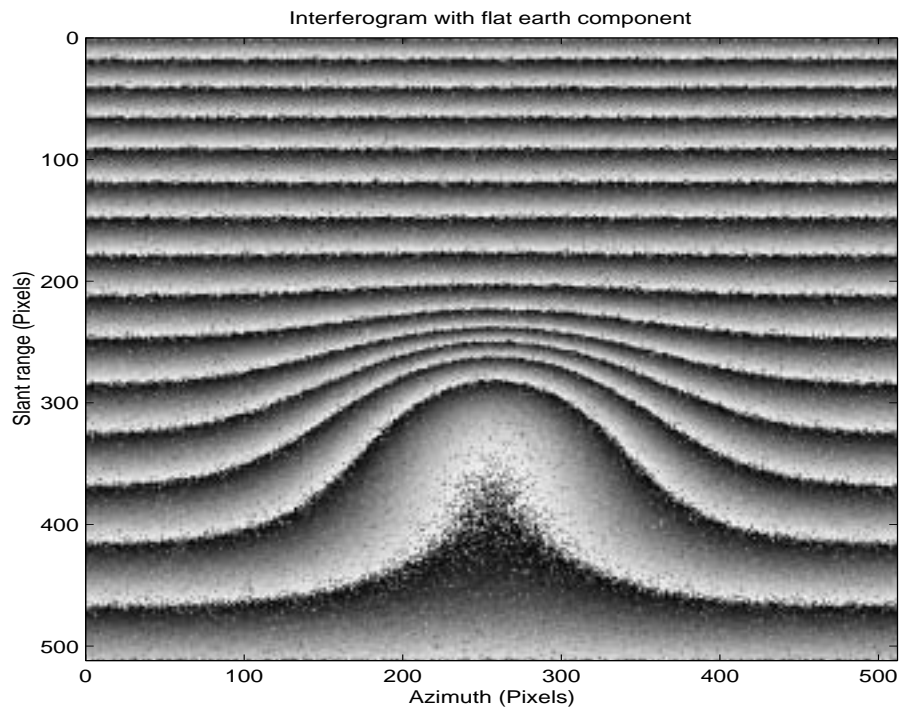


Figure A.4: Interferogram formed with antenna 1 and antenna 2 SAR images.

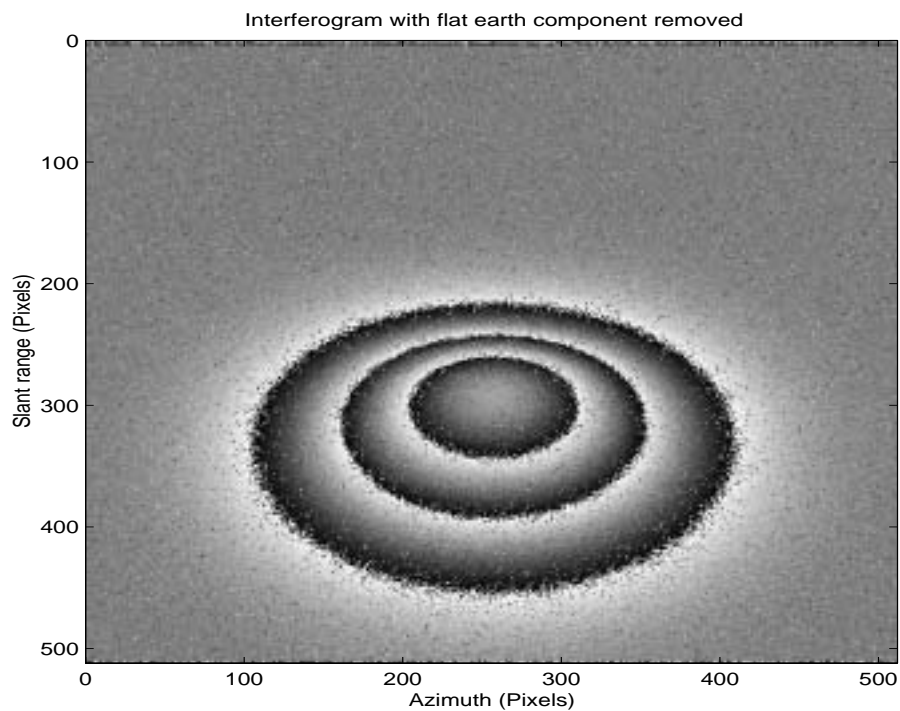


Figure A.5: Interferogram (flat earth component removed) formed with antenna 1 and antenna 2 SAR images.

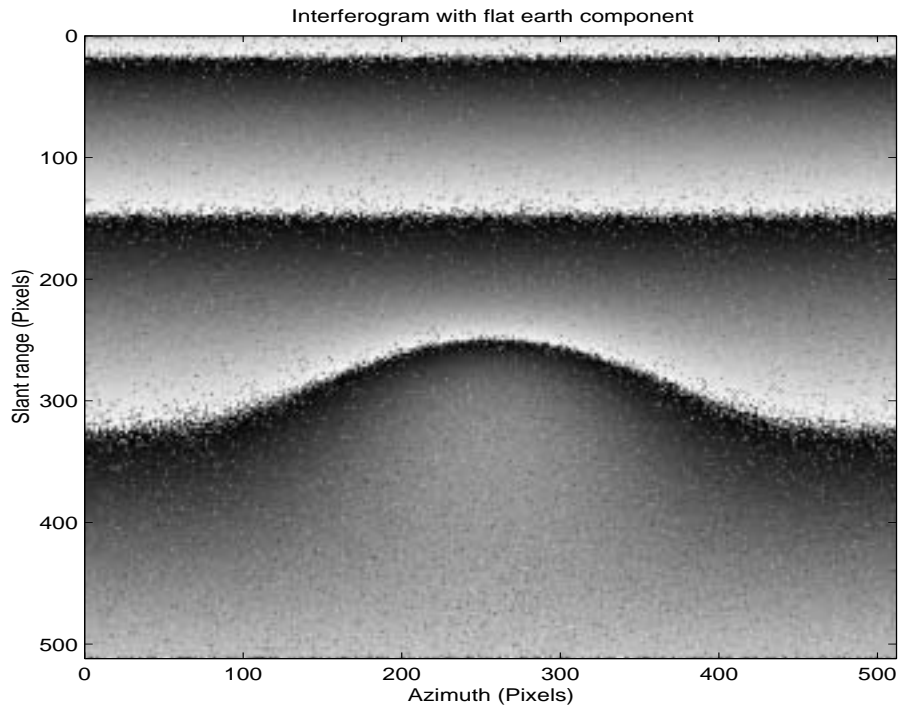


Figure A.6: Interferogram formed with antenna 2 and antenna 3 SAR images.

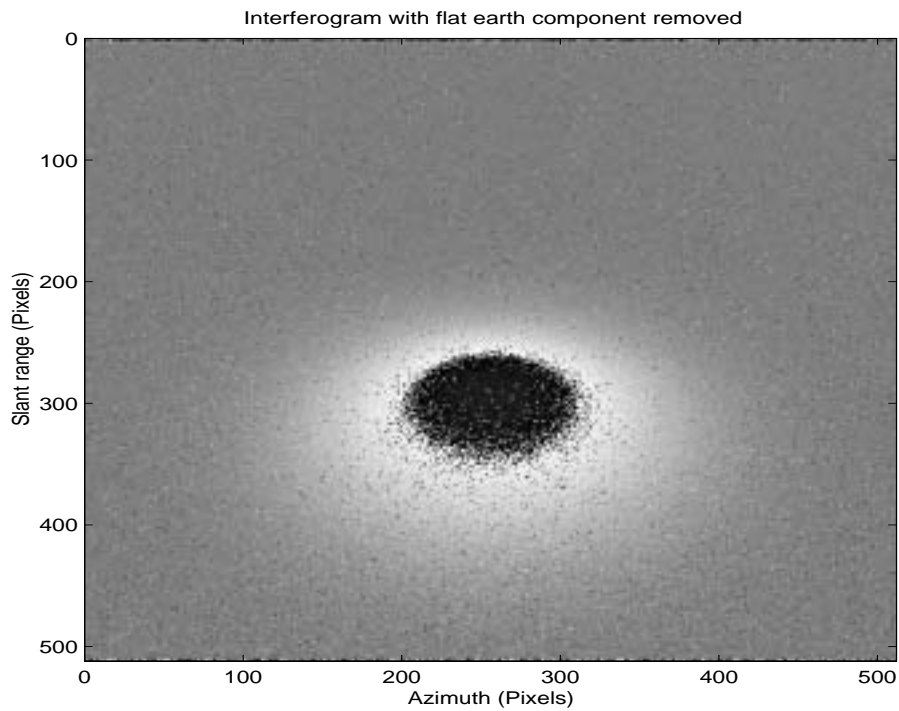


Figure A.7: Interferogram (flat earth component removed) formed with antenna 2 and antenna 3 SAR images.

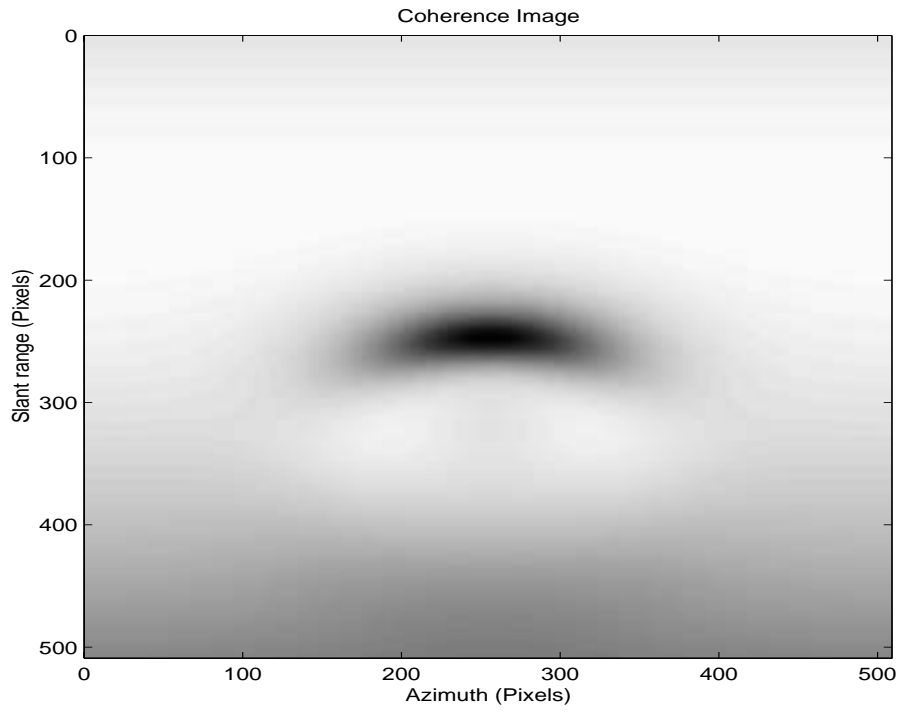


Figure A.8: Coherence map for antenna 1 and antenna 3 SAR images.

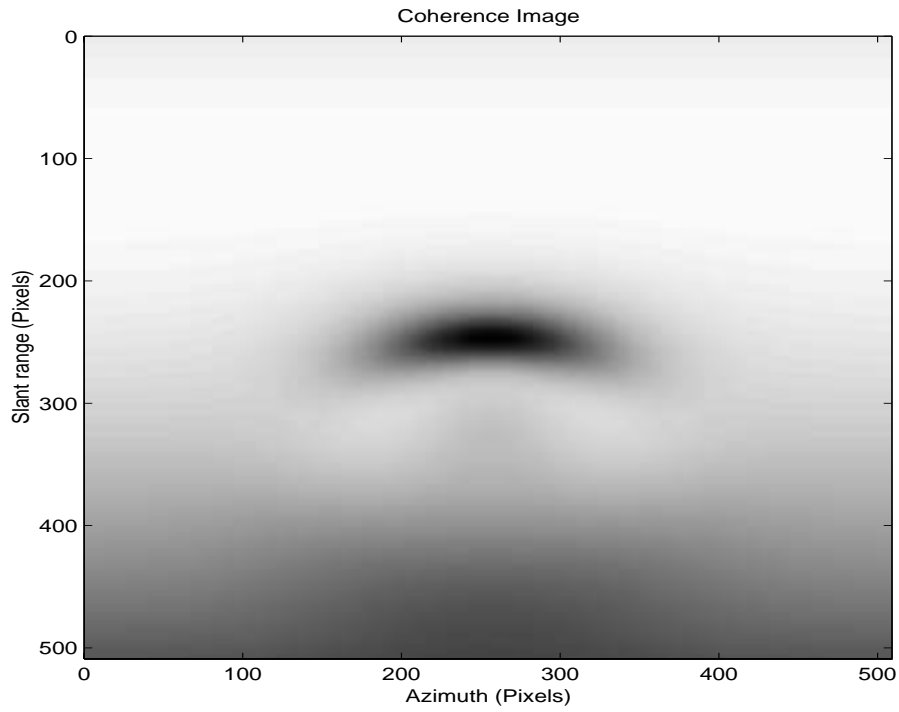


Figure A.9: Coherence map for antenna 1 and antenna 2 SAR images.

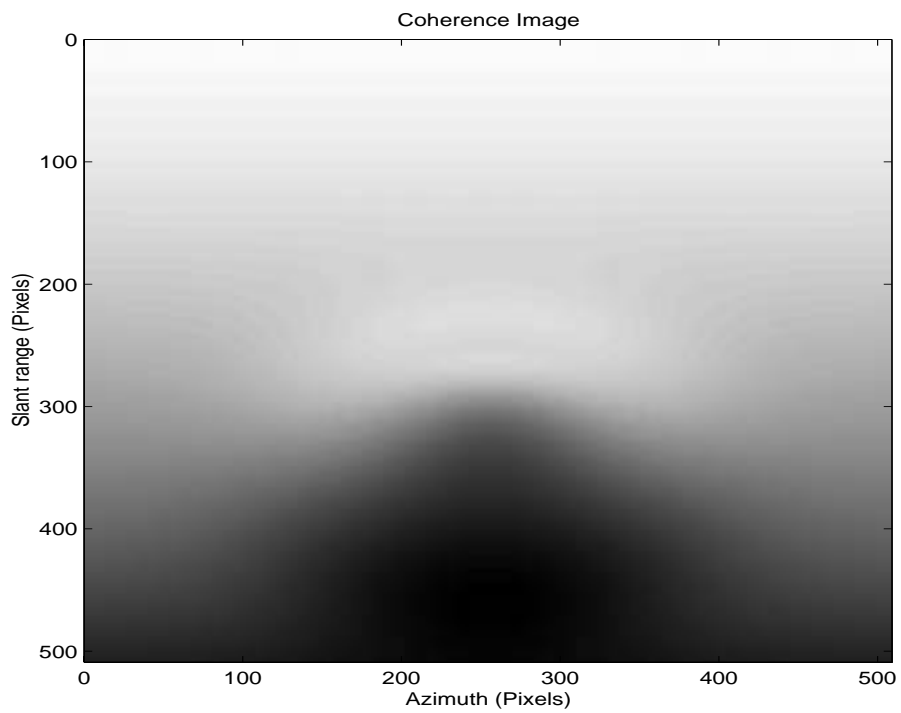


Figure A.10: Coherence map for antenna 2 and antenna 3 SAR images.

Appendix B

Topographic Reconstruction Demonstration

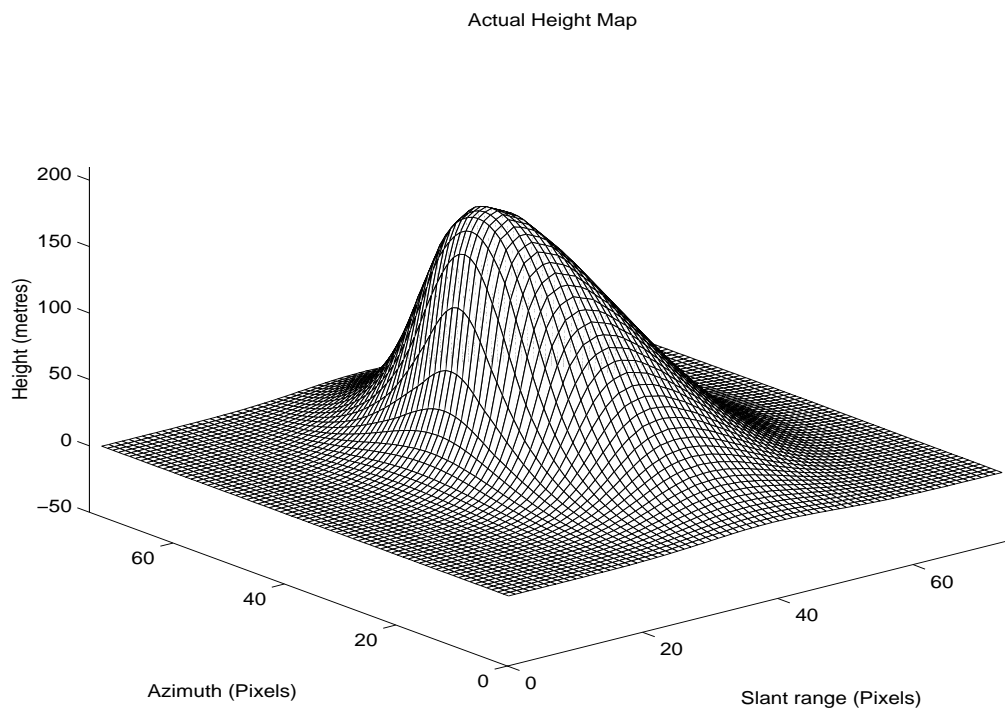


Figure B.1: Actual DEM, slant range projection.

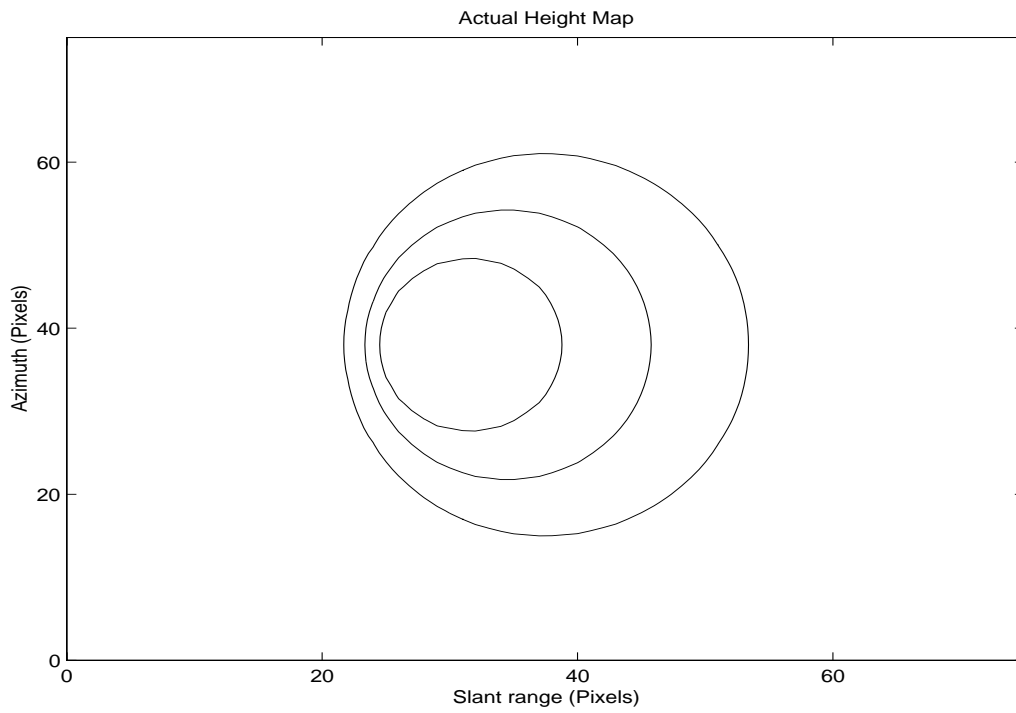


Figure B.2: Actual DEM Contour map, slant range projection.

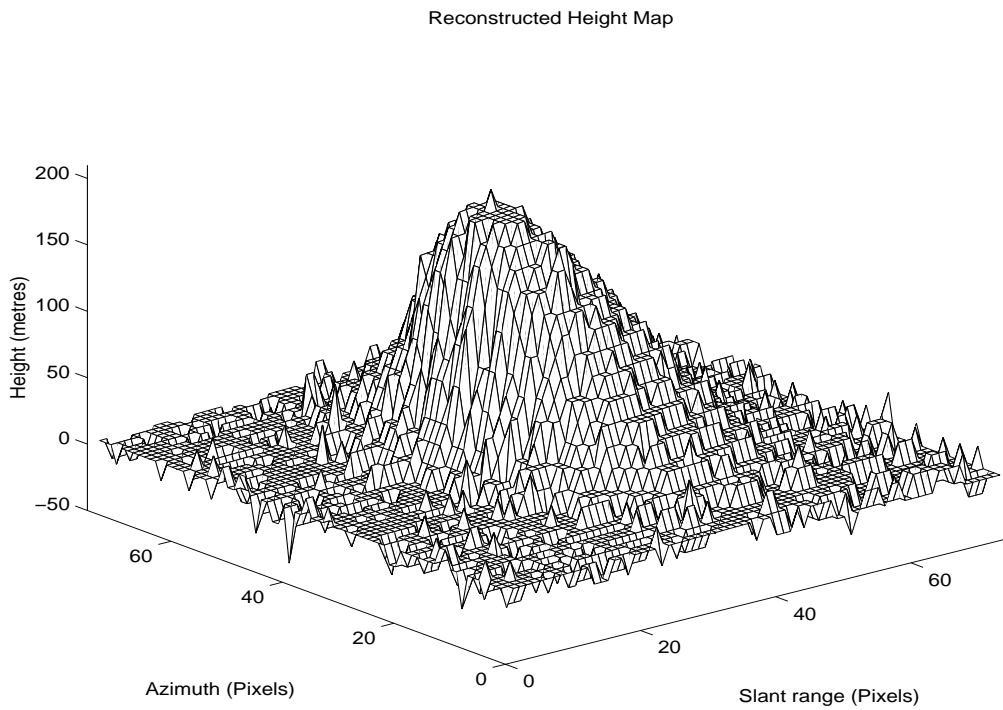


Figure B.3: Reconstructed DEM, slant range projection.

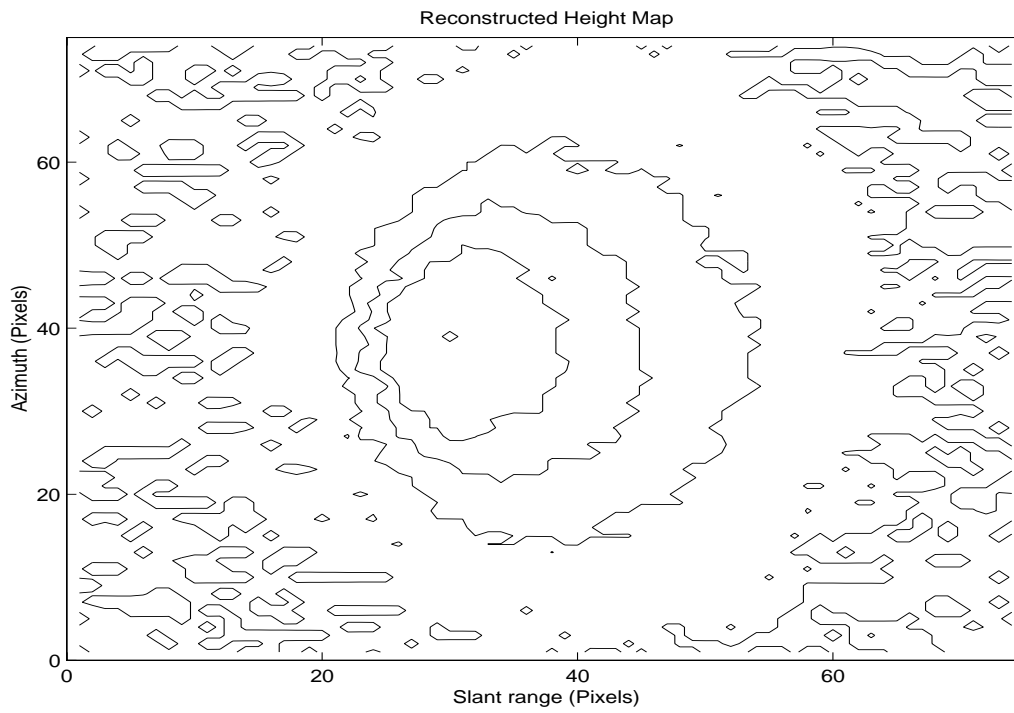


Figure B.4: Reconstructed DEM Contour map, slant range projection.

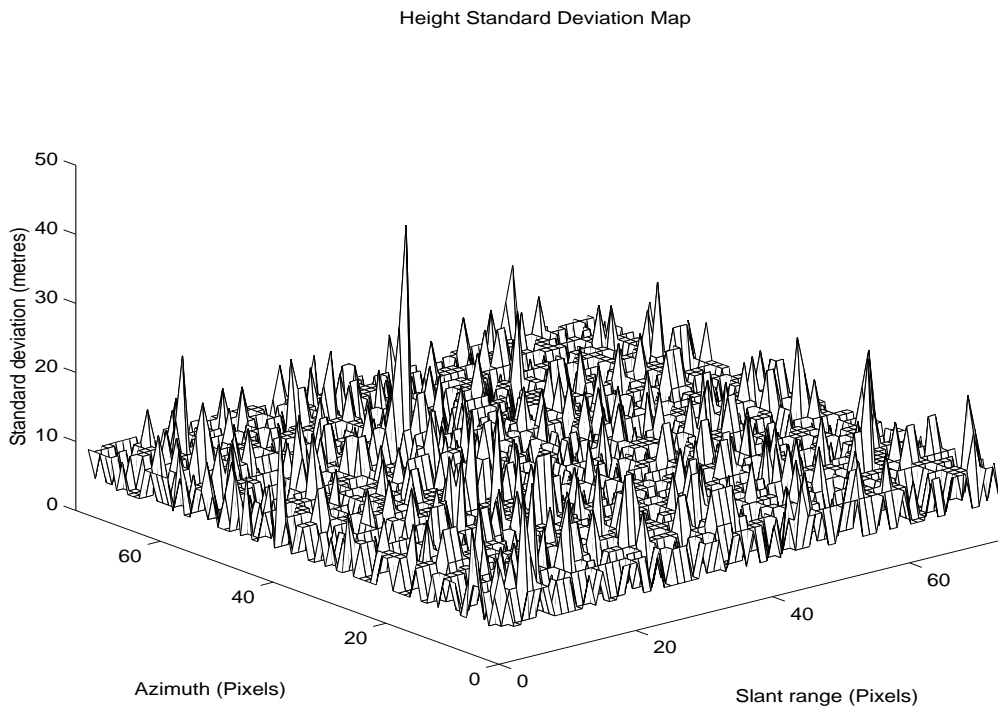


Figure B.5: Height standard deviation map, slant range projection.

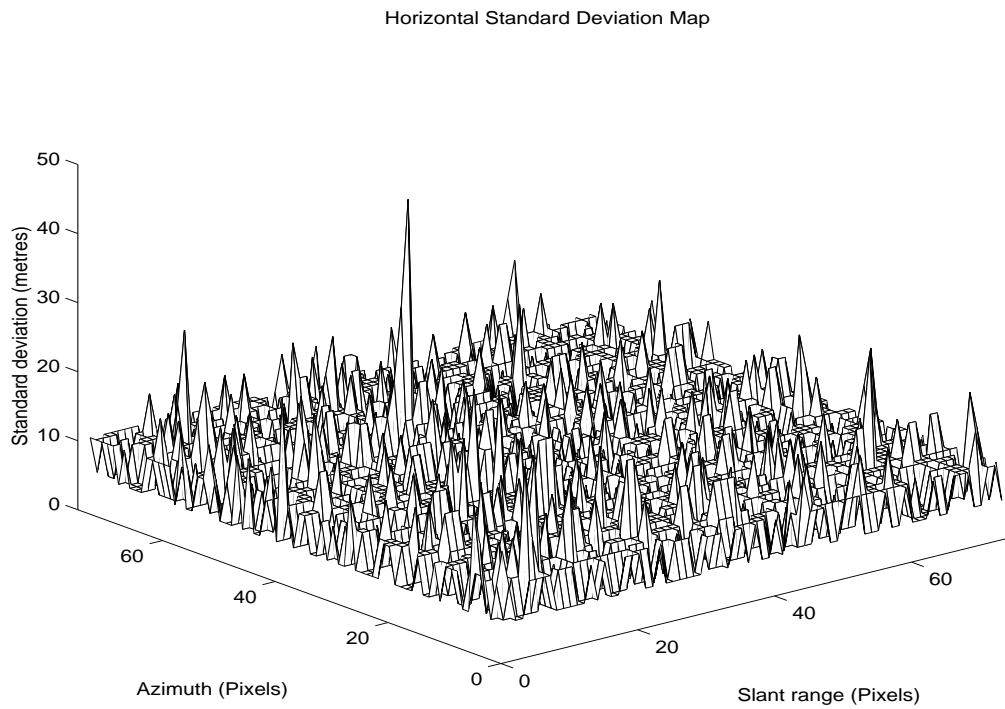


Figure B.6: Horizontal standard deviation map, slant range projection.

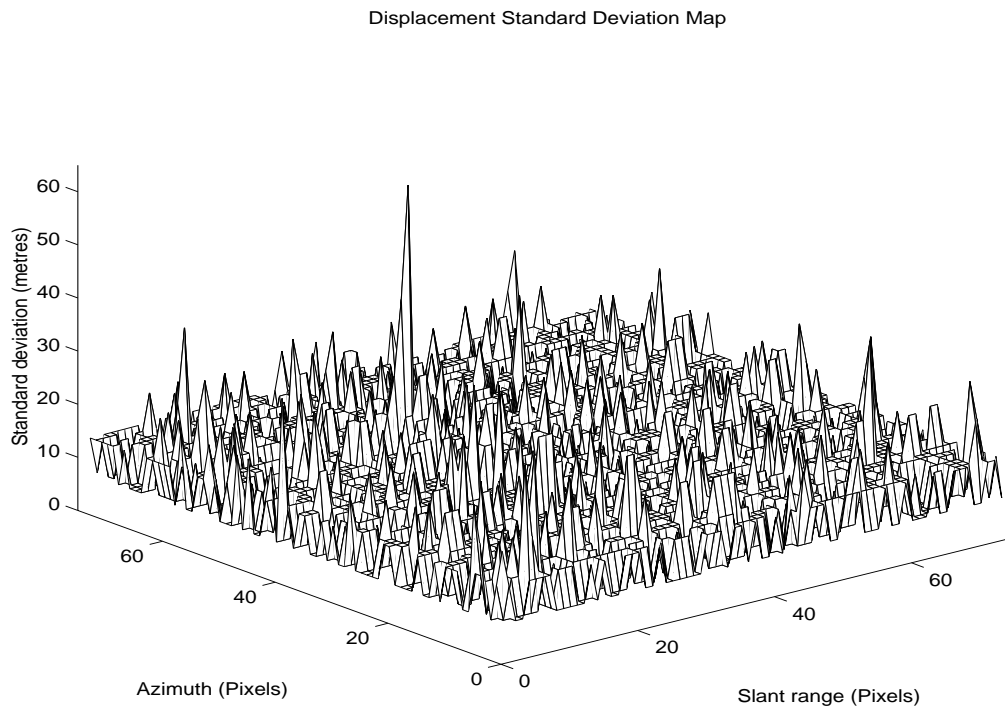


Figure B.7: Displacement standard deviation map, slant range projection.

Bibliography

- Bamler R. and Hartl P. (1998). Synthetic aperture radar interferometry. *Inverse Problems*, **14**, R1:R54.
- Carande R.E. (1992). Dual baseline and frequency along track interferometry. In *Proceedings IGARRS'92*. 1585-1588.
- Constantini M. (1996). A phase unwrapping method based on network programming. *FRINGE'96 ESA Workshop on Applications of ERS SAR Interferometry*.
<http://www.geo.unizh.ch/rsl/fringe96>
- Corsini G., Diani M., Lombardini F. and Pinelli G. (1999). Simulated analysis and optimization of a three-antenna airborne InSAR system for topographic mapping. *IEEE Transactions on Geoscience and Remote Sensing*, **37**(5), 2518-2529.
- Corsini G., Diani M., Lombardini F. and Pinelli G. (1997). Reduction of phase-unwrapping drawbacks by the three-antenna interferometric SAR . In *Proceedings IGARSS'97*, 1536-1538.
- Derauw D. and Moxhet J. (1996). Multiple images SAR interferometry. *FRINGE'96 ESA Workshop on Applications of ERS SAR Interferometry*.
<http://www.geo.unizh.ch/rsl/fringe96>
- Ferretti A., Guarnieri A. M., Rocca F., and Prati C. (1996). Multibaseline interferometric techniques and applications. *FRINGE'96 ESA Workshop on Applications of ERS SAR Interferometry*. <http://www.geo.unizh.ch/rsl/fringe96>
- Ferretti A., Prati C., Rocca F., and Guarnieri A. M. (1997). Multibaseline SAR interferometry for automatic DEM reconstruction. In *Proceedings 3rd ERS Symposium*.
- Gabriel A.K. and Goldstein R.M. (1988). Crossed orbit interferometry: theory and experimental results from SIR-B. *International Journal of Remote Sensing*, **9**(8), 857-872.

- Gabriel A.K., Goldstein R.M., and Zebker H.A. (1989). Mapping small elevation changes over large areas: differential radar interferometry. *Journal of Geophysical Research*, 94, 9183-9191.
- Gelman A., Carlin J. B., Stern H. and Rubin D.B. (1995). Bayesian Data Analysis. *Chapman and Hall*.
- Ghiglia D.C. and Wahl D.E. (1994). Interferometric synthetic aperture radar terrain elevation mapping from multiple observations. In *Proceedings 6th IEEE Digital Signal Processing Workshop*. 33-36.
- Goldstein R.M. and Zebker H.A. (1987). Interferometric radar measurements of ocean surface current. *Nature*, **328**, 707-709.
- Goldstein R.M., Zebker H.A., and Werner C.L. (1988). Satellite radar interferometry: two-dimensional phase unwrapping. *Radio Science.*, **23**(4), 713-720.
- Goldstein R. (1995). Atmospheric limitations to repeat-track radar interferometry. *Geophysical Research Letters*, **22**(18), 2517-2520.
- Graham L.C. (1974). Synthetic interferometer radar for topographic mapping. In *Proceedings IEEE*, **62**, 763-768.
- Hagberg J.O. and Ulander L. M. (1993). On the optimization of interferometric SAR for topographic mapping. *IEEE Transactions on Geoscience and Remote Sensing*, **31**(1), 303-306.
- Hanssen R. and Feijt A. (1996). A first quantitative evaluation of atmospheric effects on SAR interferometry. *FRINGE'96 ESA Workshop on Applications of ERS SAR Interferometry* <http://www.geo.unizh.ch/rsl/fringe96>
- Hartl P. and Wu X. (1993). SAR Interferometry: Experiences with various phase unwrapping methods. In *Proceedings Second ERS-1 Symposium*, 727-732, ESA Publications Division.
- Homer J., Longstaff I.D., and Callaghan G. (1996). High resolution 3-D SAR via multi-baseline interferometry. In *Proceedings IGARSS'96*. 796-798.
- Homer J., Longstaff I.D., and She Z. (1997). Improved digital elevation models via multi-baseline interferometric SAR. In *Proceedings IGARSS'97*. 1579-1580.
- Jakowatz C.V. , Wahl D.E. and Thompson P.A. (1996). Ambiguity resolution in SAR interferometry by use of three phase centers. In *Proceedings SPIE Aerospace Conference*. **2757**, 82-91.

- Lee P. M. (1997). Bayesian Statistics: An Introduction. 2nd edition, *Arnold*.
- Lombardini F. (1996). Absolute phase retrieval in a three-element synthetic aperture radar interferometer. In *Proceedings CIE'96 International Conference of Radar*, 309-312.
- Lombardini F. (1998). Optimum absolute phase retrieval in a three-element SAR interferometer. *Electronic Letters*. **34**, 1522-1524.
- Lombardo P. and Lombardini F. (1997). Multi-baseline SAR interferometry for terrain slope adaptivity. In *Proceedings IEEE National Radar Conference'97*, 196-201.
- Massonnet D. and Rabaute T. (1993). Radar interferometry: limits and potential. *IEEE Transactions on Geoscience and Remote Sensing*, **31**, 455-464.
- Massonnet D. , Briole P. and Arnaud A. (1995). Deflation of Mount Etna monitored by spaceborne radar interferometry. *Nature*, 375, 567-570.
- Nico G., Palubinskas G., and Datcu M. (2000). Bayesian approaches to phase unwrapping: theoretical study. *IEEE Transactions on Geoscience and Remote Sensing*, **48**(9), 2545-2556.
- O'Hagan A. (1994), Bayesian Inference. *Volume 2B of Kendall's Advanced Theory of Statistics*, *Arnold*.
- Oliver C. and Quegan S. (1998). Understanding Synthetic Aperture Radar Images. *Artech House Remote Sensing Library*. *Artech House*.
- Prati C. and Rocca F. (1992). Range resolution enhancement with multiple SAR surveys combination. In IEEE 1991, *IEEE Proceedings*, 1576-1578.
- Prati C. and Rocca F. (1993). Use of spectral shift in SAR interferometry. *Proceedings Second ERS-1 Symposium (Jan'94 ed.)*, Volume ESA, 691-696, ESA Publications.
- Rodriguez E. and Martin J.M. (1992). Theory and design of interferometric synthetic aperture radars. In *IEE Proceedings*, **139**, 147-159.
- Rogers A.E.E. and Ingalls R.P. (1969). Venus: Mapping the surface reflectivity by radar interferometry. *Science*, **165**, 797-799.
- Skolnik M. (1981). Introduction to Radar Systems. 2nd edition, *Artech House*.
- Tarayre H. and Massonnet D. (1994). Effects of a refractive atmosphere on interferometric processing. In *Proceedings IGARRS'94*.

- Touzi R., Lopes A., Bruniquel J. and Vachon P.W. (1999). Coherence estimation for SAR imagery. *IEEE Transactions on Geoscience and Remote Sensing*, **37**(1), 135-148.
- Ulaby T.F., Moore R.K. and Fung A.K. (1982). Microwave Remote Sensing: Active and Passive. Volume II: Radar remote sensing and surface scattering and emission theory. *Addison-Wesley Publishing House*.
- Wilkinson A.J. (1997). Techniques for 3-D surface reconstruction using synthetic aperture radar interferometry. PhD thesis, University of London.
- Wilkinson A.J. and Datcu M. (1997). Interferometric SAR topographic mapping, a Bayesian model-based approach. In *Proceedings COMSIG'97*, Cape Town, South Africa.
- Wilkinson A.J. (1998). Synthetic aperture radar interferometry: A model for joint statistics in layover areas. In *Proceedings COMSIG'98*, Cape Town, South Africa, 333-338.
- Wilkinson A.J. (1999). Synthetic aperture radar interferometry: A statistical model for layover areas. In *Proceedings IGARSS'99*, Hamburg, Germany.
- Wilkinson A.J. (2000). *personal communication*.
- Wray L.S. (2000). Synthetic Aperture Radar image simulator for interferometry. MSc. thesis, University of Cape Town.
- Xu W., Chang C., Kwok L.K., Lim H., Heng W.C.A. (1994). Phase unwrapping of SAR interferogram with multi-frequency or multi-baseline. In *Proceedings IGARSS'94*. 730-732.
- Zebker H.A. and Goldstein R.M. (1986). Topographic mapping from interferometric synthetic aperture radar observations. *Journal of Geophysical Research*, **91**(B5), 4993-4999.
- Zebker H.A., Madsen S.N., Martin J., Wheeler K.B., Miller T., Lou Y., Alberti G., Vetroia S. and Cucci A. (1992). The TOPSAR interferometric radar topographic mapping instrument. *IEEE Transactions on Geoscience and Remote Sensing*, **30**(5), 933-940.
- Zebker H.A. and Villasenor J. (1992). Decorrelation in interferometric radar echoes. *IEEE Transactions on Geoscience and Remote Sensing*, **30**, 950-959.